BOMBYX MORI SILK:
FROM MECHANICAL PROPERTIES TO FUNCTIONALITIES

KOH LENG DUEI

NATIONAL UNIVERSITY OF SINGAPORE

2015

BOMBYX MORI SILK:
FROM MECHANICAL PROPERTIES TO FUNCTIONALITIES

KOH LENG DUEI

(B.Eng.(Hons.), NUS)

A THESIS SUBMITTED

FOR THE DEGREE OF DOCTOR OF PHILOSOPHY

DEPARTMENT OF BIOMEDICAL ENGINEERING

NATIONAL UNIVERSITY OF SINGAPORE

2015

DECLARATION

I hereby declare that the thesis is my original
work and it has been written by me in its entirety.
I have duly acknowledged all the sources of information
which have been used in the thesis.

This thesis has also not been submitted for
any degree in any university previously.

_____

Koh Leng Duei

31 July 2015

ACKNOWLEDGEMENTS

I would like to express my deepest gratitude to my supervisor, Professor Dr. Han Ming-Yong, for his guidance, support, understanding, patience and encouragement during my graduate studies. Prof. Han's mentorship is paramount in providing a well-rounded experience consistent with my long-term career goals. His vast knowledge, inspiring personality, creative and innovative way of thinking help greatly in the design, implementation and accomplishment of my research work. I am also deeply grateful to Professor Li Jun for rendering his kind assistance and support during my studies in NUS. I am deeply grateful to Dr. Cheng Yuan for her kind encouragement as well as constant guidance and support in the research work throughout my studies. Besides, I am deeply grateful to Professor Zhang Yong-Wei for giving me a lot of support and help in the course of my studies. I would also like to express my appreciation and gratitude to Dr. Tansil Natalia Chendrawati for her guidance in getting my graduate studies started on the right foot by sharing with me important lab skills and knowledge for working with silk materials and sericulture.

I am extremely grateful to Ice Tee Si-Yin, Chen Xuelong, Teng Choon Peng, Dr. Khin Yin Win, Dr. Yu Haidong, and Michelle Low, who helped me a lot throughout my research, as well as Dr. Ye Enyi, Dr. Jiang Shan, Dr. Loh Xian Jun, Dr. Michelle Dela Cruz Regulacio, Dr. Liu Shuhua, Dr. Zhang Shuangyuan, and Dr. Guan Guijian for their words of encouragement and their kind sharing of knowledge and experimental skills. I would also like to take this opportunity to thank all the other colleagues and friends in the Institute of Materials Research and Engineering for their support and encouragement. I am indebted to Chee Wee, my aunt Natalie Nam, and my family members for their deepest love and support at every step of this journey. I would also like to thank all my friends for their encouragement during this journey.

Last but not least, I gratefully acknowledge the National University of Singapore for offering the NUS Research Scholarship to support my studies.

LIST OF PUBLICATIONS

This thesis is based upon the work contained in the following papers:

1. **L. D. Koh**, Y. Cheng, C. P. Teng, Y. W. Khin, X. J. Loh, S. Y. Tee, M. Low, E. Ye, H. D. Yu, Y. W. Zhang, M. Y. Han, Structures, mechanical properties and applications of silk fibroin materials, *Progress in Polymer Science*, **2015**, *46*, 86–110.

2. Y. Cheng, **L. D. Koh**, D. Li, B. Ji, M. Y. Han, Y. W. Zhang, On the strength of β-sheet crystallites of *Bombyx mori* silk fibroin, *Journal of the Royal Society Interface*, **2014**, *11*, 20140305.

3. N. C. Tansil, **L. D. Koh**, M. Y. Han, Functional Silk: Colored and Luminescent, *Advanced Materials*, **2012**, *24*, 1388–1397.

4. N. C. Tansil, Y. Li, **L. D. Koh**, C. P. Teng, Y. W. Khin, X. Y. Liu, M. Y. Han, The use of molecular fluorescent markers to monitor absorption and distribution of xenobiotics in a silkworm model, *Biomaterials*, **2011**, *32*, 9576–9583.

Publications not included in the thesis:

5. Y. Cheng, **L. D. Koh**, D. Li, B. Ji, Y. Zhang, J. J. Yeo, G. Guan, M. Y. Han, Y. W. Zhang, Peptide–Graphene Interactions Enhance the Mechanical Properties of Silk Fibroin, *ACS Applied Materials and Interfaces,* **2015,** *7*(39), 21787–21796.

6. G. Guan, S. Zhang, S. Liu, Y. Cai, M. Low, C. P. Teng, I. Y. Phang, Y. Cheng, **L. D. Koh**, B. Srinivasan, Y. Zheng, Y. W. Zhang, M. Y. Han, Protein Induces Layer-by-Layer Exfoliation of Transition Metal Dichalcogenides, *Journal of the American Chemical Society*, **2015,** *137*(19)*,* 6152–6155.

7. S. Y. Tee, E. Ye, P. H. Pan, C. J. J. Lee, H. K. Hui, S. Y. Zhang, **L. D. Koh**, Z. Dong, M. Y. Han, Fabrication of bimetallic Cu/Au nanotubes and their sensitive, selective, reproducible and reusable electrochemical sensing of glucose, *Nanoscale*, **2015**, *7*, 11190–11198.

Table of Contents

SUMMARY

Bombyx mori silkworms are the main producer of silk worldwide. It has been used as high-end textile fibers and as surgical sutures, and is being further developed for various emerging biomedical applications including drug delivery, tissue engineering, sensing, and imaging. The silk fibroin features a hierarchical architecture consisting of β-sheet crystallites embedded in a less ordered amorphous matrix, which accounts for its unique combination of lustre appearance, soft-to-touch texture, and impressive mechanical properties. Notably, many applications of silk take advantage of its impressive mechanical properties, which by nature surpass many natural and synthetic materials. Interestingly, both the silkworm silk and spider dragline silk share similar hierarchical architecture but possess great disparity in mechanical properties.

Inspired by spider dragline silk with much superior strength and toughness, there is an ever growing interest to enhance the mechanical properties of *Bombyx mori* silk. Here, we design a green and facile feeding method to modulate the structures of silk fibroin at the nanoscale using citric acid (CA), and achieved greatly enhanced mechanical properties. The silk obtained (i.e., CA silk) emerges to be the intrinsically toughest silkworm silk, with mechanical properties that exceed those of the previously reported natural and enhanced silkworm silk, and compare well with those of naturally produced spider silk (including those from spiders *Araneus diadematus*, *Nephila clavipes*, etc.).The underlying interactions of CA with fibroin structures are revealed by both advanced characterizations and simulations. It is found that CA interacts with fibroin, resulted in remarkably shorter crystallites, and thus giving the outstanding strength and toughness of the CA silk. The greatly enhanced mechanical properties are expected to lead to better functionalities and wider applications of the *Bombyx mori* silkworm silk.

Silkworms usually produce white silk with normal feed containing no xenobiotics. Here, through introducing fluorescent xenobiotics into silkworm's diet and monitoring the resulting color and fluorescence in the silkworm's body, we established an understanding on the *in vivo* uptake of xenobiotics in silkworms that leads to direct production of intrinsically colored and/or luminescent silk by the silkworms. The molecular properties-directed absorption, distribution and excretion of xenobiotics were investigated using a series of fluorescent molecules as model compounds in a silkworm model. The efficient uptake of xenobiotics into silk is further studied through quantitative analysis of the intrinsically colored and highly luminescent silk secreted by silkworm. Criteria for effective uptake have been established based on the relationship between the structure-dependent hydrophobicity of various dyes vs. the amount selectively absorbed into the silk. The biological incorporation of dyes into silk, in particular its fibroin is a greener method of producing the functional silk because it eliminates the need of an external dyeing process, along with the resources (water, energy and additional chemicals) associated with conventional dyeing of silk. Beyond the absorption of dyes to produce color and luminescence in the silk, this feeding concept can also be expanded to incorporate other functional molecules (e.g., drugs, antibacterial agents, perfumes and nutrients) into silk with therapeutic or nutritional value.

LIST OF ABBREVIATIONS OR SYMBOLS

α: alpha

β: beta

β-sheet: beta-sheet

λ: wavelength

τ_{mfp}: mean first passage time

A: alanine

A: attempting frequency

AFM: atomic force microscopy

Ag: Silver

ANOVA: analysis of variance

ACL: anterior cruciate ligament

Ca: calcium

CA: citric acid

COOH: carboxyl group

E_a: activation energy

EGFP: Enhanced Green Fluorescent Protein

f: orientation function value

$Fe(NO_3)_3$: ferric nitrate

Fe: iron

FTIR: fourier transform infrared

FWHM: full-width at half-maximum

G: glycine

H_2O: water

H-chain: heavy chain

HFIP: hexafluoroisopropanol

hMSC: human mesenchymal stem cells

HNO_3: nitric acid

k_B: Boltzmann constant

KCl: Potassium chloride

L: crystallite size

L-chain: light chain

LED: light emitting diode
LiBr: lithium bromide
log *P*: partition coefficient
ML: middle layer
MLMC: middle layer-middle chain
N: nitrogen
NaCl: sodium chloride
$NaHCO_3$: sodium hydrogen carbonate
NMR: nuclear magnetic resonance
O: oxygen
P: pressure
PDB: Protein Data Bank
RGD: arginine-glycine-aspartic acid
RMSD: root-mean-square deviation
S: serine
SL: surface layer
SLCC: surface layer-corner chain
SLMC: surface layer-middle chain
T: temperature
T: threonine
TEM: transmission electron microscopy
TGF-β1: Transforming Growth Factor-β1
TiO_2: titanium dioxide
UTF: ultimate tensile force
UV: ultraviolet
V: valine
VMD: visual molecular dynamics
XRD: x-ray diffraction
Y: tyrosine

LIST OF TABLES

LIST OF FIGURES

Chapter 1 Introduction

1.1 General Introduction on *Bombyx Mori* Silkworm Silk

Bombyx mori silk features a unique combination of lustre appearance, soft-to-touch texture, and impressive mechanical properties. *Bombyx mori* silkworms are the main producer of silk worldwide. After being hatched from eggs, the silkworms live through five instars before undergoing metamorphosis into a moth [1]. The silk is produced throughout the instar stages in benign and aqueous conditions in silk glands. At the end of fifth instar, the silk is spun by the silkworms into a continuous thread of silk for cocoon formation. In its raw form, the silk consists of two fibroin fibers held together with a sericin on their surfaces (Figure 1.1) [2–8]. Upon removal of sericin, the fibroin fibers appear shiny and feel soft to the touch [9], and are highly sought after in the textile industry [10]. Moreover, the fibroin fibers are endowed with a combination of attractive strength, toughness, biocompatibility/biodegradability and thermal stability, representing one of the most impressive natural protein fibers that surpass many synthetic and natural fibers [5,11].

Besides being fabricated into braided, knitted and non-woven matrices, the versatile processability of fibroin also enables the regeneration of various morphologies from dissolved fibroin fibers (i.e., fibroin solution), including but are not limited to sponges, hydrogels, films, mats, microparticles and microneedles (Figure 1.2) [11–18]. These matrices/morphologies serve most notably as surgical sutures (e.g., SOFSILK™, PERMA-HAND™), carriers for controlled release and drug delivery, also scaffolds for tissue engineering of corneal [19–21], neural [22] and anterior cruciate ligament (ACL) constructs [14,23]. Recent advances have further developed fibroin as flexible interfacial

components in electronic and photonic devices including edible food sensors, organic light-emitting transistors, metamaterial silk composites, and *in vivo* bio-trackers/detectors [24,25]. Fibroin materials demonstrated good biocompatibility with various cell types by promoting their adhesion, proliferation, growth and functionality. In addition, there is a growing interest to introduce functionalities into silk fibroin while preserving its advantageous intrinsic properties, and also to incorporate silk fibroin in composite systems for improved performance [26–37]. In recent years, the mechanical performance of silk fibroin, which is related to its molecular constituent and packing, has received substantial investigations. One particularly appealing aspect in the research of this natural material today would be the possibility to create stronger and tougher silk. Reliable mechanical properties critically ensure the functionality and durability of the material in most applications. With better mechanical properties, silk fibroin materials can also have a higher safety factor against failure when used in load-bearing applications [5,7].

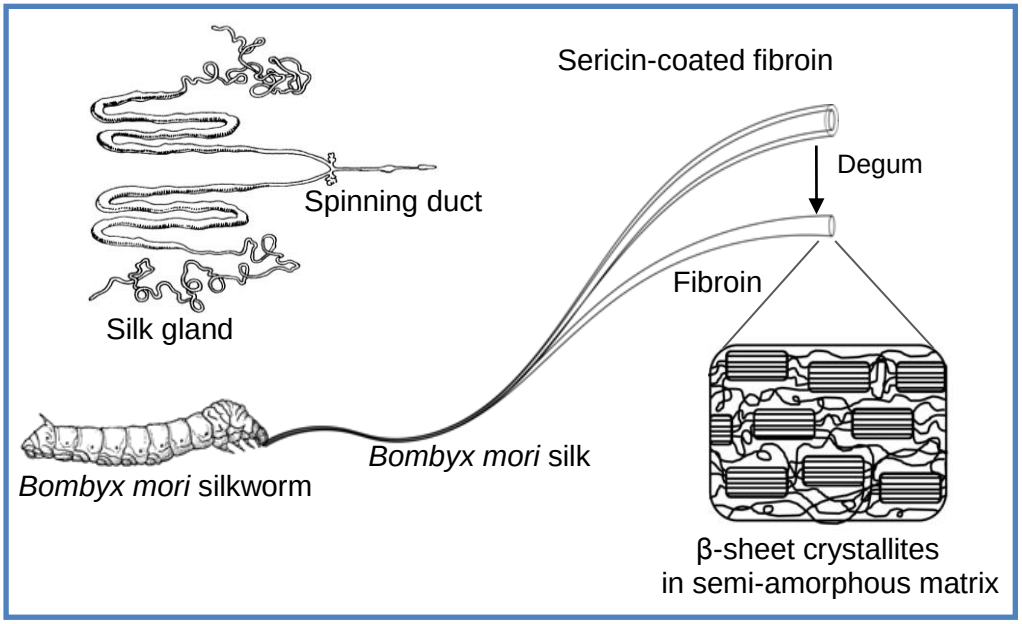

Figure 1.1 An overview of the natural spinning by silkworms from the silk glands to produce fibroin fibers which consist of the ordered and disordered domains [5, 8].

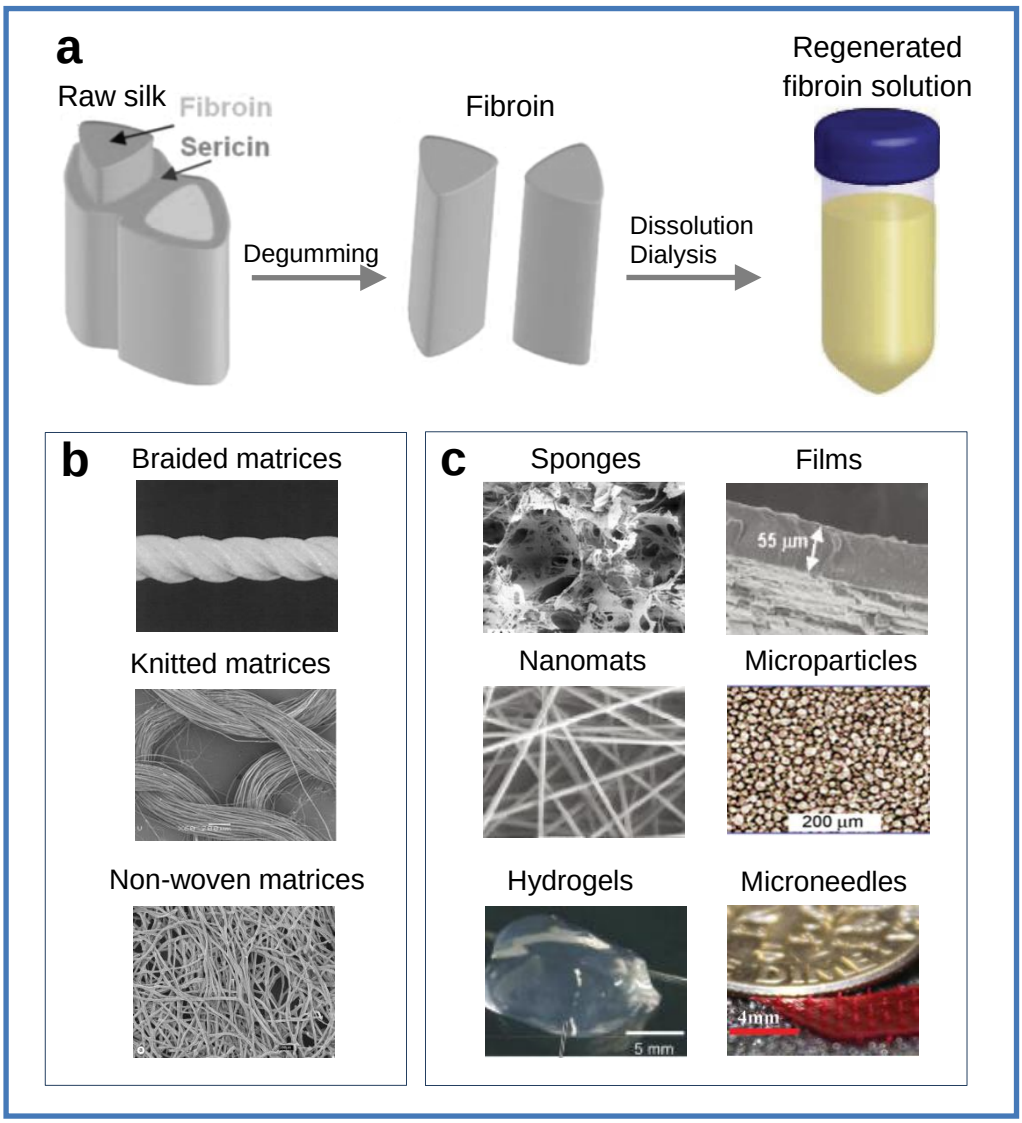

Figure 1.2 *Bombyx mori* silkworm silk in various morphologies. (a) The raw silk consists of two fibroin fibers held together with a layer of sericin on their surfaces. After degumming to remove sericin, the fibroin fibers are dissolved in lithium bromide solution followed by dialyzing against ultrapure water or polyethylene glycol to obtain regenerated fibroin solution, (b) Silk braided, knitted, and non-woven matrices constructed from the fibroin fibers, (c) Silk sponges, hydrogels, films, nanofibrous mats, microparticles, and microneedles constructed from the regenerated fibroin solution [11–18].

1.2 Constituent and Crystal Structure of Silk

1.2.1 Constituent

Silk fibroin consists of a light (L) chain polypeptide and a heavy (H) chain polypeptide linked together via a single disulfide bond at the C-terminus of H-chain, forming a H-L complex [38,39]. The H-L complex also binds glycoprotein P25 in a ratio of 6:1 via hydrophobic interactions to form an elementary micellar unit. Necessarily, the formation of such micellar unit enables the transportation of a large amount of fibroin through silk gland lumen towards the spinnerets before spinning into fibers [11,40].

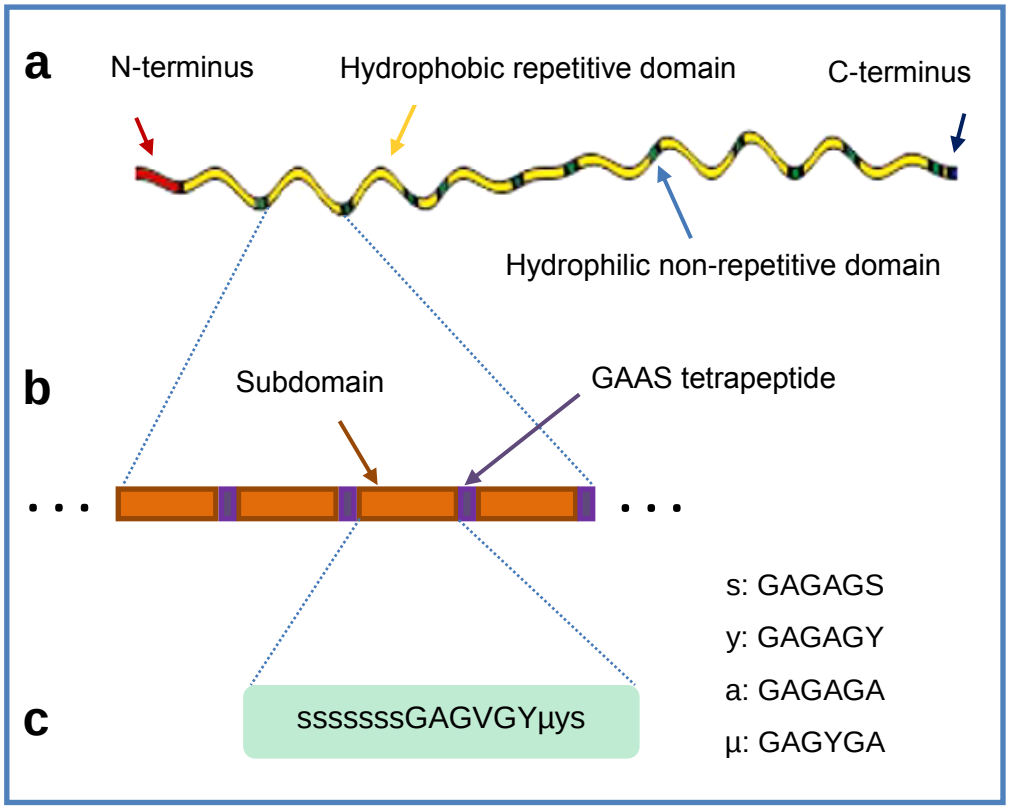

Figure 1.3 (a) Each fibroin heavy chain (H-chain) consists of hydrophobic repetitive domains interspersed between hydrophilic non-repetitive domains [7]. (b) Each repetitive domain consists of subdomains separated by GAAS tetrapeptides. (c) Each subdomain in turn consists of different repeating units of hexapeptides (represented by s, y, a or μ), and terminates with a tetrapeptide GAAS [6,7].

In silk fibroin material, H-chains form discrete β-sheet crystallites serving as the main structural component responsible for the superior mechanical properties, while L-chain plays little mechanical role as its size is much smaller than H-chain and besides, its sequence is also not associated with the formation of the crystalline region in silk fibroin [11,41]. The β-sheet crystallites are in turn embedded in a less-ordered (i.e., semi-amorphous) matrix. In terms of amino acid composition, the H-chain comprises primarily the three simplest amino acids, i.e., glycine (G) (~43–46%), alanine (A) (~25–30%) and serine (S) (~12%), whereas tyrosine (Y) (the larger amino acid with a polar side chain) occurs at ~5%. The next most abundant amino acid in H-chain is valine (V) (~2%), and this is followed by aspartic acid (D), phenylalanine (F), glutamic acid (E), threonine (T), isoleucine (I), leucine (L), proline (P), arginine (R), lysine (K) and histidine (H), which are present in much smaller percentages (i.e., less than 2% each) [6,11,42].

Organizationally, the silk fibroin H-chain is a highly regular biopolymer that consists of 12 hydrophobic domains interspersed with 11 hydrophilic domains (Figure 1.3a). The hydrophobic domains contain amino acids in repetitive sequence (i.e., therefore also referred to as repetitive domains), while the hydrophilic domains contain amino acids in non-repetitive sequence (i.e., also referred to as non-repetitive domains) [5–8]. The repetitive domains (comprising mainly glycine, alanine, serine, and also tyrosine, valine and threonine in lesser proportion) are capable of organizing themselves together into β-sheet crystallites via intramolecular or intermolecular forces including hydrogen bonds, van der Waals forces, and hydrophobic interactions, leading to the formation of highly ordered crystalline regions in silk fibroin. On the other hand, the non-repetitive domains (comprising mainly charged/acidic amino acids, e.g., glutamic acid, aspartic acid, arginine and lysine, which are not found in the repetitive domains [6,39]) form non-crystalline (semi-amorphous) region in silk fibroin [4]. Interestingly, 11 out of 14 proline residues in a H-chain are present at one each for all the 11 hydrophilic domains (also known as linkers),

which serve as β-turns to allow the chain reversal and facilitate folding into a micellar structure during silk processing in vivo [6,39].

1.2.2 Crystal structure

The crystal structure of fibroin in silk fibers was investigated by X-ray diffraction (XRD). The XRD patterns revealed that its molecular chains are orderly aligned along the axis of the silk fibers. Together with chemical analysis, it was proposed that the chains are made up of glycine and alanine with occasional substitution by other amino acids. The chains are held together by strong interactions, which were discovered to be hydrogen bonds between amide linkages of the adjacent chains [42,43].

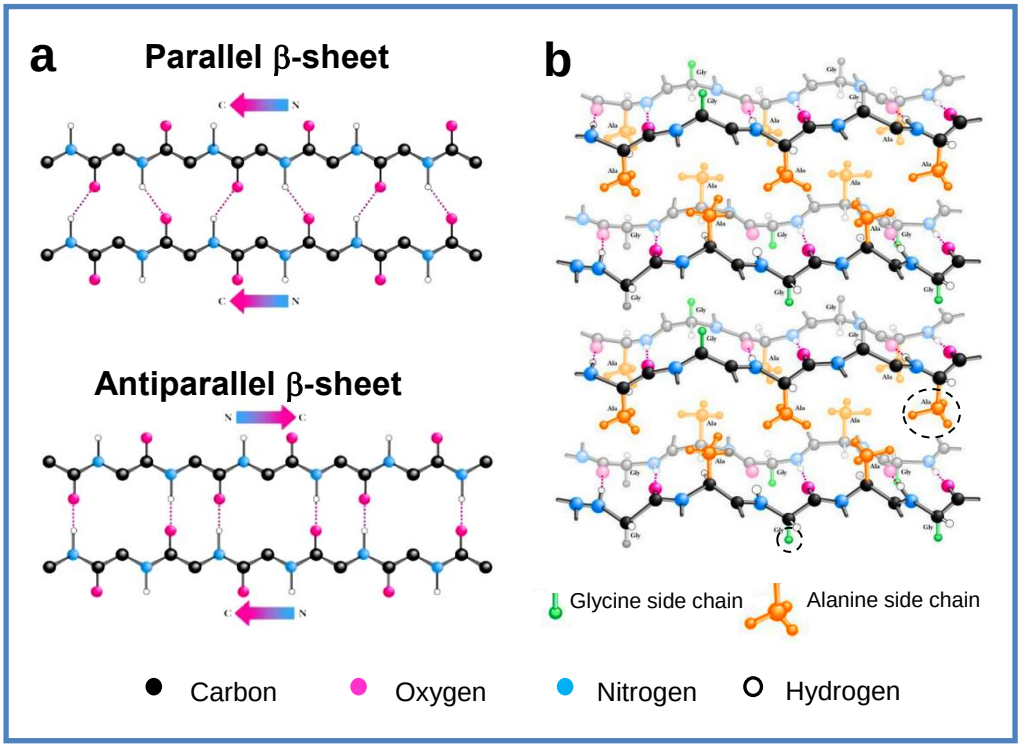

Figure 1.4 (a) Longer bond length (~2.97 Å) and NH---O bond angle deviating by 20° from linearity in parallel fibroin β-sheets, as compared with shorter bond length (~2.76 Å) and NH---O bond angle close to linearity in antiparallel fibroin β-sheets [44]. (b) Widely accepted polar-stacking of antiparallel β-sheets, with the surface of one sheet projecting entirely methyl groups (side chains) of alanine residues and the other surface of the same sheet projecting only hydrogen atoms (side chains) of glycine residues. The intersheet distances alternate at 5.5 Å and 3.7 Å respectively [42,44].

To clarify the packing of the chains, Marsh et al. proposed a pseudo unit based on the two established principles for proteins, i.e., the planarity of the six atoms in each amide linkage, and the tendency towards maximizing the number of hydrogen bonds during molecular arrangement. The repeats of the pseudo unit form β-sheet crystallites, which constitute β-strands with antiparallel arrangement (i.e., adjacent β-strands run in the opposite direction) rather than parallel arrangement (i.e., adjacent β-strands run in the same direction). This is mainly because, there are shorter linear hydrogen bonds (2.76 Å) between antiparallel β-strands as compared to longer non-linear hydrogen bonds (2.97 Å) between parallel β-strands (i.e., a bond angle deviating by 20° from linearity) (Figure 1.4a), which can offer greater stability to the β-sheet crystallites [42–44].

Based on the pseudo unit, the side chains of adjacent β-strands are similar within each face in a β-sheet. In such a polar arrangement, the front face of the β-sheet projects only the glycine side chains (–H) (i.e., glycine face), while the back face of the same sheet projects only the alanine side chains ($–CH_3$) (i.e., alanine face), as illustrated in Figure 1.4b [42,44]. The β-sheets are stacked into a β-sheet crystallite in such a way that similar faces of adjacent β-sheets are facing each other (i.e., front-to-front and back-to-back). Important clues which led to the revelation of such front-to-front and back-to-back stacking of β-sheets were the intersheet distances, which were generated after feeding X-ray equatorial reflections data into Patterson function – a convolution function to solve crystal structures. The calculated intersheet distances between two glycine faces (front-to-front) or two alanine faces (back-to-back) are 3.7 and 5.5 Å, respectively. According to the pseudo unit, the β-sheet crystallite adopts an orthorhombic crystal lattice with unit cell dimensions **a** = 9.20, **b** = 9.40, and **c** = 6.97 Å [42], where **a** is the direction along the stacking of β-sheets, **b** is the direction in a β-sheet perpendicular to the strand axis, and **c** is the direction along the strand axis [42]. Subsequent investigations yielded similar results [41,45,46].

Up till today, the polar-antiparallel arra\ngement in the β-sheet crystallites is still widely accepted.

In addition to XRD, mathematical model, molecular modeling and nuclear magnetic resonance (NMR) spectroscopy have been explored as alternative or complementary techniques to examine the crystal structure of fibroin. For example, while the amino acid residues, glycine and alanine, have been widely accepted as the main constituents responsible for the formation of crystalline region of silk fibroin, the presence of larger residues such as serine and tyrosine in the β-sheet crystallite was still unascertained only until recent confirmation from NMR that the crystalline region could also accommodate serine and tyrosine residues [46–50]. The larger residues resulted in some degree of local disorder in the crystalline structure.

To date, there are still disputes on the (anti)polarity and (anti)parallelity in the β-sheet crystallites of silk fibroin [51]. Four arrangements of strands are possible, and among them three have been suggested as being the crystal structure of fibroin. These include the previously established polar-antiparallel arrangement, and two other arrangements, i.e., polar-parallel and antipolar-antiparallel as discussed below.

Polar-parallel arrangement. A polar β-sheet, i.e., a β-sheet with smaller glycine side chains and larger side chains (e.g., alanine, serine, and tyrosine) respectively at two different faces, can be obtained when there are glycine residues in virtually every alternate amino acid position of the repetitive domains. Zhou et al. determined the amino acid sequence of repetitive domains in H-chain, which have a strict occurrence of glycine residue in every alternate position (i.e., GX as basic repeating units, with X being mainly alanine, serine, tyrosine, valine or threonine), and this necessarily implies the need for the formation of polar β-sheets in silk [6,43]. Molecular modeling based on conformational energy calculations has also simulated the energetically favored structure of silk fibroin [46]. Specifically, using glycylalanyl

chains, also referred to as poly(GA), Fossey et al. derived a polar β-sheet arrangement in the crystalline region (Figure 1.5a), reproducing the structure proposed by Marsh et al. [42] and experimental measurements [41,45,46]. The calculated energies indicated the polar conformation is more stable than the antipolar conformation (Figure 1.5b).

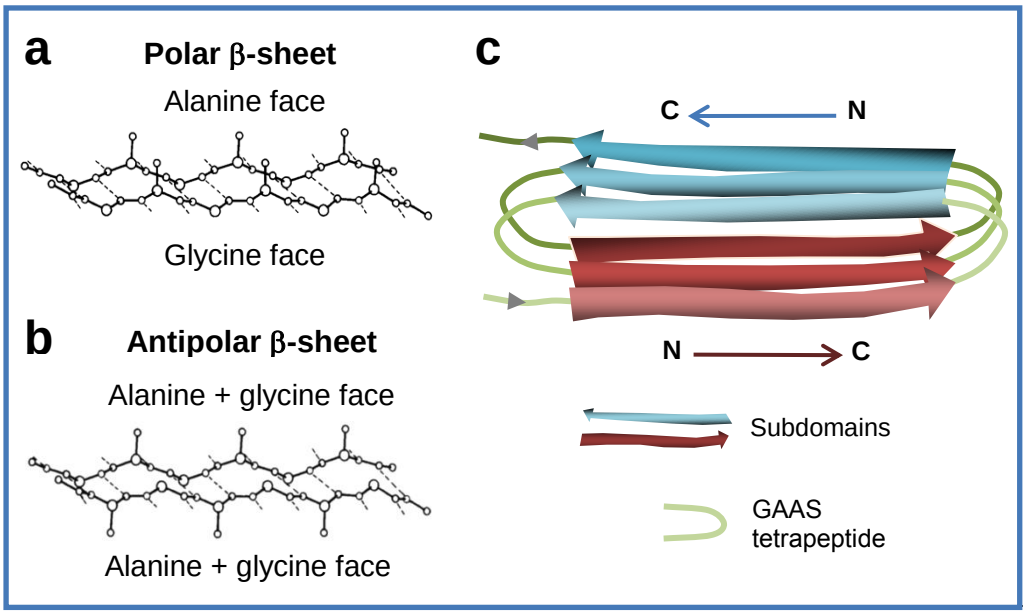

Figure 1.5 Schematic illustration of (a) polar and (b) antipolar poly (GA) β-sheets obtained by conformational energy calculations. The polar β-sheet has an Ala face and a Gly face, while the antipolar β-sheet has two identical faces [46]. (c) Double-layered solenoid structure of fibroin β-sheet crystallite [6], in which consecutive subdomains in H-chain loop through the top and bottom layers alternately, and the adjacent β-strands in each layer run in a parallel manner. Such a structure is proposed to be necessary for satisfactory packing of the amino acid side chains with obvious N- to C- directionality. In between the two layers, the bulkier side chains (i.e., tyrosine, valine and threonine) gather at the C-terminus, and smaller side chains (i.e., glycine, alanine and serine) gather at the N-terminus.

The H-chain sequence derived by Zhou et al. [6] showed that each repetitive domain comprises an average of five to six subdomains (Figure 1.3b), and each subdomain can often form a β-strand. Each subdomain of ~70 residues constitutes different repeating units of hexapeptides (i.e., GAGAGS, GAGAGY, GAGAGA, and GAGYGA, represented by s, y, a and µ, respectively, which are present in the H-chain with the approximate abundance ratio of 32:9:2:3) (Figure 1.3c) [6]. The subdomain shows an obvious N- to C-directionality, in which the more common smaller amino acids of fibroin (i.e., glycine, alanine and serine) gather nearer the N-terminus while the less frequently occurred bulkier amino acids of fibroin (i.e., tyrosine, valine and threonine) gather nearer the C-terminus (e.g., sssssssGAGVGYµysGAAS). With such sequence, it was theoretically suggested that the β-sheet crystallite has a double-layered solenoid structure, in which consecutive subdomains loop alternately through the top and bottom layer, such as that shown in Figure 1.5c. The parallel running of β-strands within each layer of polar β-sheet allows regular packing of the side chains, i.e., the similar side chains of adjacent β-strands can gather at one terminus of β-sheets. GAAS tetrapeptides, which appear regularly between subdomains throughout the repetitive regions (Figure 1.3c), could form β-turns which are required to loop the strand into the double-layered solenoid structure [6]. With the proposed structure, Zhou *et al.* [6] raised the need for parallel arrangement in order for satisfactory packing of the β-sheets to occur.

Antipolar-antiparallel arrangement. Takahashi et al. examined the crystal structure of fibroin using XRD and further analyzed the obtained data with mathematical model [41]. In the analysis which considered the sequence in the crystalline region as $(\text{-GAGAGS-})_n$, all the possible arrangements of strands, including polar-parallel, polar-antiparallel, antipolar-parallel and antipolar-antiparallel arrangements were taken into consideration. The calculated values using constrained least-squares method led to a conclusion disputing the proposed structure

by Marsh et al. [42], i.e., instead of stacking in a polar manner, the β-sheets are stacked in an antipolar manner, whereby larger side chains of adjacent strands point to opposite sides of β-sheets. In this proposed antipolar-antiparallel model, hydrogen bonds between adjacent strands assume four values (i.e., 2.76, 3.05, 3.17, and 3.41 Å). Also, serine side chains are possibly involved in inter-β-sheets hydrogen bonding, based on the calculated distances between hydroxyl groups of serine from adjacent sheets, which are shorter than the sum of their van der Waals radii, although it was acknowledged that such shorter than expected distance between hydroxyl groups of serine from adjacent sheets could also be due to disorder caused by intersheet stacking [41].

1.3. Mechanical Properties of Silk

Naturally produced silk fibroin fiber (*Bombyx mori*) has a high ultimate tensile strength of 300 – 740 MPa [52–54]. It has also large breaking strain and high toughness exceeding those of synthetic fibers such as Kevlar [55,56]. The mechanical properties are listed in Table 1.1 along with those of other natural and synthetic fibers [11,52–55,57–63], and the representative stress-strain curve is shown in Figure 1.6 along with that of spider dragline silk [38]. Increasing evidences suggest that the impressive mechanical properties of silk are closely related to its hierarchical structures [64–67]. Although silkworm and spider silk have different primary structures (e.g., crystalline sequences, poly(GA) in silkworm silk and poly(A) in spider dragline silk [55]), they still possess similar hierarchical structures (i.e., β-sheet crystallites structure, and a semi-amorphous matrix with less ordered structures including helices and turns) [58,64]. Here, we review the structural dependency of the mechanical properties of *Bombyx mori* silkworm silk, incorporating relevant insights drawn from spider dragline silk to benefit the mechanical enhancement efforts of silkworm silk.

Table 1.1 Mechanical data of silkworm silk along with other fibrous materials [11,52–55,57–63].[a]

Materials	Young's Modulus (GPa)	Ultimate Strength (MPa)	Breaking Strain (%)	Toughness (MJ m^{-3})	Ref.
Silkworm silk fibroin (*Bombyx mori*)	10–17	300–740	4–26	70–78	[11,52–55]
β-sheet crystallites (*Bombyx mori*)	16–18	–	–	–	[53,57]
β-sheet crystallites (*Bombyx mori*)[b]	22.6	–	–	–	[58]
Spider silk (*Nephila clavipes*)	10.9	875	16.7	–	[53]
Spider silk (*Nephila edulis*)	–	1300	38	200	[54,59]
Spider silk (*Araneus*)	10	1100	27	160	[55]
Collagen	0.0018–0.046	0.9–7.4	24–68	–	[60,61]
Wool	0.5	200	50	60	[55]
Nylon	1.8–5	430–950	18	80	[55,62]
Kevlar	130	3600	2.7	50	[55]
Polypropylene	4.6	490	23	–	[63]

[a] Unless specifically indicated, the data are extracted from experimental studies. [b] Simulation data.

1.3.1 Structure-dependent mechanical properties

The strength and stiffness of silk are dictated mainly by β-sheet crystallites. In β-sheet crystallites, there are hydrogen bonds, together with intersheet van der Waals and hydrophobic interactions, which contribute significantly to the stability of the structure [58,68]. On the other hand, the extensibility and toughness of silk are governed mainly by the semi-amorphous matrix [17,64,69]. Upon tensile loading, the

material undergoes homogeneous stretching until the onset of yielding, when the material ceases to behave elastically and starts to deform plastically. Respectively, the semi-amorphous matrix and β-sheet crystallites of silk govern its mechanical behavior at small and large deformation during tensile loading. The semi-amorphous components start to unravel beyond yield point, after which the load is transferred to the β-sheet crystallites, which subsequently handle the load up to the point of fracture [64]. Fundamentally, silk fibroin can form intramolecular/intermolecular β-sheet crystallites [67,70], parallel/antiparallel β-sheet crystallites, as well as β-sheet crystallites of different sizes and orientations along fiber axis. Below, these structural aspects of the β-sheet crystallites are discussed pertaining to the mechanical properties of silk.

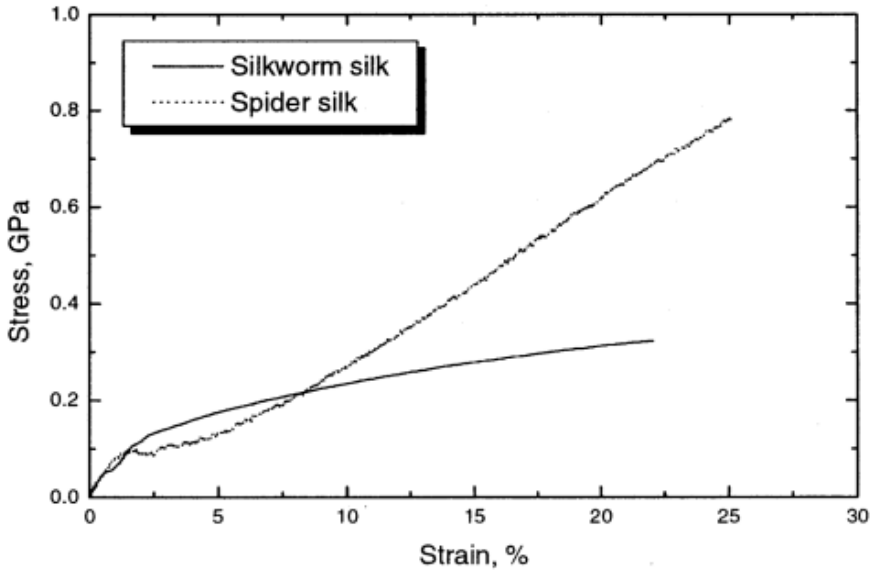

Figure 1.6 Typical stress-strain curve for the single filament of silkworm silk (*Bombyx mori*) along with that of spider silk (*Nephila edulis*) [52].

Intermolecular vs. intramolecular β-sheet crystallites. Essentially, the splitting of intermolecular β-sheet crystallites leads to weakening of the overall molecular network in silk, and thus results in failure of the

material. On the contrary, the splitting of intramolecular β-sheet crystallites leads to lengthening of silk as they split (i.e., unfold) [56,65]. The content of intramolecular β-sheet crystallites significantly influences the mechanical properties of silk. Evidently, the superb mechanical strength and toughness of spider silk (*Nephila pilipes*) have been attributed to its high content of intramolecular β-sheet crystallites [56]. Spider silk has a content of about 57% of intramolecular β-sheet crystallites (of total β-sheet crystallites content), significantly above that of silkworm silk (18%). A possible explanation for the lower content in silkworm silk is that the H-chain has comparatively larger crystal-forming domains [55], which increase their likelihood of interactions with those from neighboring H-chains to form intermolecular β-sheet crystallites when the domains are well-aligned during spinning [71]. With this understanding, the mechanical properties of silkworm silk may be further enhanced if there is a way to increase the amount of the intramolecular β-sheet crystallites in silk fibroin.

Parallel vs. antiparallel β-sheet crystallites. Different arrangements of β-strands in β-sheet crystallites, i.e., parallel vs. antiparallel, have been proposed. When arranged in parallel sense, adjacent β-strands form lengthier and non-linear hydrogen bonds, whereas antiparallel adjacent strands are able to form shorter and linear hydrogen bonds [42]. The arrangement of the β-strands thus influences the mechanical properties owing to the geometrical and energetic differences in the hydrogen bonding. Mechanical properties of poly(GA) crystalline units, in both parallel and antiparallel arrangements, have been simulated to compare any difference in mechanical properties (Figure 1.7a). It was found that antiparallel β-sheet crystallites outperform the parallel counterparts, in terms of rupture strength and stiffness, as shown in Figure 1.7b. Experimental stress-strain data of silk fiber is also presented (green curve), and is of lower strength and stiffness than the simulation data. This is because the experimental result was calculated using cross-sectional area of fiber, which includes also the area contribution from semi-amorphous region, in addition to the β-sheet

crystallites. Meanwhile, it was also reported that the hydrogen bonds are stronger in the antiparallel arrangement [68].

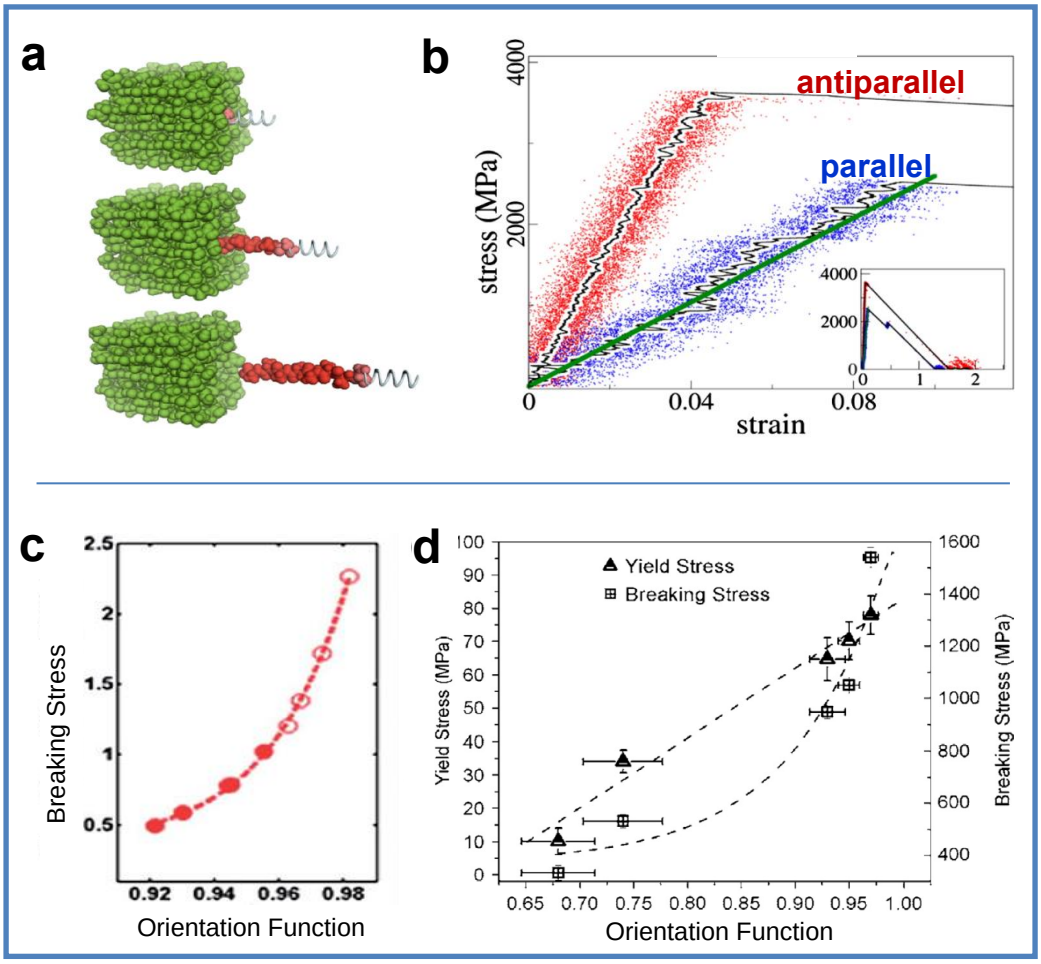

Figure 1.7 Mechanical properties of poly(GA) crystalline units from molecular dynamics simulations. (a) Simulation snapshots of the rupture process. Crystalline unit is in green with the pulled strand in red. The pulling force is depicted as a spring. (b) Stress-strain plots of the parallel (blue) and antiparallel (red) crystalline units (solid black curves for averages), with experimental result (green) in comparison. The inset shows the complete extension and rupture process [68]. (c) Relation between orientation function and breaking stress of silkworm silk fibers predicted based on a hierarchical network model. The solid circles indicate the orientation function values (*f*) from force-spun silkworm silk while higher values are represented by hollow circles (f = 0 for no preferred orientation; f = 1 for perfect orientation) [77]. (d) Relation between orientation function and breaking stress of spider dragline silk [67].

Size of β-sheet crystallites. The size of β-sheet crystallites has been investigated using both XRD and TEM. The reported crystallite dimensions of both silkworm and spider silk are listed in Table 1.2 along with several other structural parameters [56,72–75]. So far, there has been no reported experimental research to correlate the size of β-sheet crystallites to the mechanical properties of silkworm silk fibroin fibers. Instead, molecular modelling and simulation have been used to provide insights on the crystallite size-mechanical property correlation of silk fibroin [58]. Recent modeling and simulation studies showed that confining the dimensions of β-sheet crystallites to a few nanometers is mechanically advantageous [58,64]. Keten et al. [58] performed a series of large-scale molecular dynamics simulations to explore the size effect of *Bombyx mori* silkworm β-sheet crystallites on their mechanical properties (Figure 1.8a). Their findings indicated that the mechanical properties of silk are strongly dependent on the β-sheet crystallite sizes. It was found that β-sheet crystallites that are confined to a few nanometers can achieve higher strength, stiffness and toughness than larger β-sheet crystallites, as shown in Figure 1.8b [58]. The reported critical dimensions of crystallite for optimal mechanical properties are 2–4 nm along interchain direction and 1–2 nm along the strand axis (Figure 1.8c). Similar findings were also reported for spider silk β-sheet crystallites, whereby an increase in the strength and toughness was observed when the size was reduced from 10 to 6.5 nm, and further reduced to 3 nm [64]. The reason being that, larger β-sheet crystallites experience predominantly bending deformation, whereas smaller β-sheet crystallites experience predominantly shear deformation. Through nanoconfinement, a combination of uniform shear deformation that makes most efficient use of hydrogen bonds and the emergence of dissipative molecular deformation leads to significantly enhanced mechanical properties of β-sheet crystallites [58,64].

Table 1.2 Structural parameters of silk fibers [56,72,73–75].

Silk	Crystalline content (%)	Crystallite size[+] (nm)			Ref.
		a	b	c	
Silkworm cocoon silk (*Bombyx mori*)	40	4.1	2.3	10.3	[56]
Silkworm silk fibroin (*Bombyx mori*)	55	3.26	4.14	12.4	[74]
Silkworm silk fibroin (*Bombyx mori*)	27	4.8	1.6	20.4	[73]
Silkworm silk fibroin (*Bombyx mori*)	–	3.82	3.2	10.76	[72]
Spider dragline (*Nephila clavipes*)	22	2.7	2.1	6.5	[56]
Spider dragline (*Nephila clavipes*)	–	2	5	6	[75]

[+] **a** is the direction along the stacking of β-sheets, **b** is the direction in a β -sheet perpendicular to the strand axis, and **c** is the direction along the strand axis.

Orientation of β-sheet crystallites. The β-sheet crystallites in silk fibers are known to be highly oriented along the fiber axis [76]. The relation between the crystallite orientation (measured by orientation function value, *f*) and breaking stress of silkworm and spider dragline silk fibers have been investigated, respectively using modeling [77] and experimental studies [67]. Typically, a higher orientation of β-sheet crystallites along fiber axis contributes to a higher breaking stress (Figure 1.7c–d). Presumably, the more oriented β-sheet crystallites are better positioned to sustain tensile load along the fiber axis [67]. Naturally spun silkworm silk (spinning speed 4 to 15 mm s^{-1}) has been reported to have orientation function *f* of 0.84 [73], while the silk force-spun at the natural spinning speed is more oriented (*f*=0.93 to 0.94). Furthermore, a range of different crystallite orientations have been

obtained by force-spinning the silkworm silk at different speeds (1–27 mms^{-1}). Typically, a higher spinning speed better orients the crystallites along the fiber axis (Table 1.3) [77]. A similar trend was also observed for spider silk [67,77].

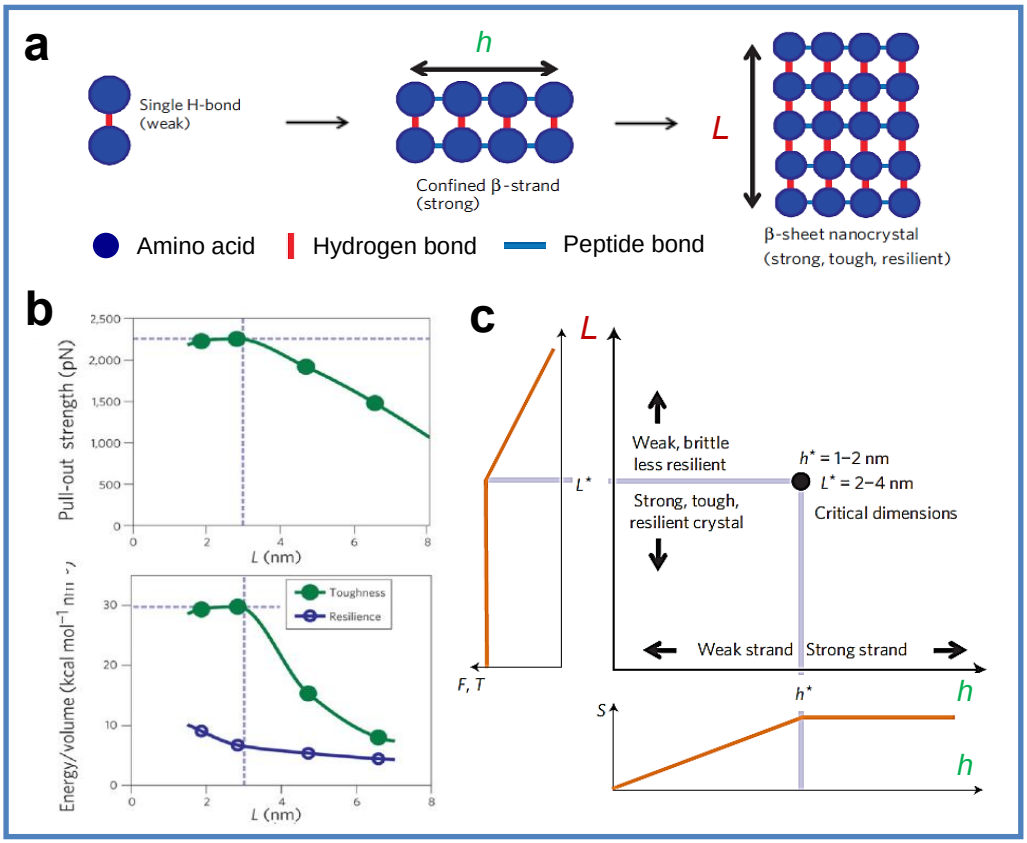

Figure 1.8 Size effects on mechanical properties of silkworm *Bombyx mori* β-sheet crystals from modeling and simulation. (a) Hierarchical structure of β-sheet crystal that combines strength, toughness and resilience, despite being composed of structurally inferior, weak building blocks, hydrogen bonds (*h*: strand length; *L*: β-sheet size). (b) Variation of strength, toughness and resilience (i.e., elastic energy storage capacity) of β-sheet crystal as a function of crystal size *L*. (c) Schematic phase diagram to show the interplay of the parameters *h* and *L* in defining the properties of crystallites, together with (bottom) schematic plot of the strength (*S*) of crystal as a function of strand length *h*, and (left) schematic plot of the strength (*F*) and toughness (*T*) of crystal as a function of *L*. Nanoconfinement of β-sheet crystal at critical strand length h^* and critical β-sheet size L^* provides maximum strength, toughness and stiffness [58].

Table 1.3 Crystallite sizes and orientations of silk fibers as a function of force-spinning speed [67,77].

Silk	Spinning Speed (mm s^{-1})	Crystallite size (nm)			Orientation function (*f*)	Ref.
		a	b	c		
Silkworm silk fibroin (*Bombyx mori*)	1	2.63	3.20	11.65	0.922	[77]
	4	2.57	3.18	11.48	0.930	
	13	2.55	3.17	11.49	0.944	
	20	2.55	3.16	11.49	0.945	
	27	2.54	3.15	11.49	0.956	
Spider dragline (*Nephila species*)	1	2.40	3.50	7.30	0.680	[67]
	2.5	2.30	3.40	7.10	–	
	10	2.10	2.70	6.50	0.940	
	25	2.20	2.70	6.40	–	
	100	2.10	2.70	6.40	0.970	

1.3.2 Enhanced mechanical properties

The mechanical properties of silkworm silk are not entirely limited by its constituent and natural production. The mechanical properties of silk fibers are highly dependent on various factors aside from the intrinsic structure. These factors include fed food, rearing conditions and health of silkworms, as well as spinning process variation and genetic modification of silkworms. Table 1.4 lists the mechanical data of silk fibroin matrices constructed directly from silk fibers [14–16,78,79].

The food quality and rearing conditions greatly influence the health level of silkworms, which in turn influence the mechanical properties of produced silk [80–82]. In terms of food source, mulberry leaves are the only practical feed for *Bombyx mori* silkworms. Mulberry leaves contain mainly water along with a rich source of protein and carbohydrates, and the quality is subjected to the influence of various factors such as

plant species, position of leaves (extent of exposure to sunlight), ripening stage of the leaves, soil quality, etc. Feeding on good quality fresh mulberry leaves ensures good health of the silkworms to produce mechanically superior silk. Besides, artificial diet containing mulberry leaf powder (with high nutritional value preserved through refrigeration during storage) is also suitable for feeding silkworms. Meanwhile, rearing conditions including temperature and humidity have been reported to affect the assimilation of food in silkworms, and thus influence their health to a large extent. Specifically, silkworms that are fed with good quality mulberry leaves, reared at high temperature (e.g., 28°C) along with high humidity (e.g., 70–90%) during early stages/instars, and reared at lower temperature (e.g., 23–24°C) along with low humidity (e.g., 65–70%) during late stage (i.e., the fifth instar), are known to produce mechanically superior silk [81,82]. On the contrary, poor food quality and suboptimal rearing conditions result in various illnesses and diseases which hinder the production of high quality silk.

The spinning of silk fibers takes place via the extrusion of the silk dope stored in glands through the spinnerets of silkworms into the external environment by mechanical shearing, stretching, and continued evaporation of water [4,7]. It is understood that the delicate gland conditions in vivo (i.e., silk dope acidification, concentration change of metal ions, and water content reduction) play critical roles in the proper folding of fibroin from gel to micelles and finally liquid crystals, leading to the production of mechanically superior silk fibers [3,4,7]. In addition, variation in temperature, humidity [80], drawing rate [54], and absence/presence of electric field [73] during spinning are also known to greatly affect the mechanical properties of silk. Being a photosensitive insect, *Bombyx mori* silkworms also react to light. It was reported that the spinning process slows down significantly in complete darkness and the resulting silk quality is inferior [82]. Here, the natural spinning process is described, followed by two modified spinning

processes (i.e., by applying external force or spinning in electric field) as well as gene transfection to obtain enhanced silk.

Natural spinning. Silkworms extrude silk naturally at speeds oscillating between 4 to 15 mm s^{-1} by moving their heads in 'figure of eight' motion [54]. Just prior to leaving the silk glands, the silk dope (containing up to 30% wt/vol fibroin in water) exists as a water-soluble liquid crystalline state which ensures a low viscosity for easy spinning through the spinnerets into external environment. Being a liquid crystalline state, the viscosity of the silk dope is independent on environmental temperature [83]. However, the temperature is known to affect the spinning rate of silkworms, a temperature range of 22–25°C is favorable during spinning. Additionally, a humidity level of 60–70% is favorable during spinning [82].

Table 1.4 Mechanical data of various silkworm silk fiber matrices [14–16,78,79].

Matrices	**Young's Modulus (GPa)**	**Load (N)**	**Breaking Strain (%)**	**Ref.**
Nonwoven mats				
wet	0.035–0.075	–	36–55	[16,78,79]
dry	0.45–0.70	–	25–34	
Braided cords (parallel bundle)	1740+	2214	26.5	[14]
Braided cords (wire-rope bundle)	354+	2337	38.6	[14]
Knitted mats	45–50+	252–257	~50	[15]

+ Values expressed indicate stiffness (N/mm) rather than Young's modulus.

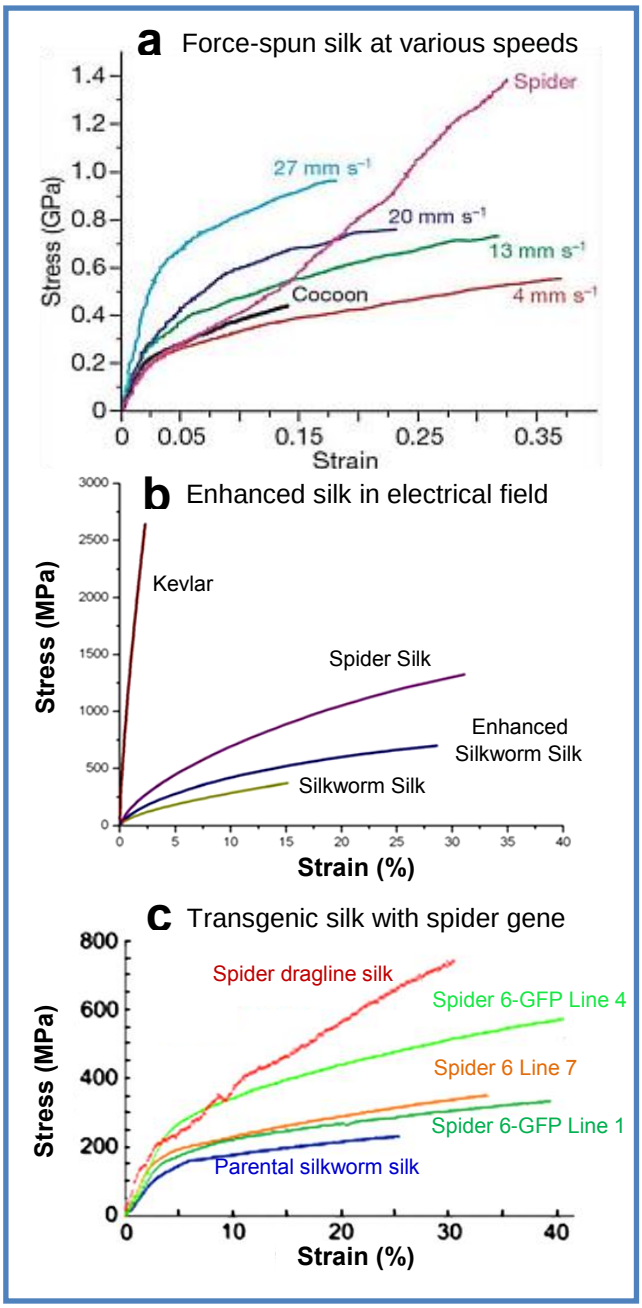

Figure 1.9 Stress-strain curves of mechanically enhanced *Bombyx mori* silk fibers. (a) Degummed silks obtained by force-spinning at speed 4, 13, 20 and 27 mm s^{-1}, as compared to *Nephila* spider dragline silk (20 mm s^{-1}) and degummed cocoon silk spun naturally by *Bombyx mori* silkworm at speeds oscillating between 4 and 15 mm s^{-1} [54]. (b) Degummed silk produced by *Bombyx mori* silkworm placed in an alternating electric field during spinning (blue curve) [73]. (c) Degummed genetically-modified silk containing spider silk sequence (*Nephila clavipes)*. The best mechanical performances measured for the parental silkworm silk and representative spider dragline silk are compared with those produced by genetically-modified silkworms at different lineages (spider 6-GFP Line 1 and 4, spider 6 Line 7).

1.3.2.1 Enhanced silk

Force-spinning at a controlled drawing rate. When silkworms are being immobilized, the silk can be artificially drawn by external force (i.e., force-spinning) to achieve superior mechanical properties, including strength, toughness and extensibility. Such force-spinning extrudes the silk at a constant speed and in a single direction, thereby eliminating any inconsistencies associated with the natural spinning (i.e., 'figure of eight' spinning motion). Different force-spinning speeds were applied to obtain silk with greatly enhanced breaking strain as compared to naturally spun counterpart (Figure 1.9a) [54]. It was reported that slow force-spinning (e.g., 4 mm s^{-1}) produced highly extensible silk with breaking strain comparable to that of *Nephila* spider silk, whereas fast force-spinning (e.g., 13 mm s^{-1}) resulted in stronger and tougher silk with breaking stress and toughness approaching that of *Nephila* spider dragline silk.

Modulated spinning in electric field. When silkworms spin in alternating electric field, the silk produced are stronger, tougher and more extensible than naturally spun silk, as shown in Figure 1.9b. The enhanced silk fibers have β-sheet crystallites more oriented along the fiber axis, while the crystallinity and crystallite sizes are similar to that of naturally spun silk [73]. This strategy for enhancing the mechanical properties is based on the use of electric field to align the liquid-crystals (i.e., the water-soluble liquid crystalline state) of silk fibroin in the silk gland. Electric field has been shown to be able to align protein dipoles along the direction of the field [84]. The better oriented β-sheet crystallites are thus able to withstand the higher load applied along the fiber axis upon stretching during tensile test.

Gene transfection. The gene sequence of spider silk (e.g., *Nephila clavata or Nephila clavipes*) has been successfully transfected into silkworms via *piggyBac* vector, and this has enabled its co-expression in silk glands of the transgenic silkworms [85,86]. Even at low expression level, the genetically-modified silk has an overall improved

mechanical performance (Figure 1.9c). It is noted that the favorable effect could also be observed through subsequent silkworm lineages, occasionally with highly enhanced effect. Successful incorporation of the guest proteins into the silk requires that their expression occurs in spatial and temporal proximity to the endogenous silk proteins [85,86]. Besides, successful gene transfection relies greatly on environmental and genetic factors and thus explains the low rate of attaining the desired phenotypic expression [86].

1.3.2.2 Enhanced regenerated silk

There are several ways to influence/enhance the mechanical properties of regenerated silk. Degummed silk fibers are often dissolved into fibroin solution and reconstructed into regenerated silk morphologies for increasing use in various applications. Regenerated silk can generally be classified into four morphological types, i.e., sponges, hydrogels, films, and mats. Table 1.5 lists the mechanical data of various regenerated silk fibroin morphologies [87–96]. The mediocre mechanical properties of regenerated silk as compared to native silk fibers are often attributed to the protein degumming and dissolution processes, during which some level of chain hydrolysis inevitably occurs. Be that as it may, the mechanical properties of the regenerated silk have been enhanced considerably through various processing strategies. Various factors, for examples, fibroin concentration, processing temperature, methanol/salt treatment, water annealing treatment, pore size/distribution, etc., are known to influence the mechanical properties of fibroin regenerated silk and can thus be adopted as strategies for mechanical enhancement. Besides, fibroin can also be physically blended or chemically cross-linked with guest polymers for mechanical enhancement. In the followings, relevant mechanical enhancement strategies are discussed for the individual morphological types.

Table 1.5 Mechanical data of various regenerated silk morphologies [87–96].

Morphologies[+]	**Pore size (μm)/ Porosity (%)**	**Young's Modulus (GPa)/ Stiffness (N/mm)**	**Ultimate Strength (MPa)/ Load (N)**	**Breaking Strain (%)/ Extension (mm)**	**Ref.**
Methanol-treated sponges (concentration 6 wt%)	151±40 (87.6%)	0.00043 GPa^	0.02 MPa^	–	[87–89]
HFIP-derived sponges (concentration 17 w/v%)	15–202	0.00045–0.001 GPa^	0.175–0.25 MPa^	–	[90]
Aqueous-derived sponges (concentration 4 w/v%)	940±50 (95%)	0.00007 GPa^	0.011 MPa^	–	[91]
	650±30 (97%)	0.0001 GPa^	0.012 MPa^	–	[91]
	470±30 (97%)	0.00013 GPa^	0.013 MPa^	–	[91]
Aqueous-derived sponges (concentration 8 w/v%)	920±50 (92%)	0.0013 GPa^	0.1 MPa^	–	[91]
	750±20 (94%)	0.00153 GPa^	0.125 MPa^	–	[91]
	640±30 (95%)	0.00194 GPa^	0.14 MPa^	–	[91]
Aqueous-derived sponges (concentration 10 w/v%)	920±50 (85%)	0.00333 GPa^	0.32 MPa^	–	[91]
Hydrogels (concentration 8% w/v)	–	–	0.0252 MPa^	–	[92]
Films (as cast)	–	3.9 GPa	47.2 MPa	1.9%	[93]
Films (methanol-treated)	–	3.5 GPa	58.8 MPa	2.1%	[93]
Films (water-annealed)	–	1.9 GPa	67.7 MPa	5.5%	[93]
Films (ultrathin, i.e., 20–100 nm; spin coating and spin-assisted layer-by-layer assembly)	–	6–8 GPa	100 MPa	0.5–3%	[94]
Electrospun mat (concentration of 3%, electric field of 1 kV/cm and 10-15 cm spinning distance)	–	–	15 MPa	40%	[95]
Electrospun mat (concentration of 15%, electric field of 2 kV/cm and 5 cm spinning distance)	–	0.515	7.25 MPa	3.2%	[96]

[+] Concentration values refer to that of fibroin solution used to prepare the morphologies.

^ Compression instead of tensile mechanical test results.

Fibroin sponges. Fibroin sponges are usually prepared from fibroin solution by freeze-drying and particles-leaching using porogens (e.g., salt crystals, sugar crystals or paraffin beads) [87–91,97,98]. Several factors known to affect the mechanical properties are initial fibroin concentration and methanol/salt treatment during sponge fabrication, as well as the resulting pore size and distribution of the sponges. Firstly, a higher initial concentration of fibroin solution leads to a molecular network which is more tightly packed, and thereby results in stronger and stiffer sponges. Secondly, methanol/salt treatment is used to induce molecular crystallization into β-sheets so as to impart water stability and mechanical integrity to the sponges. Thirdly, smaller pore size comes with more closely distanced/situated pore walls which act to stop crack propagation, and thus also results in stronger and stiffer sponges. Lastly, a uniform distribution of pores within the sponges allows for more homogeneous distribution of mechanical stresses, which facilitates their effective dissipation and thus results in mechanically enhanced fibroin sponges. For example, fibroin sponges, which are aqueous-processed, have more homogeneous/uniform pore distribution, and hence are mechanically more superior to non-aqueous solvent (HFIP)-processed counterparts [11,91].

Fibroin hydrogels. Fibroin hydrogels are formed via sol-gel transition through the aggregation of fibroin molecules into β-sheets or cross-linking of fibroin molecules to form an interconnected network in aqueous solution. The gelation is induced upon heat/cold treatment, mechanical agitation/sonication, pH change, and/or cross-linking using ionic species such as Ca^{2+} ions [92,99–101]. Increasing the initial concentration of fibroin solution results in hydrogels with enhanced compressive strength, modulus and strain. This is due to more tightly packed fibroin molecular network and reduced pore size, which help in stress distribution. Increasing the gelation temperature similarly leads to enhanced mechanical properties due mainly to reduced pore size. Meanwhile, cross-linker species/concentration, gelation pH, and degree of swelling can also affect the mechanical properties.

Fibroin films. Fibroin films are prepared by dry-casting, spin-coating, or spin-assisted layer-by-layer assembly techniques [93,94,102–105]. Dry-casted fibroin films are weak both in terms of strength and breaking strain [104], and are especially brittle in dry state [102,105]. Meanwhile, spin-coating and spin-assisted layer-by-layer assembly methods are able to produce ultrathin (tens of nanometers) and mechanically robust free-standing silk fibroin films with superior ultimate tensile strength (~100 MPa) and toughness (328 kJ m^{-3}) rivaling many conventional polymer composites (<100 kJ m^{-3}) [94]. Such films result from the physical formation of β-sheets during the spin coating process without requiring any chemical cross-linking reactions. However, the brittleness of fibroin films (breaking strain of 0.5–3% [94]) is still a major limitation hindering its practical use. One strategy known to produce non-brittle fibroin films is the water-annealing technique (i.e., long hours of immersion in water or exposure to water vapor). Water-annealing of casted fibroin films has resulted in reduced β-sheet content (i.e., three-fold less β-sheet content than methanol-treated films [106]) as well as highly organized molecular packing, both of which collectively render the films stronger and more extensible (i.e., stretchy) [93]. The mechanical properties of water-annealed films can be regulated by controlling the temperature during water-annealing, i.e., a lower temperature treatment (e.g., 4°C) produces softer and more stretchy films due to lowered crystallinity, whereas a higher temperature treatment (e.g., 95°C) produces stiffer and stronger films due to increased crystallinity [107].

Fibroin mats. Electrospun fibroin mats are fabricated by spinning silk fibroin solution into micro- or nanofibers in an electric field. The mechanical properties of the fibers are greatly influenced by solvents system (e.g., methanol, formic acid), fibroin concentration, electric field strength, and spinning distance (i.e., distance between spinneret and collecting plate) [95,96]. AFM studies showed that the stiffness of fibroin-based nanofibrous matrix can be enhanced by decreasing the spinning distance, while the flexibility can be enhanced by increasing

the spinning distance [108]. The weaker mechanical properties of the electrospun fibroin mats may be attributed to the unrealized orientation at both the molecular and fibrillar levels. Several processing strategies such as fiber drawing, aligning, and annealing may be helpful for attaining mechanically robust electrospun fibroin mats [96].

Blended/cross-linked fibroin with guest polymers. Natural polymers (e.g., cellulose, chitosan, polyacrylamide, sodium alginate and sodium poly-glutamate) and synthetic polymers (e.g., polyethylene oxide, polyurethane, polyvinyl alcohol and nylon 66) are popular guest polymers to enhance the mechanical properties of regenerated fibroin [87,105,109,110–113]. Physical blending of fibroin with natural polymer such as recombinant collagen gives rise to sponges which have compressive stress ~33 times higher than pure fibroin sponges, along with enhanced biocompatibility [87]. Furthermore, blended fibroin-cellulose films have both enhanced strength and ductility (i.e., up to ten-fold increase in the extensibility). The improved mechanical properties were respectively attributed to the presence of intermolecular hydrogen bonding between cellulose and fibroin, and the intrinsic hygroscopicity of cellulose [105]. In another case, polyacrylamide was first cross-linked with N,N’-methylenebisacrylamide to form an interconnected network, which allows fibroin chains to form mechanically more superior hydrogels through hydrogen bonding to the network [111]. These examples demonstrated that polymer blending is a good strategy to enhance the mechanical properties [104]. Besides physical blending, chemical cross-linking strategy involving guest-polymer has been adopted to enhance the mechanical properties of regenerated fibroin by selecting guest polymers that possess functional groups for covalent cross-linking with fibroin [11,112]. For instance, fibroin-collagen hydrogels cross-linked by 1-ethyl-3-(3-dimethylaminoprophy) carbodiimide hydrochloride are mechanically superior to pure fibroin hydrogel as well as most other protein-based hydrogels [113].

1.4 Functionalization of Silk

To expand the use of silk fibroin, it is often required to introduce new functionalities through the incorporation of various functional components in the material. Some examples of functional components include drugs, peptides, proteins (e.g., fluorescent proteins, antibodies, growth factors, enzymes, haemoglobin) [11,34,112,114], metals/semiconductors and their nanoparticles [9,115–117], conductive polymers, etc. The functionalized silk can effectively direct/impart cellular response, antibacterial activity, stimuli-responsive ability, therapeutic effect, electrical conductivity, specific optical properties, and/or sensing functions [11,19,112,118,119]. In most cases, it is always desirable to introduce functionalities into silk while preserving its superior inherent features such as the high mechanical strength and toughness.

Genetic modification has been successfully applied to produce fluorescent colored silk [120]. A gene vector was constructed for inserting fluorescent color gene into the silkworm genome. In the vector, the color gene is bound on both ends by the N-terminal and C-terminal gene sequence of the fibroin H-chain, which enables its binding to the fibroin L-chain via a disulphide bond. This binding consequently allows its co-expression in the silk glands together with silk fibroin protein to produce transgenic fluorescent colored silk cocoons (Figure 1.10a). The mechanical strength of the red colored fluorescent silk is about 14% higher compared to the control (Figure 1.10b), whereas the introduction of the green and orange fluorescent proteins in the silk results in a slight decrease in their mechanical strength [120].

On the other hand, ready-produced fibroin fibers or regenerated fibroin [19] have been functionalized through functional component incorporation and/or morphological molding/surface topological patterning. Firstly, the incorporation of functional components to silk fibroin is done through physical adsorption or chemical cross-linking, which can have an effect on the mechanical properties. There are

some examples to illustrate the indefinite mechanical influence of post-functionalization through functional component incorporation. It was reported that the chemical cross-linking of TiO_2 onto silk led to a significant drop in the tensile strength and a rise in stiffness of silk [117]. In comparison, the physical adsorption of TiO_2 onto silk resulted in significantly enhanced mechanical properties including the modulus, ultimate tensile strength, breaking strain and toughness [121]. Besides, another study reported that fluorescent silk fibers prepared via physical dye adsorption have similar breaking stress, strain, and energy to those of unmodified silk [122]. Meanwhile, electrospun silk mats coated with conductive polymer (e.g., polypyrrole) supported higher load as compared to the non-coated counterpart [123]. These findings indicate that the choice of functional components and the associated functionalization process can significantly influence the mechanical properties of silk. In addition, it is also important to take into consideration of the nature and concentration of cross-linker(s) as well as other conditions (e.g., pH and temperature) used during the functionalization process [124].

Secondly, silk fibroin in regenerated forms can be functionalized using soft lithographic technique (i.e., micro-molding). For example, regenerated silk solution was molded to fabricate needle-like morphology by micro-molding technique, providing an advanced option/route for drug delivery [18]. From the mechanical point of view, cone-shaped microneedles were reported to be stronger than pyramid-shaped microneedles. The functional microneedles were additionally subjected to water vapor annealing for enhancing their mechanical strength. Silk microparticles were also embedded into silk microneedles to further increase the mechanical strength at higher drug load [125]. In another example, regenerated silk solution was molded to fabricate films with topologic patterns by micro-molding technique [19,20,118,119]. This produces mechanically robust functionalized films with features such as air holes or linear/concentric surface grooves on the order of nano/micro-scale, which improve

extracellular matrix production, guide cellular alignment, diffract light, etc. During the functionalization process, however, the mechanical stress imposed during the peeling of the silk films from the master generated undesirable artifact (i.e., smudging/distortion of patterns). This can be overcome by allowing the film to float off the master facilitated by the use of surfactants [119].

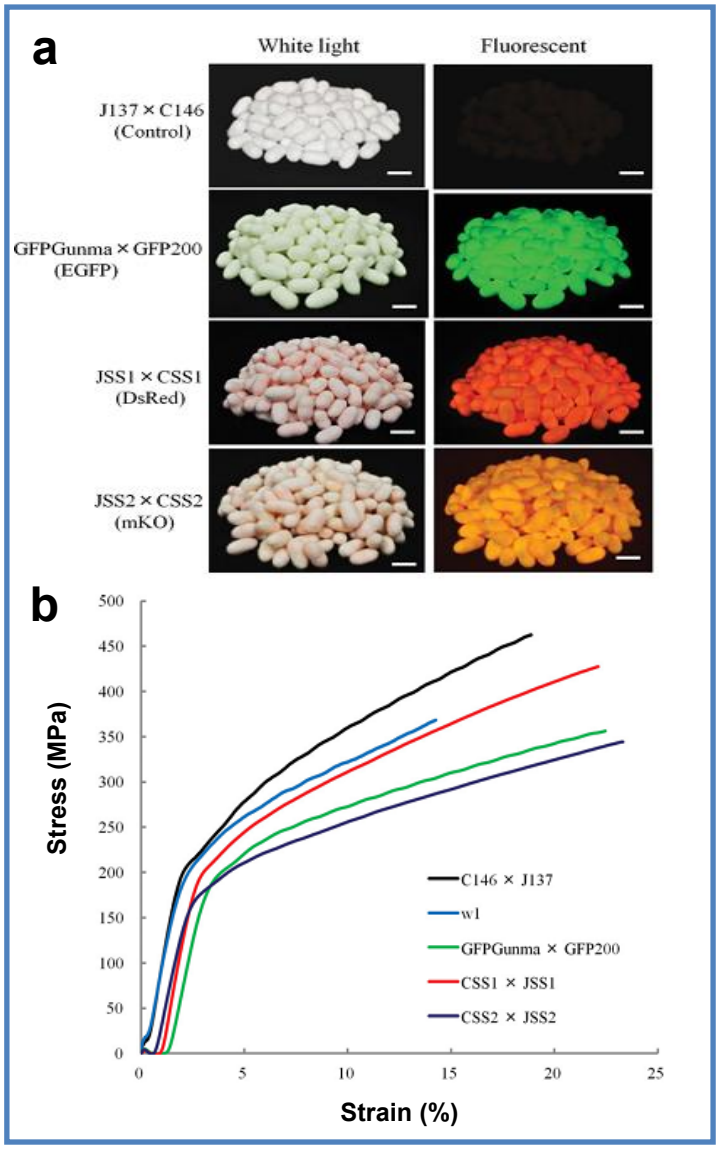

Figure 1.10 Genetically modified fluorescent colored silk (*Bombyx mori*). (a) Optical and fluorescent images of the fluorescent colored cocoons (green (EGFP), red (DsRed-M), and orange (mKO) silk) exposed under white light and a blue LED (imaged through a yellow filter), respectively. (b) Stress-strain curves of the fluorescent colored silk fibers produced by genetically modified strains compared to control (w1) and commercial race (C146 x J137) [120].

1.5 Applications of Silk

A great variety of applications have been demonstrated to utilize the numerous favorable intrinsic properties of silk fibroin, including its lustrous appearance, smooth texture, good biocompatibility/biodegradability, versatile processability, ease of functionalization, thermal stability, etc. Most notably, many applications take advantage of its excellent mechanical properties, besides benefiting from the low-cost and abundant supply of the material. Today, silk fibroin is a valuable textile material, and also an attractive biomaterial in various medical/pharmaceutical fields, mainly tissue engineering, drug delivery, optics, sensing, diagnostics, etc. In the following, the applications of silk fibroin are discussed from the mechanical perspectives.

1.5.1 Textile

Selection and design of materials for use as textile are greatly dependent on their aesthetic appeal and functional performance [126]. Today, there are different natural (i.e., silk, cotton and wool fibers) and synthetic (e.g., polyamide, polyester and polyacrylic fibers) materials available for use as textile. Among them, silk fibroin fibers are outstanding with exceptionally lustrous/fine appearance, soft-to-touch texture, ease of dyeing, superior mechanical properties, good biocompatibility and impressive moisture-absorption abilities. So far, silk fibroin still remains as an attractive textile choice, particularly for fashion apparel, luxury clothing (e.g., shirts, ties and formal dresses) and furnishings (e.g., upholstery and beddings).

Conventional incorporation of colors into textiles requires harsh dyeing conditions (e.g., elevated temperature and extreme pH) followed by multiple washing/rinsing steps to clear excess dyes, which not necessitate a great deal of water and energy, but also deteriorate the structures and thus the original properties of silk fibers. Besides, the silk can also be coated or covalently attached with antibacterial agents

(e.g., silver nanoparticles, TiO_2@Ag nanoparticles, etc.) to achieve decent antibacterial activity (e.g., against *Escherichia coli*, *Staphylococcus aureus,* and *Pseudomonas aeruginosa* bacteria), along with UV protective effect and self-cleaning ability [116]. Due to the favorable intrinsic properties and such facile incorporation of color, antibacterial, sunscreen and self-cleaning properties, the silk is increasingly sought after as the material of choice in the development of antibacterial apparel, sportswear, military uniforms, filtration fabrics, cosmetic textiles and therapeutic/surgical/medical textiles [126–128]. More often than not, these diversified textile applications place considerable demands on the mechanical performance of silk to provide mechanical protection/support, resist wear and tear, etc. Manifestly, these applications also created the demands for silk fibers with mechanical properties to satisfy varying requirements in terms of the stiffness/flexibility of the textile.

1.5.2 Surgical suture

With desirable combination of high strength, low bacterial adherence and good handling/tying characteristics, silk fibroin is a commonly used suture material, which is absorbable after 60 days *in vivo* [2,129–131]. Silk is typically braided when used as suture, rendering it susceptible to inducing inflammatory reactions [132]. In comparison, the use of non-braided sutures usually reduces the incidence of inflammatory reactions due to the smoother surface and the absence of grooves for adherence of inflammatory-causing substances (i.e., mainly immune cells such as neutrophils, lymphocytes, fibroblasts, histiocytes and giant cells) [133]. The foreign body response following implantation in vivo has been reviewed for the commonly available sutures in the market [2]. It follows that the use of non-braided silk suture is desirable, and this inevitably demands a stronger and tougher silk, which is expected to be obtained from the efforts in the mechanical enhancement of silk.

1.5.3 Tissue engineering

Silk fibroin possesses superior mechanical properties, which can readily meet the mechanical requirements of tissue engineering scaffolds to provide a stable template for tissue regeneration including ligament, tendon, cartilage, bone, skin, liver, trachea, nerve, cornea, eardrum, bladder, etc. [30,134,135]. The use of fibroin as tissue engineering scaffolds requires that their mechanical properties resemble those of the original tissue, in order to render good biomechanical compatibility and support. The construction of fibroin into different matrices/morphologies offers a wide range of useful mechanical properties for the regeneration of various human tissues (Tables 1.4 and 1.5). The numerous choices of fibroin matrices/morphologies along with the versatile processability thus provide diverse options for tailoring their mechanical properties to match those of the respective tissues, ranging between the values of hard and soft tissue [14,91,136–140]. Particularly for load bearing applications, the ultimate tensile strength of the tissue engineered construct should exceed the stress experienced during normal human activity, whereas the Young's modulus should not exceed that of the original tissue so as to avoid stress shielding (e.g., in bone tissue) [25,141,142]. Besides supporting the load, the mechanical properties of the scaffolds (e.g., stiffness) are also known to influence cellular behaviors (e.g., adhesion, proliferation, and function) [143–146].

1.5.3.1 Non-woven and woven silk scaffolds

Silk fibroin fibers can be fabricated into non-woven or woven matrices for use as tissue engineering scaffolds. Typically, to form non-woven matrices, silk fibers are degummed followed by acid partial dissolution of fiber surface and subsequent crosslinking between fibers into non-woven mats. Whereas to form woven matrices, silk fibers are degummed followed by braiding, or first knitted followed by degumming, into braided cords and knitted mats respectively.

Non-woven mats. Non-woven mats of silk fibroin have large fiber surface area, rough surface topography, high porosity and pore interconnectivity [33,78], which are favorable for cellular attachment and tissue regeneration. Besides, the mats demonstrated substantial ability to induce vascularization in regenerating tissue [16,79]. For instance, the mats guided formation of vascularized reticular connective tissue in vivo with no traces of fibrosis. The numerous attractive features of non-woven mats as tissue engineering scaffolds have seen its use in the regeneration of a range of tissues (e.g., vascular tissue, epithelial tissue, reticular connective tissue, fibroblast tissue, glial tissue, keratinocyte tissue, osteoblast tissue) [16,79]. Consequently, there is a need to optimize the mechanical as well as morphological properties according to the specific requirements of individual tissue types [147].

Braided cords. Braided cords of silk fibroin were fabricated to closely mimic the hierarchical arrangement of collagen fibers in native ACL. The braided cords are sufficiently tough to withstand cyclic loading experienced by ACL tissue in daily activities [14]. Besides, the braided cords also exhibit triphasic load deformation, typically observed for native ACL, which is necessary for prevention of damage due to creep and fatigue [148]. When seeded onto the braided cords, human bone marrow stromal cells adhered, proliferated and differentiated into desired ligament tissues [14]. Nevertheless, as the braided cords provide only limited space available for cellular in-growth, nutrients infiltration and extracellular matrix deposition, they face significant challenges in maintaining long term viability of the tissue [15].

Knitted mats. Knitted mats of silk fibroin have generous openings favorable for the cellular in-growth, nutrients infiltration and extracellular matrix deposition. Supplementation of microporous silk sponges at the openings of the knitted mats can mimic an extracellular matrix environment to exert positive effects on the growth, differentiation and function of human mesenchymal stem cells (hMSC). Such combined knitted mats with sponges, when rolled into cylindrical

shape, have good mechanical properties that are potentially sufficient to withstand the loading of ACL during daily activities [15]. It is noted that the mechanical properties of knitted matrices can be further optimized, for example, by adjusting the yarn densities or via mechanical stimulations during the tissue culturing process [149].

1.5.3.2 Regenerated silk scaffolds

Regenerated silk solution can be used to prepare different morphologies including sponges, hydrogels, films and mats under all-aqueous processing conditions, which have good biocompatibility as tissue engineering scaffolds. The regenerated silk fibroin morphologies exhibit many attractive features such as large surface area, favorable surface texture smoothness/roughness and high porosities [91]. Despite being mechanically less superior when compared to native silk, the versatile processability of regenerated silk allows for mechanical enhancement through various strategies as described in Section 1.3.2.2. Mechanically enhanced regenerated silk morphologies possess good mechanical properties useful for various tissue engineering applications [11]. Furthermore, they can also be conveniently imbued with growth factors to stimulate, guide and/or accelerate tissue healing and growth [11,112].

Fibroin sponges. Fibroin sponges have high porosities of up to 97% (v/v) [91]. Highly porous sponges provide large interior surface area and interconnected pore spaces, allowing for cell anchorage, proliferation and migration, as well as nutrients and oxygen diffusion into the scaffold [11,33]. Fibroin sponges were shown to support the differentiation and growth of cartilage tissue-related cells, along with the secretion of extracellular matrices typical of cartilage tissue [88,89]. Besides, fibroin sponges attached with RGD sequence were also shown to favorably direct the proliferation and differentiation of human mesenchymal stem cells (hMSC) to express bone cells or chondrocytes phenotypes, along with cellular deposition of respectively

desired extracellular matrix [150,151]. Moreover, fibroin sponges formed in knitted silk scaffold were able to mimic an extracellular matrix environment to exert positive effects on cellular growth, differentiation and function [15]. Remarkably, the fairly homogeneous cell distribution and extracellular matrix accumulation achieved in fibroin sponges are helpful for maintaining mechanical integrity of the tissue construct and facilitating load transfer from scaffold to the regenerating tissue after implantation.

Fibroin hydrogels. Fibroin hydrogels have a high water content [152] that makes them physically and mechanically similar to natural soft tissues such as cartilage, skin and intervertebral disc [92,153], and thus are important tissue engineering scaffold materials. Being injectable, fibroin hydrogels are appealing as minimally invasive scaffolds [152]. Fibroin hydrogels have demonstrated ability to heal critical-size distal femur trabecular bone defects in rabbit model [154], specifically by inducing cellular proliferation and stimulating the expression of TGF-β1 (Transforming Growth Factor-β1), resulting in the formation of new trabecular bone formation with morphology close to normal physiological bone. In addition to facilitating a speedy bone healing and remodeling, the hydrogels also did not elicit any inflammatory reactions [154]. Recent studies on fibroin hydrogels have focused on improving the less than satisfactory mechanical properties of most fibroin-based hydrogels [111,113], which have limited their use in load-bearing applications.

Fibroin films. Given their high water and oxygen permeability [155], fibroin films are particularly appealing as wound dressings, skin or corneal replacement grafts [102]. It was reported that fibroin films induced a higher cell proliferation and lower inflammatory response as compared to collagen films [156]. Despite the brittleness (in dry state) of conventionally processed fibroin films, water/vapor-annealed fibroin films are mechanically robust in dry/hydrated state and have extremely smooth surface (<5 nm root mean square roughness), which enables

surface topographical patterning with features on the order of nano/micro-scale for directing cellular response and alignment [19,20,119]. The linear or concentric surface pattern has guided cellular alignment as well as enhanced extracellular matrix production and cellular function [19]. Above all, fibroin films can achieve extremely good optical transparency [93], essential for cornea tissue engineering. Along with surface topological patterning, fibroin films chemically attached with RGD peptide for corneal tissue regeneration resulted in well-aligned tissue architecture, giving rise to highly transparent and mechanically stable cornea tissue construct resembling that of native corneal tissue [19,20]. A stack of silk films, each pre-seeded with cells, can also be sturdily punched into three-dimensional construct mimicking the transparent stromal layer of the corneal tissue [21].

Fibroin mats. Electrospun non-woven mats demonstrated biomimetic features desirable for use as tissue engineering scaffolds. The nanofibrous electrospun mats have morphology mimicking the extracellular matrix of natural tissues and possess high surface area favorable for cellular attachment [157]. Fibroin-based electrospun mats of various stiffnesses were shown to modulate the migration, aggregation and differentiation of human mesenchymal stem cells (hMSC) into chondrocytes for cartilage tissue regeneration [158]. They were also shown to serve as a prospective scaffold for bone tissue regeneration by providing a favorable environment to support mineralized bone tissue formation [159]. When coated with conductive polymers (e.g., polyaniline, polythiophene and polypyrrole) to make them electrically conductive, the non-woven mats have a good electrical conductivity and are able to stimulate cellular growth when subjected to a low electrical field, which render them especially useful for guiding neutrite growth and extension [123]. With these favorable features, electrospun mats would make an ideal choice as scaffolds, given that the mechanical properties meet the tissue requirements.

1.5.4 Therapeutic agent delivery

The development of silk fibroin material for use as carriers of therapeutic agents (e.g., small molecular or protein-based drugs/growth factors) is advantageous due to its mild processing options, superior mechanical properties and excellent stabilizing effect [112,160,161]. The loaded therapeutic agents are subsequently delivered via various routes (i.e., localized, systemic, or cellular) to achieve the desired therapeutic effects. The mechanical roles of silk fibroin for controlled release and delivery applications are discussed in terms of the following three aspects.

1.5.4.1 Entrapment and protection of agents

Therapeutic agents are either surface loaded or bulk loaded in fibroin carriers depending on the amount of drug to be loaded and the required release kinetics in vitro/in vivo. In surface loading, the therapeutic agents are coated directly onto native/regenerated fibroin carriers. In bulk loading, they are entrapped into regenerated fibroin carriers [112,160,161]. Bulk loading is generally preferred over surface loading as it allows the loading of therapeutic agents at higher quantities. For bulk loading, therapeutic agents are first mixed into regenerated silk solution followed by fabrication into mechanically stable carriers (microparticles, sponges, films, etc.). The mechanical robustness can be achieved without the use of high temperature and UV-curing, through either aqueous processing condition or methanol treatment, thereby avoiding damage to the therapeutic agents [98] during carrier fabrication. The bioactivities of the entrapped therapeutic agents (e.g., enzymes, growth factors, antibodies) were not destroyed during the fabrication process [98,162]. Also, the entrapped enzymes (e.g., glucose oxidase, lipase, horseradish peroxidase) demonstrated significant bioactivities even after a long storage period of ten months [163,164].

1.5.4.2 Release of agents

With substantial amount of β-sheet crystallites in fibroin as mechanical barriers to the therapeutic agents, the entrapped agents can be gradually diffused out of the fibroin through the semi-amorphous regions between the β-sheet crystallites to achieve sustainable release with low initial burst. The release profile may be conveniently controlled by varying the β-sheet content and thus the crystallinity of the fibroin, as compared to other parameters such as the size and diffusivity of the agents, as well as the osmotic pressure [102,112,160,161,165,166–168]. With regards to this, however, any accompanying changes in the mechanical properties upon tuning of release profile have to be taken into consideration. On the other hand, there is a great interest to develop fibroin-based smart carriers, i.e., carriers that can offer controlled release profile in response to mechanical loading, which are particularly attractive for use in stimuli-sensitive/responsive applications [168].

1.5.4.3 Delivery of agents

Fibroin carriers can be employed for localized, systemic, or even cellular delivery of therapeutic agents. In these modes of delivery, the mechanical properties of fibroin carriers are known to play important roles.

Localized delivery. Localized delivery often requires the direct placement of fibroin carriers in contact with the targeted tissue/organs. This can be achieved through i) suture securing, ii) bioadhesion, or iii) transdermal piercing [18,169,170] by utilizing the good mechanical properties of fibroin: i) The implantable fibroin carriers have to be able to withstand suturing, and also sustain the tension of the surrounding tissue to which it is being secured to; ii) The bioadhesive fibroin carriers (e.g., in transmucosal delivery system) have to be mechanically robust to achieve good adhesion strength to the targeted tissue (e.g., mucous membrane) for delivering the therapeutic agents, and also offer

mechanical protection to them in some cases (e.g., ulcers and wound surfaces); iii) The transdermal fibroin carriers such as the fibroin microneedles have to be able to pierce through the skin without being fractured (i.e., fracture force>100 mN/needle) to deliver the therapeutic agents [18,171].

Systemic delivery. Systemic delivery typically requires the systemic circulation of carriers to eventually reach the targeted site. Fibroin carriers have been investigated for systemic delivery of therapeutic agents through injection, oral ingestion, or inhalation [172]. So far, there is no report regarding the influence of mechanical properties of fibroin carriers on biological responses. It was reported that the mechanical properties of carriers influence biological responses such as retention time in blood stream, immune response, and cellular internalization [173].

Cellular delivery. Cellular delivery normally requires the encapsulation/coating of cells within a semi-permeable matrix/barrier through which cell-secreted therapeutic agents (growth factors, etc.) can be diffused out and delivered to targeted tissue for imparting therapeutic effects [152,174,175]. Good mechanical properties of fibroin ensure the faithful encapsulation of cells, especially when mechanical stresses are induced upon injection to the targeted site, or present at the site of application [152,174,176]. A mechanically stable coating not only keeps the cells from being recognized by immune cells/antibodies thereby avoiding immune response, but also ensures steady release kinetics through the coating. Besides, it is feasible to tune the release kinetics through the coating while maintaining the essential mechanical properties [152].

1.5.5 Optics and sensing

Fibroin is being actively investigated for use as supporting and/or interfacial substrates in optics and sensors [25,103,177]. Fibroin has a higher refractive index than air, water and many other substrates,

rendering it extremely useful in confining and guiding the propagation of light wave [178]. The use of fibroin in optics and sensing is particularly appealing due also to its good combination of mechanical and lightweight properties, along with its biocompatibility and bioresorbability. Fibroin has been imbued with dyes/probes or patterned to generate various optical and sensing components useful in bioinstrumentation, pharmaceutics, medical diagnostics and therapeutics applications. Most notably, fibroin has been developed as waveguides (i.e., optical fibers), diffraction gratings, lens arrays, electrical sensors, oxygen sensors, pH sensors, glucose sensors, food sensors, etc [25,34,112,115,123,164,178–180]. Various studies have also demonstrated its immense potential for use as implantable/ingestible optics or sensors [24,114]. In the following, the mechanically demanding roles of silk fibroin as optics and sensors are described.

Mechanical immobilization. Fibroin can achieve mechanical stability with aqueous processing often without the need for chemical crosslinking or UV-curing [18]. As such, optical or sensing probes, especially biological probes (e.g., hemoglobin, myoglobin, enzyme peroxidase, antibody Immunoglobulin G) can easily be incorporated into fibroin via mechanical entrapment [13,34,24,178–180]. The use of biological probes (e.g., antibodies or enzymes) in imaging and sensing applications is often favored over chemical (i.e., nonbiological) probes due to their higher level and broader range of sensitivities and specificities. With the ease of mechanical entrapment, biological probes are easily attached onto biologically produced fibroin without damage, as compared to commonly used materials (e.g., silica, silicon, polydimethylsiloxane or polymethacrylmethacrylate) [180]. For example, antibodies such as normal mouse IgG are mechanically immobilized on the surface of fibroin films, with preserved bioactivities to recognize antigens [13]. Besides, proteins such as haemoglobin are similarly immobilized in fibroin film-based diffraction gratings, with preserved

bioactivities to sense and detect oxygen via spectral absorption change [179].

Processing and handleability. Fibroin can offer good mechanical properties as substrates to impart functional components (e.g., graphene, metallic electrodes, etc.) by direct-writing [158], inkjet printing [24] and transfer printing [103,181], which can produce mechanically robust one-dimensional waveguides [178], two-dimensional films (conformal or free-standing) [94,119,179], or even more complex three-dimensional structures [158,182,183]. The good mechanical properties of fibroin are essential to allow its mechanical processing and handling for optics and sensing applications (e.g., shaping of optics/sensing elements, construction of electrical/light-coupling input faces, surface-smoothing, etc.) [24,184–186].

Tissue contact and device miniaturization. The combined mechanical flexibility and toughness of fibroin (e.g., ultrathin conformal films) render it mechanically compatible with biological tissues to allow intimate integration of sensing elements onto biological tissues, as compared to rigid and bulky traditional systems (e.g., braces, clamps, etc.) [103,181]. For example, fibroin films imprinted with gold electrode arrays are used for high resolution brain signal sensing in vivo, benefited from their ability to flex without fracturing to achieve high degree of instant conformal contact with the brain tissue [103] upon contact with water. Besides, fibroin combines lightweight, strength and toughness even at reduced dimensions (i.e., tens of nanometers), making it particularly attractive for use in miniaturized devices. Miniaturization often introduces new and better functionalities (e.g., better sensitivity, signal and light propagation), overcomes space and size constraints and also promotes cost-effectiveness [187]. Miniaturized devices are also useful in minimally invasive medical diagnostics and treatment applications [188] based on optics and sensing principles.

1.6 Research Motivations and Objectives

Bombyx mori silkworm silk fibroin has demonstrated its incredible features suitable for advanced applications in the fields of textiles, tissue engineering, drug delivery, imaging, and sensing. It is progressively being developed into sensing, tracking, light transmitting, or drug releasing elements of bioelectronics, biophotonics, microfluidics, and also into medical optical fibers for minimally invasive medical diagnostics and treatment applications. Most applications take advantage of fibroin's mechanical properties. In addition to the direct use and the delicate replication of fibroin's natural structure and properties, there is a growing interest to introduce more new functionalities into silk. Emerging applications of silk also often require the use of fibroin in small amount due to current trend towards miniaturized devices to achieve better functionalities, to overcome space and size constraints, and to be cost-effective. For many applications, good mechanical properties of silk fibroin are important for its functionalities, durability, aesthetic values, etc.

In this study, it is hypothesized that by feeding molecules to silkworms which can reach the silk within the gland and interact with the silk protein in the gland, it is able to change the structures of the silk (in terms of the structural content and nanocrystallite dimensions) to achieve better mechanical properties. The purpose of this study is to greatly enhance the mechanical properties of silk fibroin by investigating its structures at the nanoscale combined with *in vivo* uploading of substance into silk to effectuate changes to the structures, based on natural silk production and spinning process. Besides, it is also the purpose of this study to investigate the fate of xenobiotics in a silkworm model and the effect of molecular properties on the biological incorporation of various molecular materials into silk, in order to gain a better understanding to select, design and synthesize appropriate molecules for uptake of substances into silk through a feeding technique. The specific objectives of this thesis are:

1. To explore the structure and mechanical properties of the silk through investigating the mechanical behaviour of β-sheet crystallites.

2. To modulate the structure of silk using a feeding approach with selected substance to achieve greatly enhanced mechanical properties comparable to the spider dragline silk, and to characterize the silk in terms of the structural content and hierarchical structures.

3. To investigate the enhanced mechanical properties of the silk in relation to any structural changes through understanding the interaction of selected substance with silk fibroin.

4. To explore the concentration effect of selected substance on the uptake in silkworms and on the structures/mechanical properties of the silk.

5. To investigate the *in vivo* absorption, distribution and excretion of xenobiotics in a silkworm model after being consumed by silkworm together with the mulberry leave feed, by studying their fate in the silkworm body and their uptake into silk using a series of fluorescent substances as model compounds.

Chapter 2 Structure-Dependent Mechanical Property of Silk

2.1 Introduction

The *Bombyx mori* silk fibroin exhibits a number of superior properties in strength, ductility, biocompatibility, and biodegradability that enable a wide range of applications in apparel/medical textiles, surgical sutures, tissue engineering scaffolds, drug/gene carriers, optical components and sensors [11]. Silk fibroin comprises hydrophobic (i.e., water-hating) β-sheet crystallites (hereafter simply referred to as crystallites) embedded in a hydrophilic (i.e., water loving) amorphous matrix [41,189] that holds moisture, as illustrated in Figure 2.1. The crystallites consist of poly(glycine-alanine) (i.e., poly(Gly-Ala)) peptide chains as the main structural component, with adjacent chains held together by hydrogen bonds in an antiparallel arrangement to form β-sheets [6]. The extensive inter-chain interactions in the highly ordered crystallites contribute to the superior strength of the silk fibroin. The amorphous domain, on the other hand, is mostly disordered and acts as a soft matrix in the silk fibroin [46,57,58,65,67,68,190–193].

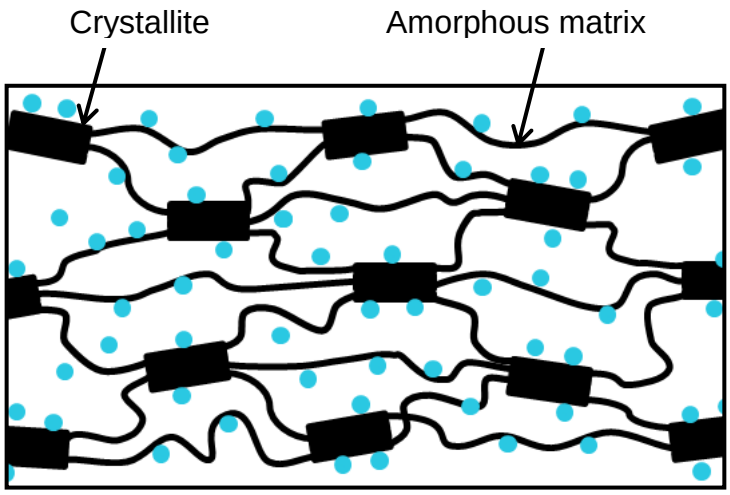

Figure 2.1 Schematic β-sheet crystallites embedded in the amorphous matrix of silk fibroin. Water molecules are represented by blue dots.

There is a great interest in the influence of moisture on the structure and strength of silk fibroin. The mechanical property of silk is known to be influenced unfavourably by humidity, however previous studies showed only the effect of moisture on the amorphous matrix of the silk, or the silk fibroin as a whole [192,194,195]. There is an intriguing question on how do water molecules affect the structure and failure strength of silk crystallites? There has been no systematic experimental or modelling analysis focusing on the effect of moisture on the mechanical behaviour of the crystallite domain. In this study, molecular dynamics simulations were performed on a typical silk crystallite unit in environments with different degrees of hydration to investigate the effect of moisture on its structure and strength. Besides, when silk is subjected to tensile loading, the fracture should be dictated by the weakest rupture strength of the crystallite. An important question naturally follows: what failure process dictates the strength of silk? Accordingly, pull-out tests for a β-chain within a crystallite unit were also performed to assess the chain location-dependent strength, aiming to identify the critical failure process that dictates the breaking strength of silk. Results obtained show that water molecules have the effect of hindering the formation of hydrogen bonds between β-chains in the crystallite domain. Furthermore, the ultimate tensile force (UTF) for pulling out a β-chain from a crystallite unit is strongly chain location-dependent, from which identify the weakest link that dictates the failure process was identified.

2.2 Theoretical Simulations

2.2.1 Models

An antiparallel β-sheet crystallite unit that represents the crystallite domain of *Bombyx mori* silk was selected as a model system for simulations. The initial coordinates for the atomistic model of the crystallites were obtained from Protein Data Bank with the entry of ‘2slk’

and the sequence of poly(Gly-Ala) [46]. Figure 2.2a illustrates the structure of the crystallite unit consisting of four layers of antiparallel β-sheets. Each layer of the crystallite unit consisting of five peptide chains, where Ala residues are displayed in blue and Gly residues in yellow, as shown in inset of Figure 2.2. The end view of the four-layer crystallite, where the targeted β-chains to be pulled out are labelled as surface layer (SL), middle layer (ML), surface layer-middle chain (SLMC), surface layer-corner chain (SLCC) and middle layer-middle chain (MLMC) is also shown. The figures were generated using the visual molecular dynamics (VMD).

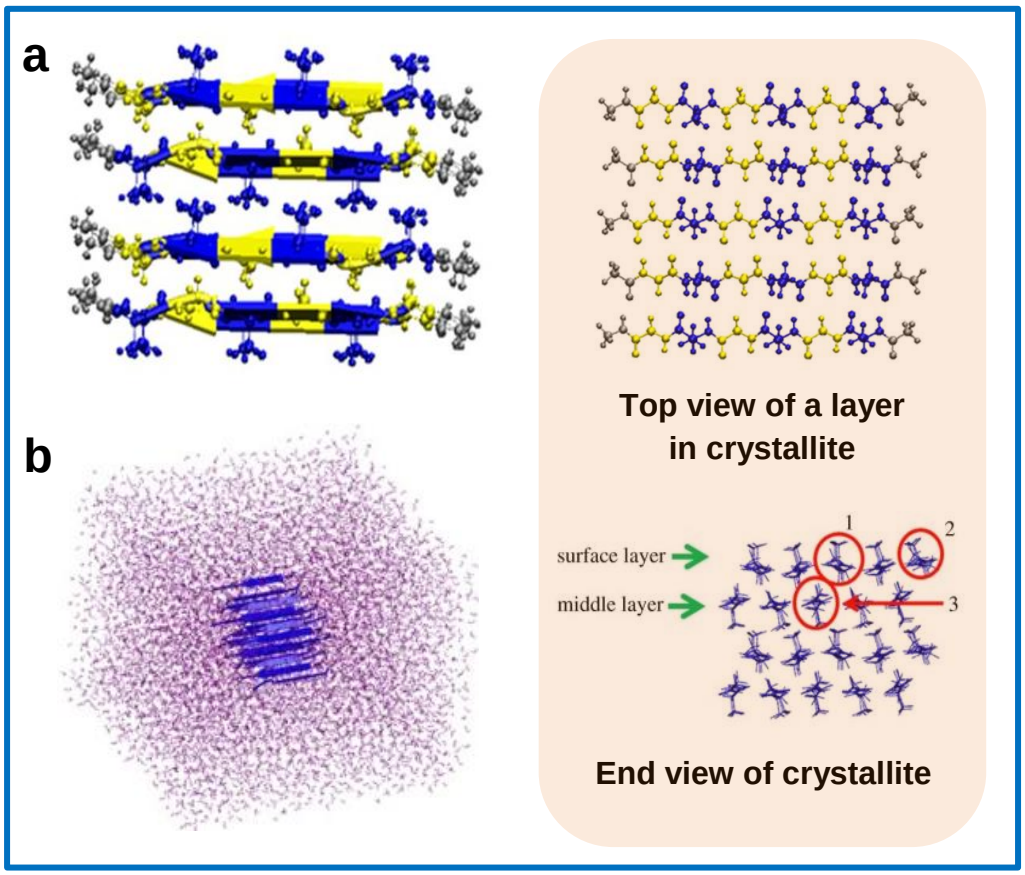

Figure 2.2 Crystallite structure and simulation set-up. (a) Structure of a four-layer silk β-sheet crystallite. Inset: top, top view of one layer of the silk β-sheet crystallite structure, each layer consists of five peptide chains. The residues displayed in blue represent Ala residues while those in yellow represent Gly residues. Cap residues are coloured in grey; bottom, end view of the β-sheet crystallite structure. Surface layer (SL) and middle layer (ML) are labelled, respectively. Representative

chains are highlighted in red circles: (1) SLMC, (2) SLCC and (3) MLMC. (b) β-sheet crystallite structure in the water box.

2.2.2 Simulation methods

The protein was parameterized using Amber force field [196]. To simulate the crystallite structure in a water environment, the crystallite was solvated in a water box [197] (Figure 2.2b). To simulate the crystallite structure in a water-free environment (hereafter simply referred to as vacuum), the crystallite was placed in a box without water molecules. In all cases, energy minimization was first carried out, followed by molecular dynamics simulation for up to 5 ns to obtain the equilibrium configurations. Periodic boundary conditions and a time step of 0.001 ps were adopted. Molecular dynamics simulations were performed at the temperature of T = 300 K and a pressure of P = 1 bar. The box dimensions are 6.0 × 6.5 × 6.8 nm^3. The electrostatic interaction of water solvent is evaluated by the particle mesh Ewald method. All simulations were carried out using Gromacs, and presented in figures using visual molecular dynamics (VMD) [198,199].

Equilibrated structures were adopted as the starting configurations for mechanical tests. Pull-out tests were carried out using steered molecular dynamics simulations [200]. For the targeted chain(s) to be pulled out from the crystallite, the terminal residue(s) were subjected to a force along the chain direction by pulling a spring with a constant velocity. A counter force was applied to the rest of the chains in the crystallite. Specifically, if one layer of the β-chains is pulled away from the crystallite, the pulling force is applied to the end residues of all the chains in this layer, whereas a counter force is applied to the rest of the chains in the crystallite. The pulling rate is 0.5 nm ns^{-1} with a spring constant of 830 pN nm^{-1} [68].

2.3 Results and Discussion

Although water environment has been known to have significant impact on the mechanical properties of the amorphous domain of silk [195], its effect on the crystallite domain remains unexplored. Equilibrium simulation was performed on the crystallite domain in both vacuum and water environment. The root-mean-square deviation (RMSD) of the β-chains is within 2 Å without unreasonable fluctuations.

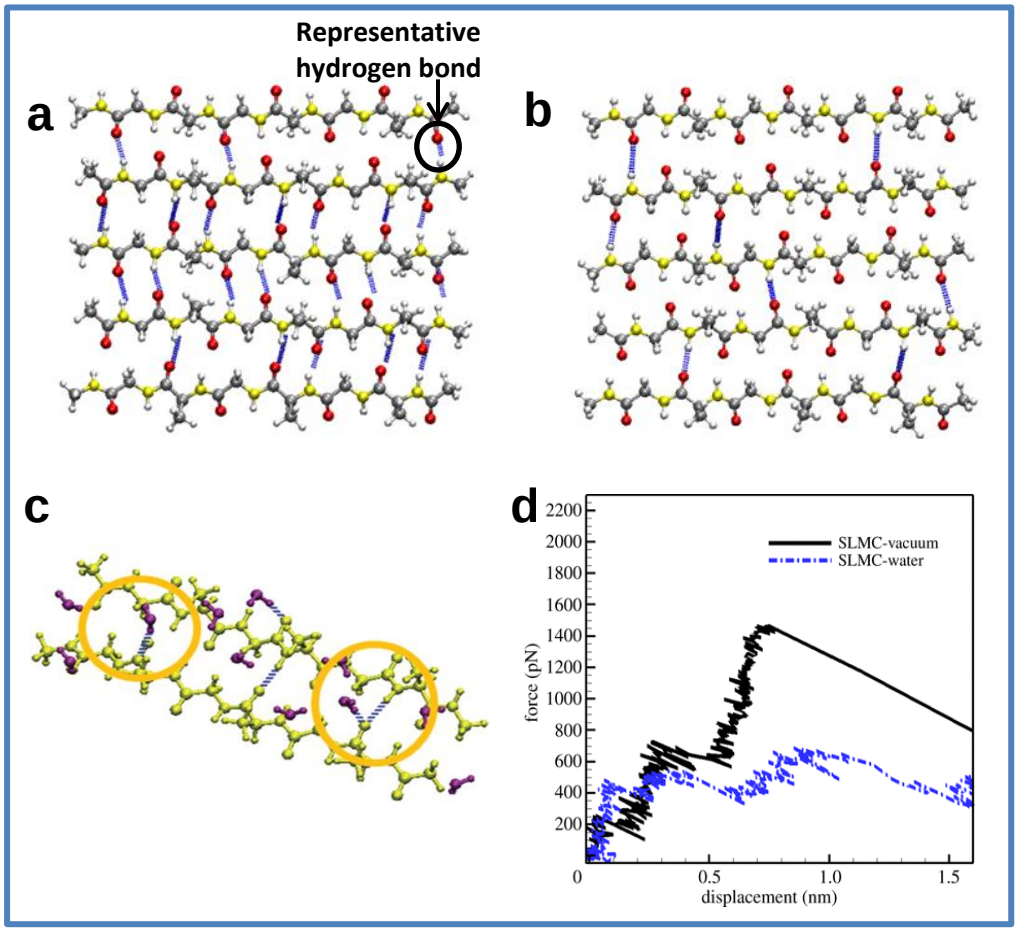

Figure 2.3 Hydrogen bond analyses of the β-sheet crystallite structures. (a) Snapshot of the equilibrated structure in vacuum (i.e., water-free) environment, showing the β-chains on surface layer of the equilibrated crystallite. (b) Snapshot of the equilibrated structure in water environment, showing the β-chains on surface layer of the equilibrated crystallite. The hydrogen bonds between the β-chains are displayed in blue. (c) Snapshot of two representative β-chains on the SL interacting with water molecules. The β-chains are displayed in yellow, water molecules are displayed in purple, and the hydrogen bonds are

displayed in blue. (d) Force–displacement curves for pulling out the SLMC from the crystallite in vacuum and in water environment, respectively.

2.3.1 Water effects on crystallite domain

2.3.1.1 Hydrogen bond analyses

Hydrogen bond formation in β-sheet crystallite provides strength and stability to the crystalline structure. The behaviour of hydrogen bonds in the crystallite was assessed upon exposure to the vacuum and water. Figure 2.3a and 2.3b show the surface layer of the equilibrated crystallites exposed to vacuum and water environment, respectively, displaying hydrogen bonds formed in the structures. The hydrogen bonds were analysed using VMD default definition for hydrogen bonds, i.e., by tracking N–O in the β-sheet layer. It was determined that in the β-sheet layer, there are 22 hydrogen bonds in vacuum, as compared with eight in water. To assess the stability of hydrogen bonds [201,202] in vacuum and in water, the lifetimes of hydrogen bonds were obtained from long time molecular dynamics simulations of each system up to 50 ns [203]. The hydrogen bond lifetimes in water are consistently lower in water than in vacuum. The lifetime of hydrogen bond in the surface layer is 212.52 ± 13.40 ps in vacuum, and drops to 43.36 ± 2.84 ps in water. Likewise, the lifetime of hydrogen bond in the middle layer is 286.16 ± 28.47 ps in vacuum, and drops to 58.56 ± 9.37 ps in water. Both the number and stability of hydrogen bonds in the crystallite are lower in water, as compared with in vacuum. Figure 2.3c shows the interaction configurations of two β-chains in crystallites interacting with water molecules on the surface layer.

To simulate conditions with different degrees of hydration, in addition to vacuum (water-free) and the fully-hydrated system (100%), it was also taken into consideration two intermediate systems containing 10% and 50% of the number of water molecules used for the fully-hydrated

environment. The activation energy of the hydrogen bond is able to reflect the strength of hydrogen bond [204], with higher activation energy corresponding to higher bond strength. The activation energies of the hydrogen bond were compared among these systems. The activation energy of a representative hydrogen bond in the crystallite, as highlighted in Figure 2.3a, was obtained by calculating the mean first passage time τ_{mfp} [204]. Molecular dynamics simulation was carried out for each system at 300 and 350 K for 1 ns, respectively, and the activation energy barrier is calculated via $1/\tau_{mfp} = A \exp(-(E_a/k_B T))$, where A is the attempting frequency, and E_a is the activation energy. The hydrogen bond activation energy in vacuum is 2.86 kcal mol^{-1}, while the value reduces to 1.02 kcal mol^{-1}, in water. As tabulated in Table 2.1, the hydrogen bond activation energies in systems with 10 and 50% degree of hydration take intermediate values. The higher the water content, the weaker is the hydrogen bond. Overall, hydrogen bond analyses suggest that the interactions between β-chains and water molecules compete with the inter-chain hydrogen bond interaction (Figure 2.3c), and thus water molecules have a weakening effect on hydrogen bond formation in the crystallite.

Table 2.1 Hydrogen bond energy for the representative hydrogen bond in the crystallite in environment with different degree of hydration. *A* denotes the attempting frequency, and E_a denotes the activation energy.

Degree of hydration	***A*** **(ps^{-1})**	**E_a (kcal/mol)**
Vacuum	24.34	2.86
10% water	16.47	2.58
50% water	9.23	2.21
Full water	5.84	1.02

2.3.1.2 Crystallite strength and stability

To prove that water molecules weaken the strength and stability of the silk β-sheet crystallites, pull-out tests were carried out on the targeted β-chain from the crystallite in vacuum and in water. The pull-out of the middle chain in the surface layer (SLMC) is selected as the representative case for comparison. For each system, the UTF is defined as the peak rupture force when the targeted β-chain is pulled away from the crystallite. The force-displacement curves for the pull-out tests in the two environments are shown in Figure 2.3d. It is seen that the UTF in water is much lower than that in vacuum.

Table 2.2 Specific interaction energies between selected β-chain(s) and the rest of the chains in the crystallite unit.

Targeted Chain(s)	Interaction energy per length (kJ/(mol nm))	
	In vacuum	In water
SLMC	-244.50	-231.56
SLCC	-125.32	-92.47
MLMC	-283.26	-275.43
SL	-417.74	-367.55
ML	-582.94	-543.98

To further understand the strength and stability of the crystallite in water, the specific interaction energy was also computed, of which is defined as the interaction energy between the targeted β-chain(s) and the rest of the crystallite divided by the length of the peptide. The specific interaction energies are calculated based on the equilibrium structure of the crystallite, and consist of both electrostatic interaction energy and van der Waals energy. The specific interaction energy for each of the targeted β-chain(s) in crystallite in vacuum and water environment, respectively, is tabulated in Table 2.2. It is seen that for

all the cases (i.e., β-chain(s) in different locations in the crystallite), the specific interaction energy is weaker in water than that in vacuum, confirming that the crystallite structure is less stable in water.

Overall, these simulations demonstrated the weakening effect of water molecules on the crystallite. Along with the reduction in the number, lifetime, and strength of hydrogen bond in water, the specific interaction energy of β-chain(s) in the crystallite also decreases in water as compared with in vacuum. These consequently imposed a weakening effect on the crystallite in water environment.

2.3.2 Water effects on the whole silk fibroin

Silk fibroin molecule is a heterogeneous, multiblock co-polymer with backbones containing alternating hydrophilic and hydrophobic amino acid sequences [4]. Structurally, silk fibroin is composed of β-sheet crystallites that are embedded in a matrix of amorphous domain (Figure 2.1). The fibroin molecule has a more extended chain structure at the initial production stage. Upon *in vivo* processing, the hydrophobic blocks begin to assemble and organize to form β-sheets. Meanwhile, the hydrophilic blocks promote silk solubility in water and also have the function of preventing premature aggregation of β-sheets during *in vivo* assembly. The β-sheet crystallites are eventually formed upon spinning. With the presence of the hydrophilic blocks, silk fibroin not only retains water even after spinning and drying in air, but also easily absorbs water from the environment [205].

Water has been reported to play an important role in the mechanical properties of silk. Dehydration has been cited to be a major cause of brittleness, rigidity and decreased softness in silk (e.g., excavated silk) [206,207]. Considering silk fibroin as a whole, water influences not only the amorphous domain, but also the crystallite domain as demonstrated in this study by molecular dynamics simulations. On the one hand, water plays the role as a plasticizer [207], which helps to

enhance chain mobility in the amorphous domain of silk, in this way it increases the flexibility and plasticity, and thus reduces the brittleness of the silk fibroin. Hence, dehydrated silk, which lacks water as plasticizers in the amorphous region, will be brittle, and water is thus beneficial in the amorphous region. On the other hand, concerning the β-sheet crystallite, which mainly dictates the strength of silk, it has been demonstrated in this study via molecular dynamics simulations that water weakens the strength of the β-sheet crystallite. The strength of crystallite, given by the hydrogen bonds between β-sheet layers, was affected by moisturization, with four cases investigated: the crystallite fully-hydrated in (i) 100% water (ii) 50% water (iii) 10% water and (iv) vacuum box, as shown in Table 2.1. The vacuum state reflects the extreme case when the silk fibroin is fully-dehydrated (e.g., excavated silk). Comparing these different solvation states demonstrates that water has a weakening effect on the mechanical property of silk. These findings provide useful insights to potentially tune the mechanical property of silk, for example by feeding suitable molecules to the silkworms to control the water content in the produced silk.

2.3.3 Single chain pull-out

To identify the critical process that governs the failure strength of β-sheet crystallite in silk, pull-out simulations were performed. First of all, , single chain pull-out (i.e., pull-out of one β-chain) from crystallite is investigated, i.e., SLMC, MLMC and SLCC pull-out. The pull-out simulations are carried out in water box since experimental tests on silk fiber were typically carried out in moisture-containing environments [4]. The representative snapshots during the single chain pull-out tests are shown in Figure 2.4a.

The force-displacement curves for pulling out a single chain from the three different locations in the crystallite are shown in Figure 2.5. The UTF for pulling out the MLMC is 1613.52 pN, which is the highest

among the three cases; the UTF for SLMC is weaker, which is 691.90 pN; and that of the SLCC is the weakest, with the value of 557.11 pN. It is noted that the UTF for MLMC obtained by previous molecular dynamics simulation [58] is about 1500–2300 pN for crystallites with sizes of approximately 6.56–1.87 nm, in good agreement with the present value of MLMC (1613.52 pN).

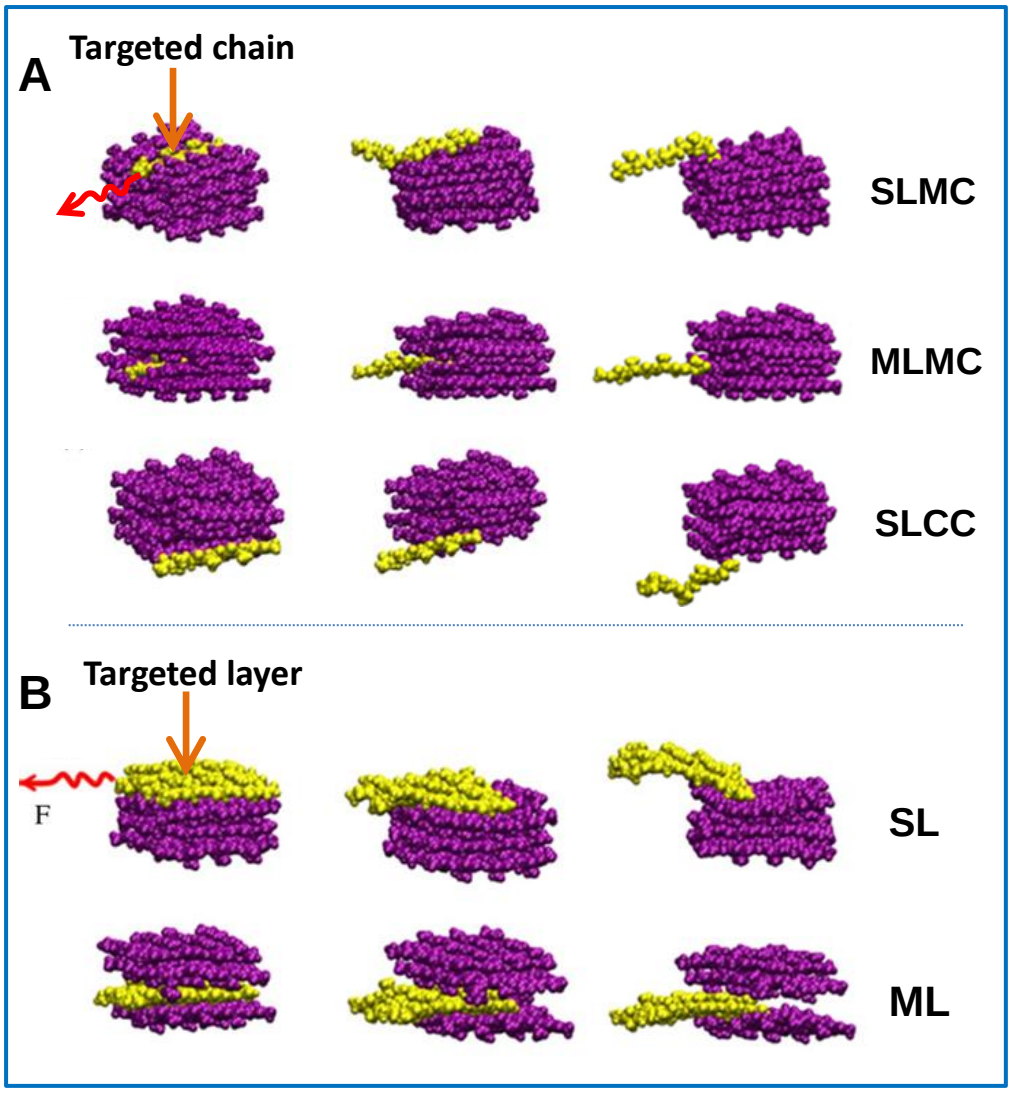

Figure 2.4 Representative snapshots for pulling out the β-chain(s) from different locations of the crystallite unit. (a) SLMC, MLMC and SLCC. (b) SL and ML. The chain(s) being pulled out are displayed in yellow, while the rest are displayed in purple.

On the other hand, the UTF for SLCC is only one-third that for MLMC due to much less confinement by inter-chain hydrogen bonds, and after

the initial rupture during the pull-out process, the interaction between this chain and the rest of the crystallite is too weak so that no obvious re-bonding process is observed. Representative snapshots for pulling out SLCC from the crystallite unit are also shown in Figure 2.5. From Table 2.2, it is seen that the specific interaction energy between MLMC and the rest of the crystallite in the water environment is the strongest (i.e., −275.43 kJ/(mol nm)), as compared with that between SLCC and the rest of the crystallite in the water environment, which is the weakest (i.e., -92.47 kJ/(mol nm)).

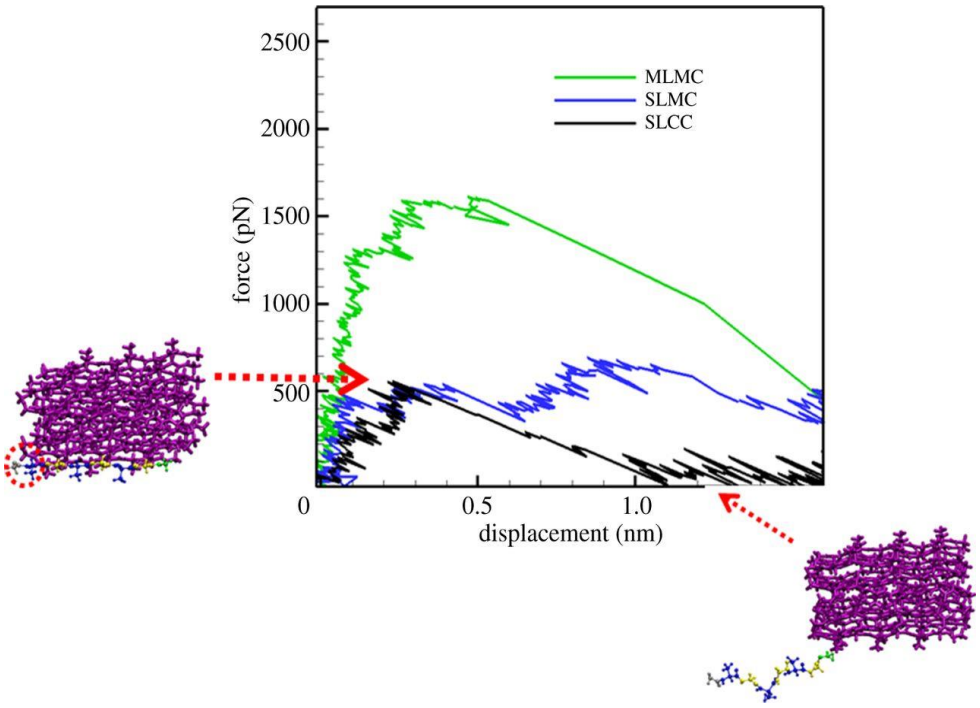

Figure 2.5 Force-displacement curves for pulling out one single chain from three different locations of the crystallite unit. Snapshots for pulling out the SLCC are also shown. The β-chain with residues displayed in blue and yellow is the targeted peptide chain, while the rest are displayed in purple.

2.3.4 Middle layer versus surface layer pull-out

Then, whole layer pull-out (i.e., pull-out of one layer of β-chains) from crystallite is investigated, i.e., SL vs. ML pull-out. The representative

snapshots during the pull-out tests are shown in Figure 2.4b. The force-displacement curves for pulling-out SL and ML are shown respectively in Figure 2.6. The UTF for pulling out pulling out ML is 2550.03 pN, and the configuration of the crystallite corresponding to UTF is given in the inset of Figure 2.6. Right after the peak force, the bonds between the pulled layer and its two adjacent layers are broken, leading to the ultimate failure of the crystallite. The subsequent abrupt decrease in force indicates the brittle nature of the ML failure. As for the pull-out of the SL, the first peak in the force-displacement curve corresponds to the initial rupture (see the inset of Figure 2.6), subsequently during the sliding of the β-chains out of the crystallite, bonds are able to reform between the layer being pulled-out and its adjacent layer. The configuration of the crystallite corresponding to the second peak is also shown in the inset of Figure 2.6. Compared to the ML, the UTF for pulling out the SL is much lower, i.e., 708.88 pN, occurring at the second peak.

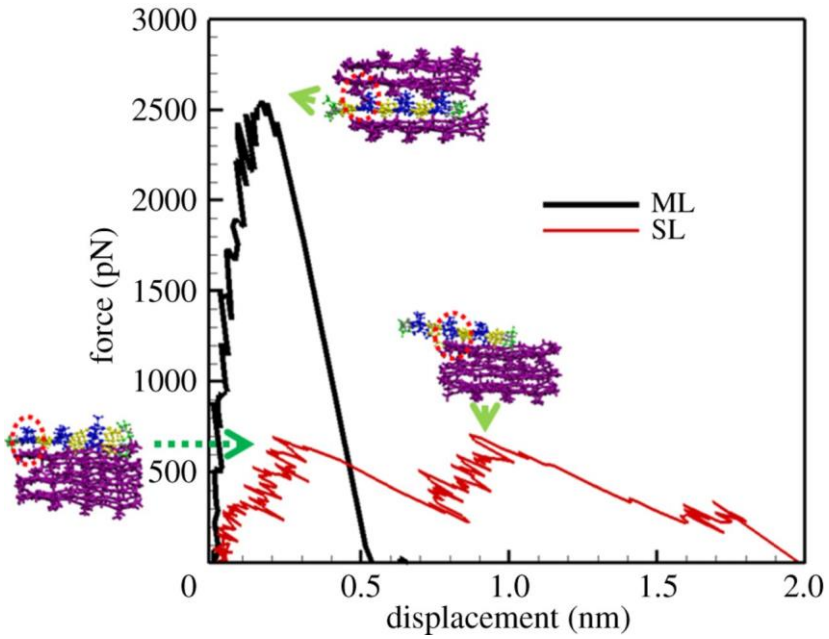

Figure 2.6 Force-displacement curves for pulling out the ML and the SL, respectively. Snapshots of the crystallite unit corresponding to the rupture force at peaks are also provided. Residues of the peptides in the targeted layer are displayed in blue and yellow, while the rest are displayed in purple.

As listed in Table 2.2, in water, the specific interaction energy between the ML and the rest of the crystallite unit is −543.98 kJ/(mol nm), while the SL has a weaker specific interaction energy of −367.55 kJ/(mol nm) with the crystallite unit. The higher energy barrier explains the larger UTF needed to pull-out the ML from the crystallite unit, when compared with SL pull-out. In addition, the difference in the specific interaction energies (ML vs. SL) is greater in the water environment (176.43 kJ/(mol nm)) than in vacuum (165.2 kJ/(mol nm)). This is because from the molecular structure point of view, the ML is less accessible to water molecules, and resultantly the hydrogen bonds formed between the ML and neighbouring layers are less affected by the water molecules. However, owing to the re-bonding process, the resilience of the SL is comparable to that of the ML, despite its much lower UTF than the ML. Therefore within one crystallite unit, the ML shows more brittle behaviour while the SL exhibits more ductile behaviour.

Considering silk fibroin as a whole, the amorphous regions will unravel first during tensile loading, and the load will then be passed on to the β-sheet crystallites [64,72], which are linked to the amorphous regions via surface/interior β-chains. Thereafter, tensile fracture most probably happens in the surface of crystallite domains, since our findings show that rupture force of β-chains on the surface of the crystallites is much weaker than the interior ones. Based on the present structural and energetic analyses, it is concluded that when the silk fibre is subjected to tensile loading, the fracture should start from the pulling of the corner chain in the silk fibroin, which is the weakest link that dictates the failure strength.

2.4 Summary

In summary, the mechanical response of a β-sheet crystallite unit subjected to pull-out tests was investigated via molecular dynamics simulations. It is found that water molecules play a weakening role in

the formation of hydrogen bonds between β-chains, thus decreasing the stability of the β-sheet crystallite compared with that in vacuum. The rupture force for pulling out the β-chain(s) from the crystallite unit varies with the location of the chain(s) in the crystallite unit. This work shows that the pulling of the SLCC has the lowest UTF. Hence, it is the weakest link that controls the failure strength of silk fibre, clarifying the inconsistency between experimental and theoretical failure strengths of silk fibre.

Chapter 3 Intrinsically Toughest Silk

3.1 Introduction

Nature produces silk fibers with impressive mechanical properties surpassing those of many other natural and synthetic materials. As biologically produced protein materials, the silk fibers are obtained from arthropods including spiders (*Araneus diadematus*, *Nephila clavipes*, etc) and silkworms (*Bombyx mori*, etc.) [1,53,55,56]. *Bombyx mori* silkworms are the main producer of silk worldwide. The silk is a highly prized material of immense commercial value. The surface coating sericin is typically removed to reveal fibroin as the main structural component of silk. Particularly well-known for its lustrous appearance, soft-to-touch texture and excellent mechanical properties, the *Bombyx mori* silk fibroin (hereafter also referred to as silk) is conventionally used as textiles and surgical sutures. Current advances have also demonstrated its superior biocompatibility, facile processability, controllable biodegradability, tunable optical properties, and ease of functionalization in native or regenerated morphologies. These qualities render the silk extremely useful in a range of medical and engineering applications, including drug delivery, tissue engineering, sensing, and imaging [14,19–25,188]. Notably, many applications of silk take advantage of its impressive mechanical properties, which by nature surpass many natural and synthetic materials.

The mechanical strength and toughness of silk depend not only on its molecular structure but also on its hierarchical architecture. Upon spinning by the silkworm, the silk dope produced in the silk gland is transformed into a solidified semi-crystalline fibrous network consisting of β-sheet crystallites embedded in a less ordered amorphous matrix. Interestingly, both the silkworm silk and spider dragline silk (e.g., *Nephila* or *Araneus* spider dragline silk) share similar hierarchical architecture but possess great disparity in their mechanical properties

[56,58,64–67,208]. Inspired by spider dragline silk with much superior strength and toughness [55,56,74,75,209], there is an ever growing interest to enhance the mechanical properties of *Bombyx mori* silk.

Several approaches were reported to produce mechanically enhanced silk. Firstly, it was shown that one is able to enhance the mechanical properties of the silk through changing the silk spinning condition [54,73]. Specifically, by way of force-spinning (i.e., artificially drawing the silk from silkworms at controlled speeds) [54] or modulated-spinning (i.e., allowing the silkworm to spin in an electric field) [73], stronger and tougher silk fibers were obtained. The application of those external forces was reported to result in more aligned crystallites along the fiber axis to better support the load, thus rendering the silk fibers stronger and tougher [54,73,77]. Secondly, it was shown that one can obtain mechanically enhanced silk by transfecting gene sequence of spider silk into silkworm for its co-expression with the silkworm silk. Successful gene transfection relies greatly on environmental and genetic factors, and incorporation of the spider silk proteins into the silkworm silk requires that their expression occurs in spatial and temporal proximity to the endogenous silk proteins, which makes it challenging to attain the desired phenotypic expression [85,86]. Considering that silkworms are easily domesticated, and that they produce silk in extremely large scale worldwide at about 70,000 tons per year [83], it makes great economic sense to make direct use of the silkworm silk *in vivo* production and processing system to produce mechanically tough fibers for use in various fields of applications. Following this, a couple of interesting questions naturally arise: Can feeding approach, a green and cost-effective method, be adopted to enhance the mechanical properties of *Bombyx mori* silkworm silk? If yes, then what are the underlying mechanisms? Clearly, answers to these questions are able to provide a novel route to control the structure and the resulting mechanical properties of silkworm silk for its much wider use.

To greatly enhance the mechanical properties of silkworm silk, a facile feeding approach proposed here is to employ a substance that is capable of both entering the silk gland and modulating the structure of the silk. Experimentally, citric acid (CA) molecules were mixed into mulberry leaf at 0.05 wt% to make modified feed (i.e., CA feed), as compared to a typical mulberry leaf feed without added CA molecules (i.e., normal feed). Remarkably, CA silk fibroin (hereafter also simply referred to as CA silk) with significantly enhanced mechanical properties was successfully obtained, which exhibits mechanical toughness nearly double that of control silk fibroin (hereafter also simply referred to as control silk) and comparable to that of spider dragline silk. Both advanced characterizations and computational simulations are used to reveal the underlying interactions of CA with fibroin structures and the structural changes that lead to the great enhancement in mechanical properties. Experimental findings show that the CA silk features remarkably short crystallites which rendered the silk mechanically strong and tough.

3.2 Materials and Methods

3.2.1 Materials

Domesticated silkworms (*Bombyx mori*) were obtained from Carolina Biological Supply Company, USA. Mulberry leaf powder was obtained from Recorp Inc., Canada, and citric acid (CA) anhydrous was obtained from Fisher Scientific.

3.2.2 Experimental methods

3.2.2.1 Silkworm culturing, feed preparation and silk degumming

Normal feed was prepared by microwaving mulberry leaf powder (100 g) with water (300 mL). Modified feed was prepared by microwaving mulberry leaf powder (100 g) with water (300 mL) followed by mixing

CA (50 mg) at 0.05 wt%. Other weight percentages were also prepared in the same way. Domesticated silkworms were cultured on the normal feed throughout the larval stage up to the second day of the fifth instar. Starting from the third day of fifth instar, silkworms were transitioned to the modified feeds to produce CA silk while the control silk was obtained from silkworms continued on the normal feed. The silkworms were continuously fed until they started spinning.

3.2.2.2 Tensile testing of silk

Silk fibers were individually mounted onto paper frames with a 20 x 5 mm window for tensile testing. The paper frame was fixed to the grips and then cut, so that the load during testing was exerted directly on the fiber. The fibers were loaded on a universal tester (Instron Double Column Universal Tester 5569 with a 5 N load cell) at a strain rate of 2 mm min^{-1}. The gauge length of each tensile sample was individually determined from the distance between the two grips at the starting position using the Bluehill software on a computer connected to the tester. Slack correction was also performed to remove 'toe' region of the stress-strain curves. For each sample, a 10 mm-segment was mounted on a specimen holder using carbon tape, sputter-coated with gold under vacuum, and imaged under a scanning electron microscope (SEM) (JEOL LV SEM 6360LA) to determine the fiber cross-sectional area for tensile stress calculation. The smallest diameter along each fiber was adopted, from which the cross-sectional area of the fibroin fiber was derived. Mechanical data presented as average ± standard deviation. Statistical significance performed using one-way ANOVA (*p<0.01, **p<0.005; n=5).

3.2.2.3 Structural characterization of silk

To remove the sericin, the silk fibers was added into a degumming solution (10 mL) consisting of Savinase enzyme (10 mg, Novozymes, Denmark) and Triton-X (10 mg) in 1 gL^{-1} $NaHCO_3$ solution, followed by

heating at 55 °C for 1 h. The degummed silk was then collected, rinsed with water, and dried in air for two days before further characterization. For determination of crystallite dimensions, parallel bundle of the degummed fibers were mounted on a cardboard frame and the X-ray diffraction (XRD) patterns were collected on an XRD system (Bruker D8 General Area Detector Diffraction System) using a beam size of 0.5 mm and a radiation wavelength of 1.5418 Å (CuKα). The sample-to-detector distance was 5 cm and the exposure time was 20 min. Radial integration was carried out on the obtained XRD patterns along both the equatorial (5–40°) and meridian (5–37.5°) axes. The resultant spectra were fitted into component peaks characteristic of silk fibroin. Crystallite sizes along **a**, **b** and **c** directions were determined respectively from the (200) and (120) crystalline peaks from the equatorial spectra, and (002) crystalline peak from the meridian spectra using Scherrer's formula, $L = 0.9\lambda/(\text{FWHM} \times \cos\theta)$, where L = crystallite size along **a**, **b** or **c** direction, 0.9 = Scherrer's constant, λ = wavelength of incident x-ray (1.5418 Å for Cu Kα radiation), θ = peak position, and FWHM = full-width at half-maximum. Scherrer's formula provides a lower bound to the crystallite size. Specifically, **a** is the direction along the stacking of β-sheets, **b** is the direction in a β-sheet perpendicular to the chain axis, and **c** is the direction along the chain axis.

For determination of structural contents, the degummed fibers were cut into short strands (~2 mm in length) that were mixed with KBr and compressed into disk before testing on a Fourier transform infrared (FTIR) spectrometer (Perkin Elmer FTIR Spectrum 2000). The infrared spectra were collected for each sample (n=3) at a resolution of 4 cm^{-1}. Sixteen scans were performed for each sample to increase the signal-to-noise ratio by a factor of four. After baseline correction, second derivative analysis was performed to 1600–1710 cm^{-1} of the FTIR spectra (the Amide I region) to identify the structural component peak positions of the silk, the structural contents in the silk were quantified through the area analysis of the structural component peaks fitted in

the region of the baseline-corrected FTIR spectra. The percentage of each structure was determined by calculating the area percentage under the respective component peaks with respect to the total area under the spectra. Data presented as average ± standard deviation. Statistical significance performed using ANOVA single factor analysis of variance (*p<0.10; **p<0. 05; n=3).

3.2.2.4 Extraction of silk dope and haemolymph

Haemolymph was extracted from silkworms (n=3) prior to silk spinning using a needle syringe. The pH of the haemolymph was measured using a micro combination pH electrode (Lazar Research Laboratories, model PHR-146, USA). The data were presented as average ± standard deviation. To obtain silk fibroin dopes, the silkworms (n=3) were dissected in Insect Ringer solution containing 128 mM NaCl, 1.8 mM $CaCl_2$. $2H_2O$, 1.3 mM KCl and 50 mM Tris. Silk glands were removed from the dissected silkworms, washed with distilled water, and peeled off their gland epithelial layers to obtain silk dope. The silk dopes were degummed to remove the sericin. The obtained fibroin dopes (n=3) were allowed to dry in air and 3 mg of each dried fibroin dope were then individually dissolved in 100 μL of 9.3 M LiBr solution at 70 °C for 3 h to quantify the content of CA.

3.2.2.5 Quantification of CA

The silk dope or fibers (3 mg) were dissolved by heating in 100 μL of 9.3 M LiBr solution at 70°C for 3h. Upon dissolution of the silk, CA molecules were released and the obtained solution was analyzed to quantify the amount of CA based on a spectrophotometric method. To determine the amount of CA in the silk, dope or haemolymph (n=3), the solution samples (100 μL) were added to a mixture of 4 mL of $Fe(NO_3)_3$ solution and 1 mL of HNO_3, and topped up to 25 mL in a glass vial using distilled water. The CA reacted with Fe^{3+} at a ratio of 1:1 to form

ferric-citrate complex. Next, the solution was illuminated at 1000 W/m^2 (Newport Corporation USA, solar simulator, model 66901) for 10 min to allow the ferric-citrate complex to turn into violet complex via photochromism, and then allowed to rest in shade for 30 min at 4°C to stabilize the color development. Thereafter, the absorbance of the solution at 520 nm was measured using a UV-Vis spectrophotometer. The actual amounts of CA were then calculated by reading off the calibration curve prepared using the same measurement parameters. The data were presented as average ± standard deviation.

3.2.3 Theoretical simulations

3.2.3.1 Molecular structure of CA

The molecular structure of CA was constructed using Material Studio 7.0 (Accelrys Inc., San Diego, CA) and the charge on CA was calculated using the Antechamber module in the Amber 9 software [210]. Energy minimization was conducted on the structure of CA to equilibrate the structure.

3.2.3.2 Molecular dynamics simulation of the interaction of CA and fibroin molecules

All the molecular dynamics simulations were carried out using Gromacs [211] and presented in figures using visual molecular dynamics (VMD) code [212]. For simulating the interactions of CA with fibroin molecules, two fibroin molecules in extended configuration were arranged in an antiparallel manner with an initial distance of 5 Å between them as the initial structure. Each molecule comprises a crystalline sequence intercalated between two amorphous sequences as given below. Molecular dynamics simulation was first carried out on the extended structure of the two fibroin molecules in an implicit water box for 50 ns. Afterwards the obtained configuration was solvated in an explicit water box, and 20 ns of molecular dynamics simulation was carried out to obtain their equilibrated structure (control). In comparison,

the same configuration was first surrounded by 144 CA molecules and then solvated in an explicit water box followed by 20 ns of molecular dynamics simulation to obtain their equilibrated structure. The dimension of the water box was 8.6×7.0×13.5 nm^3. The sequences of fibroin chain are adopted in the above simulations: (i) crystalline sequence: GAGAGSGAGAGAGSGAGAGSGAGAGSGAGAGSGAGS GAGAGSGAGAGSGAGAGYGAGAGSGAAS, (ii) amorphous sequence: GAGAGAGAGAGTGSSGFGPYVAHGGYSGYEYAWSSES DFGTGS. The sequences are respectively adopted from the GX 6.5 and Linker 6 of *Bombyx mori* silk fibroin as published by Zhou *et al* [213].

3.2.3.3 Molecular dynamics simulation of the interaction of CA and fibroin crystallites

A poly(GA) crystallite with two-layer β-sheets was extracted from Protein Data Bank with the entry of "2slk" [46]. Each layer consists of five β-chains. Each β-chain comprises of six residues (three repeating GA sequences) and the chain is acetylated at one end and methylated at the other end, i.e., two cap residues. Molecular dynamics simulation was first carried out on the structure of crystallite in an explicit water box for 5 ns. The equlibrated structure of crystallite was used for the calculation of the binding energy with CA and each of its ionized forms by energetic analysis after energy minimization The dimension of the water box was 3.0×3.8×6.5 nm^3.

For simulating the interaction when the CA is in the crystalline domains, eight CA molecules were located in between the two poly(GA) crystallites. The G (glycine) residues are displayed in yellow, the A (alanine) residues are displayed in blue, the cap residues are displayed in grey, and the CA molecules are displayed in green. The system was solvated in an explicit water box and the simulation was carried out for 5 ns. The dimension of the water box was 6.3×6.4×6.6 nm^3.

3.3 Results and Discussion

3.3.1 Enhanced mechanical properties and structural changes in CA silk fibroin

Figure 3.1a shows the stress-strain curves of silk fibroin produced with CA feed (i.e., CA silk), compared with silk fibroin produced with normal feed (i.e., control silk), along with the fracture surfaces. The mechanical properties of CA silk are found to be significantly enhanced, being much stronger and more ductile than control silk. The mechanical properties are tabulated in Table 3.1. Remarkably, the CA silk obtained exhibits significantly higher ultimate tensile strength of 840 ± 39 MPa, along with significantly higher toughness (i.e., energy to failure) of 225 ± 14 MJ/m^3 that almost double those of the control silk.

The CA silk has significantly higher breaking strain at 38 ± 2 %, compared with 32 ± 2 % of the control silk. It is additionally noted that the toughness exceed those of spider dragline silk fibers (i.e., 160–200 MJ/m^3) [53–55,59,214]. With the greatly enhanced strength and ductility, the silk obtained in this study emerges to be the intrinsically toughest silkworm silk, with mechanical properties that far exceed those of the previously reported silkworm silk (including the enhanced force-spun, modulated-spun and genetically-modified silkworm silk), and compare well with those of naturally produced spider silk (including those from spider species such as *Araneus diadematus*, *Nephila clavipes*, etc.) [53,55,56,54,73]. Figure 3.1b and Figure 3.1c show the fracture surface of CA silk and control silk respectively.

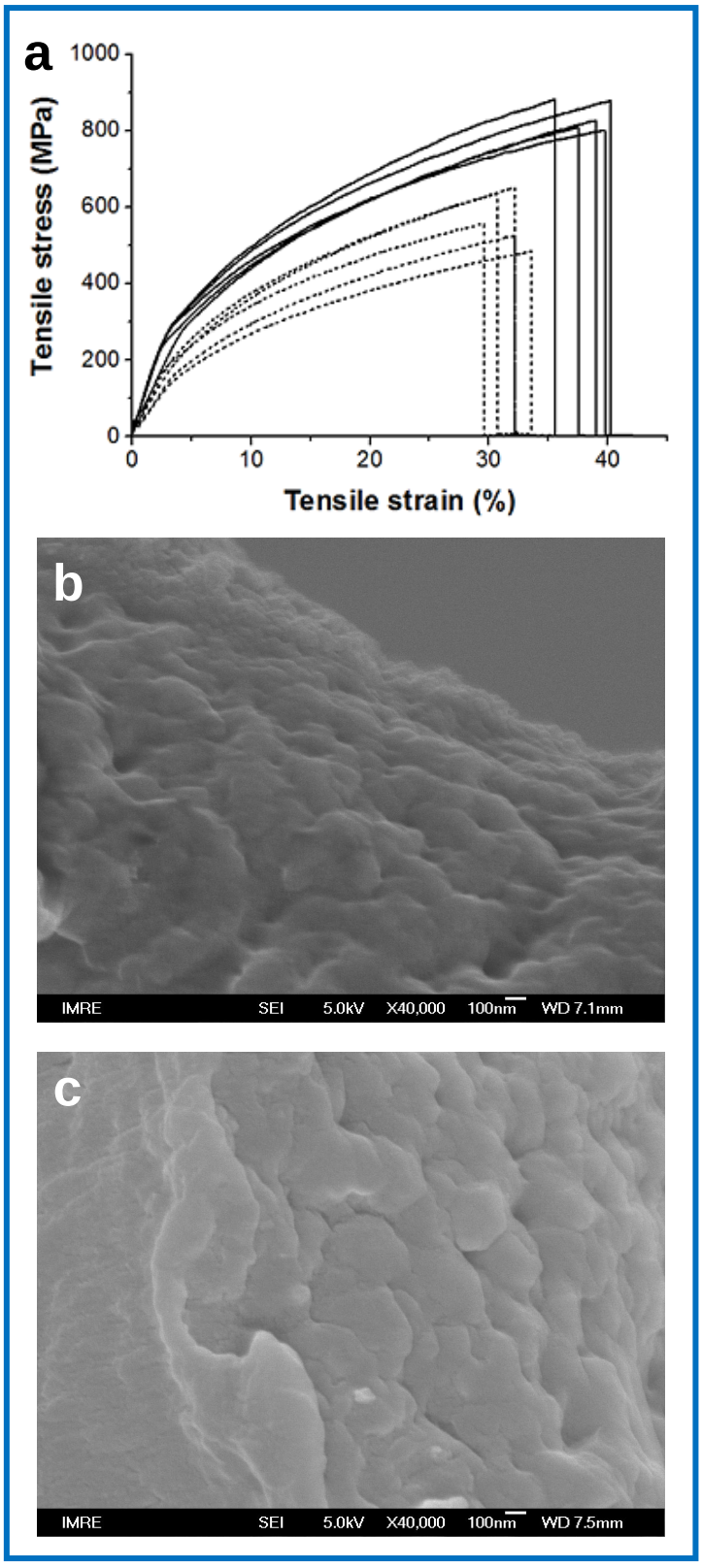

Figure 3.1 Stress-strain curves and fracture surfaces of CA silk vs. control silk fibroin. (a) Stress-strain curves of CA silk vs. control silk. Fracture surfaces of (b) CA silk and (c) control silk, respectively at 40,000x magnification (scale bars: 100 nm).

Table 3.1 Tensile properties of CA silk vs. control silk (*p<0.01, **p<0.005; n=5).

	Control silk	CA silk
Young's modulus (GPa)	5.93 ± 1.42	9.57 ± 1.70*
UTS (MPa)	571.56 ± 71.12	840.38 ± 38.67**
Breaking strain (%)	31.82 ± 1.88	38.38 ± 1.89**
Yield strength at 0.1% offset (MPa)	145.01 ± 20.70	221.77 ± 26.04**
Yield strain (%)	2.78 ± 0.66	2.46 ± 0.76
Toughness (MJ/m^3)	120.74 ± 12.98	224.52 ± 14.31**

Silk has a hierarchical architecture that is built from structures including the β-sheets, helices, turns and random coils (Figure 3.2a) [58,64,68,69]. The mechanical properties of silk are greatly dependent on its hierarchical structures. The CA silk and control silk were examined both using Fourier transform infrared (FTIR) spectroscopy and X-ray diffraction (XRD). Remarkable changes in the structures of the CA silk as compared to the control silk were detected by FTIR (a commonly used technique to quantify the structural contents in proteins including the silk [215–217]) through area analysis of the structural component peaks. The structural component peak positions of the silk were identified by performing second derivative analysis (Figure 3.3) in 1600–1710 cm^{-1} region of the FTIR spectra (Figure 3.4). FTIR findings indicated a significantly reduced content of β-sheets in CA silk (20.7 ± 1.1%) (Figure 3.2b).

As detected by XRD (a commonly used technique to quantify the crystallite sizes in the silk [56,67,72]), the CA silk features remarkably short crystallites of 4.38 nm. The control silk, on the other hand, features lengthy crystallites at 8.99 nm that are comparable to those typically observed in the silkworm silk (e.g., 10.30 nm [56]). Figure 3.5a

illustrates a β-sheet crystallite in three dimensions. The dimensions along the **a**, **b** and **c** directions correspond to the thickness, width and length of the crystallite respectively. The crystallite sizes along each direction were determined from the full width at half maximum (FWHM) of the crystalline peaks, (i.e., (200), (120), and (002), Figure 3.5b) fitted for the XRD patterns (Figure 3.6). Apart from the remarkably reduced crystallite length in CA silk, no remarkable changes were detected in the width and thickness of the crystallites of CA silk, as compared to the control silk (Figure 3.5c).

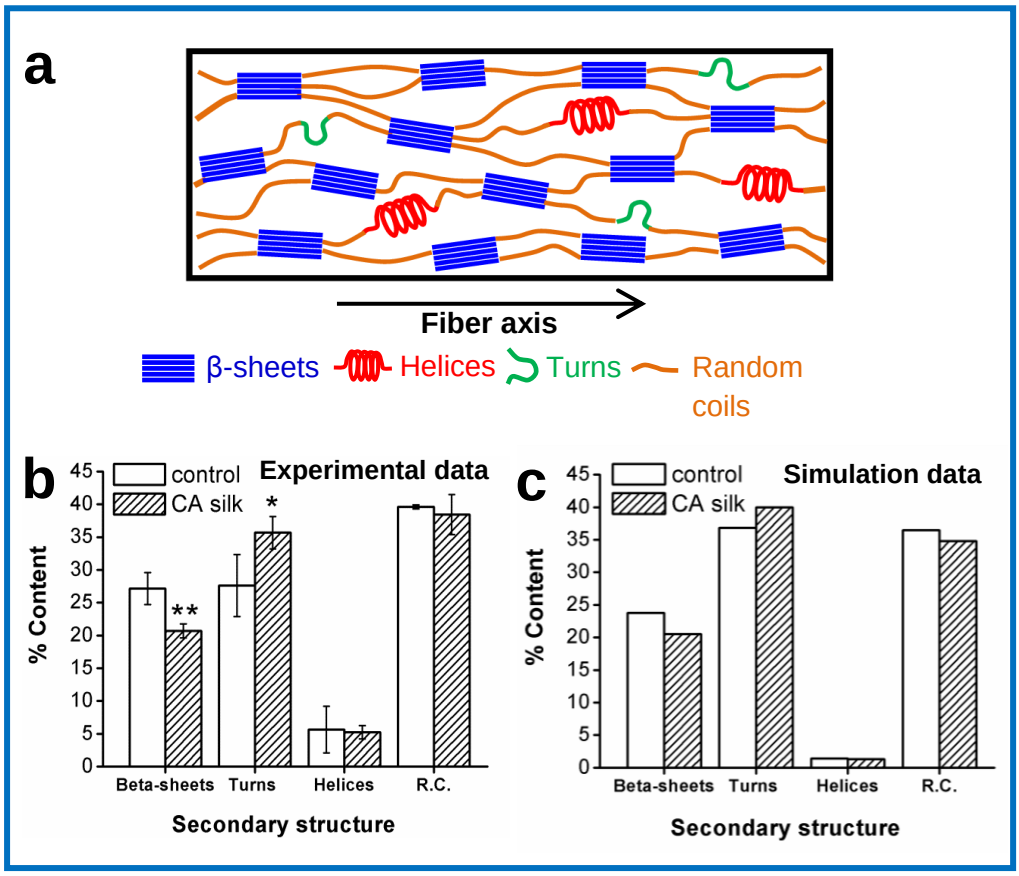

Figure 3.2 Structures in CA silk vs. control silk. (a) Structure representations of the silk fibroin fiber illustrating the hierarchical architecture, along with (b) the experimentally determined (i.e. FTIR) structural contents in CA silk vs. control silk (*p<0.10; **p<0.05; n=3). (c) The structural contents of silk fibroin folded in the presence and absence of CA (i.e., CA silk vs. control silk) simulated by molecular dynamics.

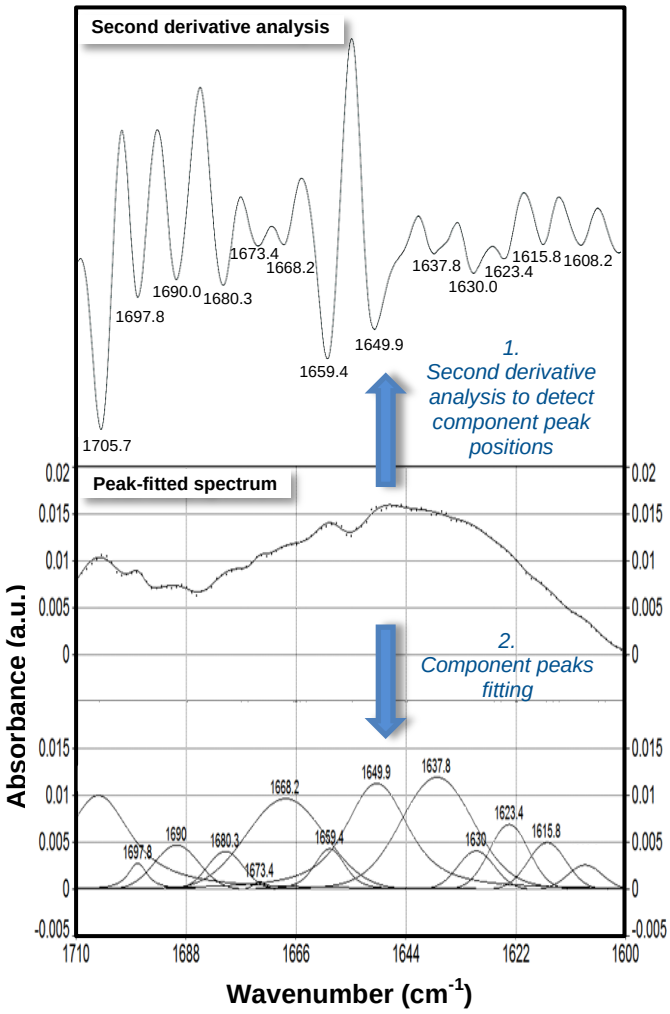

Wavenumber (cm^{-1})	Structural Assignment
1615.8	β-sheets
1623.4	β-sheets
1630.0	β-sheets
1637.8	Random coils
1649.9	Random coils
1659.4	Helices
1668.2	Turns
1673.4	Turns
1680.3	Turns
1690.0	Turns
1697.8	β-sheets

Figure 3.3 FTIR method to analyse structural contents of silk fibroin. Top, Structural component peak positions of the silk are identified by performing second derivative analysis in the 1600–1710 cm^{-1} region of the FTIR spectrum. Bottom, The dash line represents the original (i.e. pre-fitting) FTIR spectrum, while the solid line represents the spectral fit. Below the spectrum are the component peaks for structural assignments in silk fibroin (i.e., the peaks centred at 1615.8, 1623.4, 1630.0, 1637.8, 1649.9, 1659.4, 1668.2, 1673.4, 1680.3, 1690.0, and 1697.8 cm^{-1}) (see inset Table for structural assignments) [215–217].

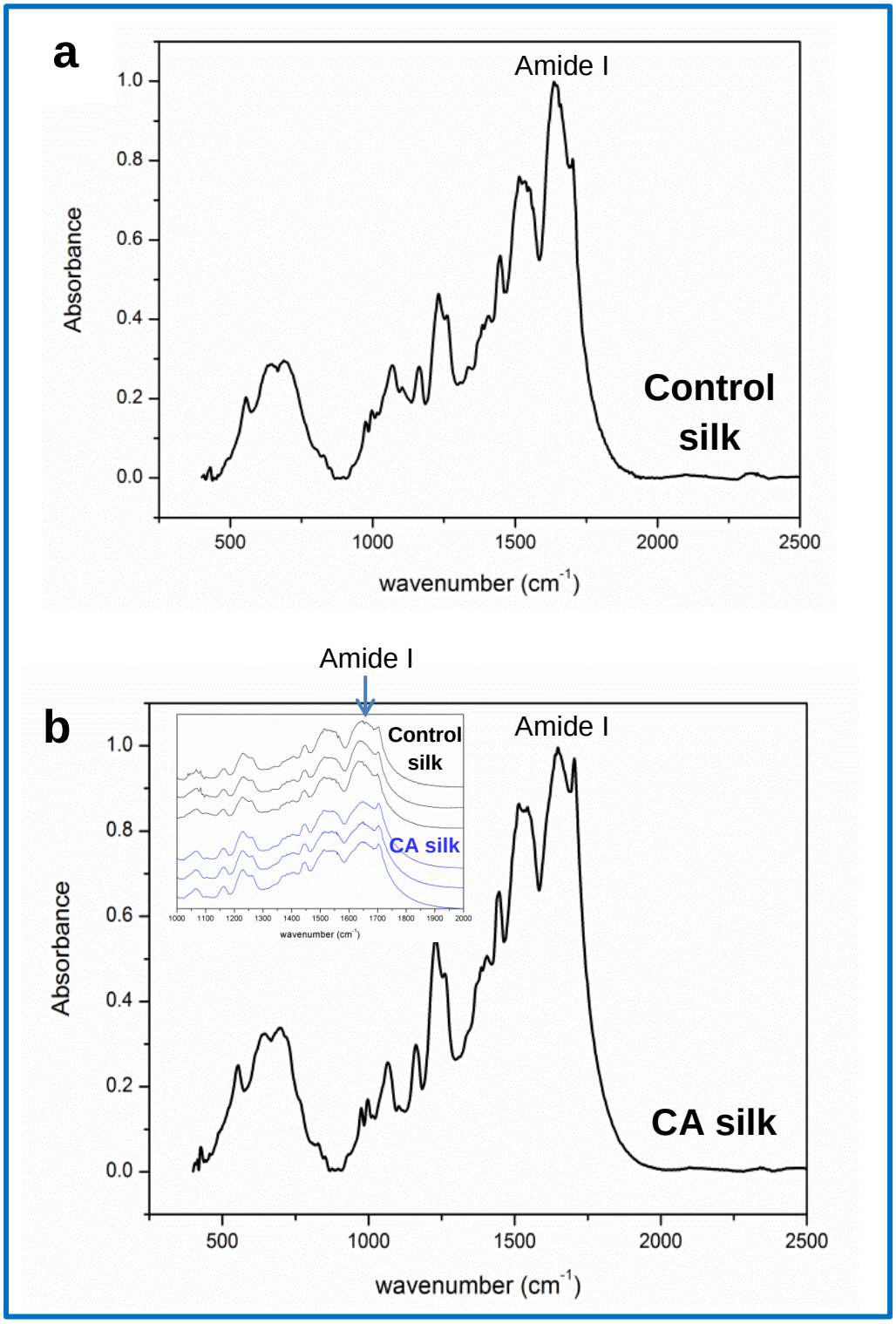

Figure 3.4 FTIR spectra of control silk (a) and CA silk (b), both normalized to the Amide I peak. Inset show individual spectrum of control and CA silks (1000 to 2000 cm^{-1}).

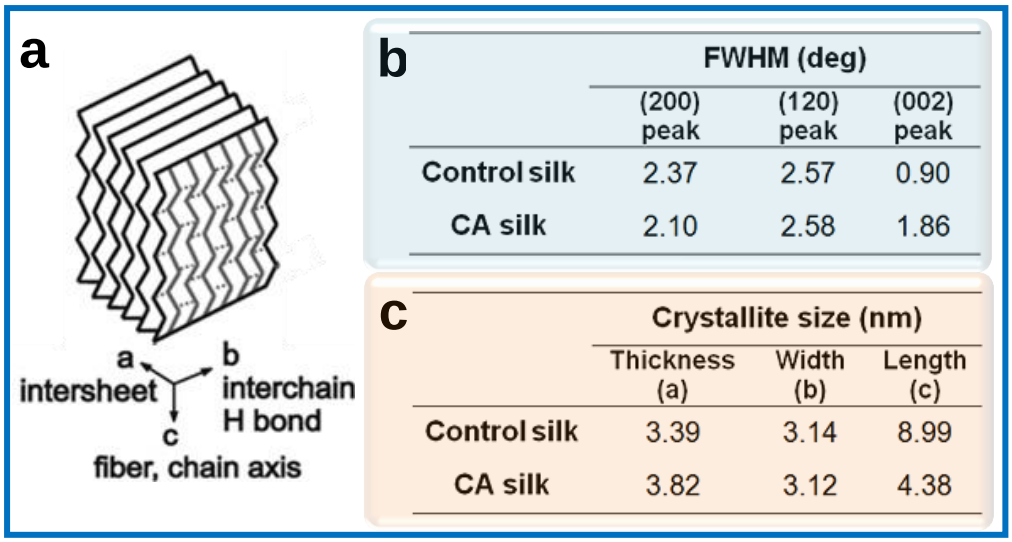

b

	FWHM (deg)		
	(200) peak	(120) peak	(002) peak
Control silk	2.37	2.57	0.90
CA silk	2.10	2.58	1.86

c

	Crystallite size (nm)		
	Thickness (a)	Width (b)	Length (c)
Control silk	3.39	3.14	8.99
CA silk	3.82	3.12	4.38

Figure 3.5 Silk fibroin crystallites. (a) Schematic drawing of a β-sheet crystallite with arrows indicating directions, where **a** is the direction along the stacking of β-sheets (i.e., thickness), **b** is the direction in a β-sheet perpendicular to the β-chain axis (i.e., width), and **c** is the direction along the chain axis (i.e., length). (b) FWHM of (200), (120), and (002) crystalline peaks of the CA silk and control silk, corresponding to the diffraction of planes in the **a**, **b** and **c** direction, respectively. (c) Crystallite sizes of the CA silk vs. control silk; a larger FWHM value corresponds to a smaller crystallite size.

The reduction in β-sheets content is further validated using Raman microspectroscopy, i.e. a non-invasive optical characterization method (no sample preparation is required, unlike IR techniques). It was also determined for CA silk a drastically reduced content of β-sheets (19.9%), as compared with control silk (38.9%). Collectively, these structural characterizations revealed that CA silk features significantly reduced content of β-sheets and unprecedentedly short β-sheet crystallites previously not observed in silkworm silk. The β-sheet crystallites are shorter along the β-chain axis direction as revealed by XRD, which coincides with the overall drop in the content of β-sheets.

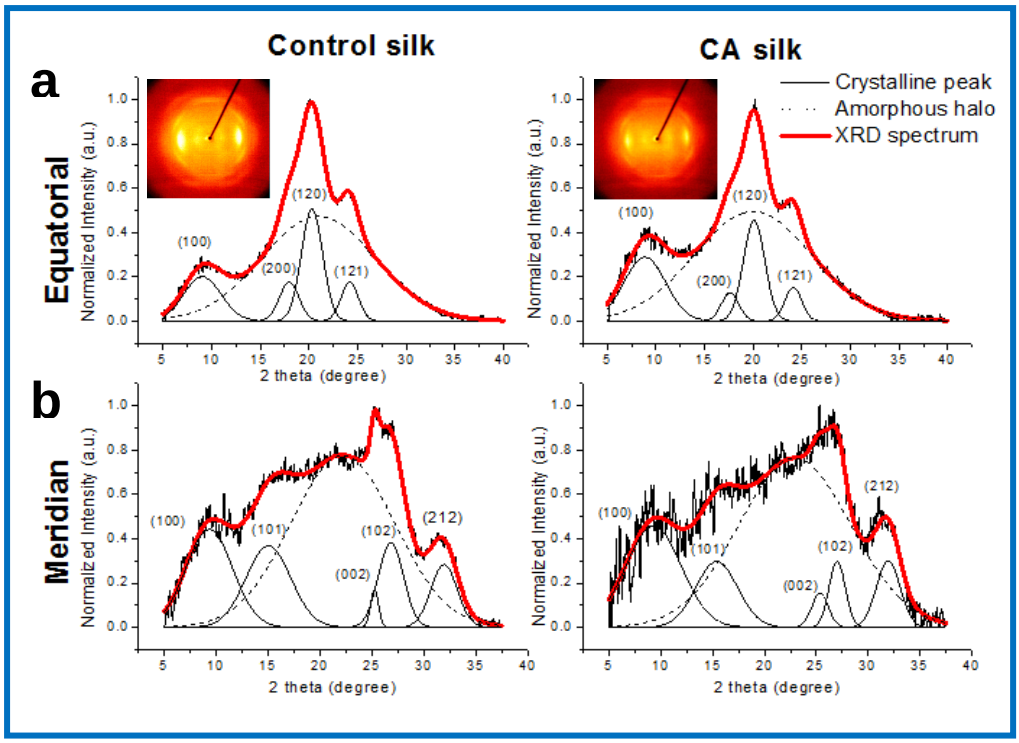

Figure 3.6 XRD of silk fibroin fibers. (a) equatorial XRD spectra of control silk vs. CA silk. (b) meridian XRD spectra of control silk vs. CA silk. All spectra were individually fitted into crystalline peaks. XRD patterns of the control silk and CA silk are also shown in inset.

3.3.2 Interaction of CA with silk fibroin

To understand the observed changes in the silk nanostructures, molecular dynamics simulations were performed to computationally assess the interaction of CA with fibroin during its organization from extended to folded configuration. The adopted fibroin molecule for the simulations comprises a crystalline sequence intercalated between two amorphous sequences, and is initially in extended configuration to represent the native unfolded fibroin (Figure 3.7). Two such molecules are placed in an antiparallel manner and subsequently allowed to fold into equilibrium, both in the absence (Figure 3.7a) and presence (Figure 3.7b) of CA respectively. In both cases, the equilibrated configurations consist of β-sheets, turns, helices and random coils. The CA greatly reduces the content of β-sheets in the folded configuration and increases the content of turns (Figure 3.2c) in agreement with

experimental findings described above (Figure 3.2b), as compared with the case in the absence of CA. Clearly, the CA markedly reduces the content of β-sheets in the folded fibroin configuration and led to the formation of shorter crystallites.

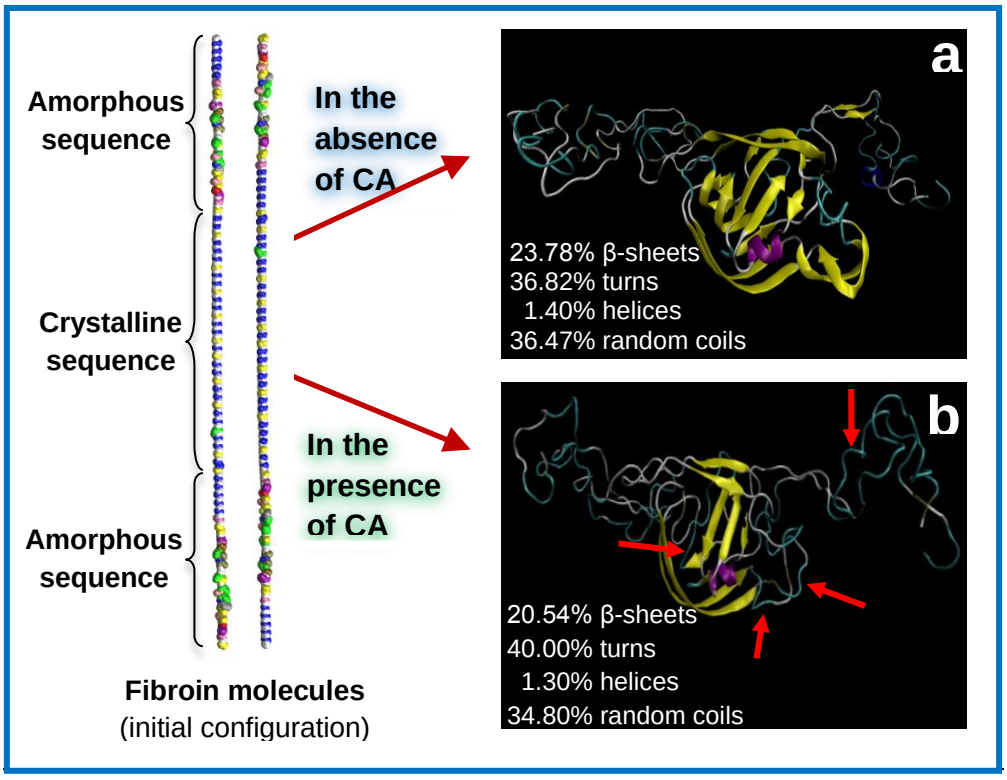

Figure 3.7 Molecular dynamics simulations – The folding of silk fibroin molecules in the absence or presence of CA molecules. Two extended fibroin molecules arranged in antiparallel manner are allowed to fold into equilibrium configuration, in the absence or presence of CA respectively. (a) Snapshot of the equilibrium fibroin configuration folded in the absence of CA. (b) Snapshot of the equilibrium fibroin configuration folded in the presence of CA. Yellow ribbons represent β-structures while green ribbons represent turns. The β-sheets structures disappear as indicated by red arrows.

The interaction of CA with fibroin β-sheet crystallites was investigated by molecular dynamics simulations. CA molecules were located between two β-sheet crystallites as initial configuration; each crystallite consists of a two-layer β-sheet structure extracted from Protein Data Bank (PDB) (Figure 3.8a). The CA, initially located between the two β-sheets crystallites, is spontaneously expelled out upon simulation

(Figure 3.8b) when the two β-sheet crystallites interact to form a four-layer β-sheet structure. The binding energy between a CA and a β-chain (i.e., a fibroin chain in the middle of a two-layer β-sheet) is -30.25 kJ/mol, which is greatly smaller than that between two β-chains (-96.74 kJ/mol). As a result, CA is readily expelled out in the event of the stacking between the β-sheet crystallites. Overall, these findings show that CA favorably interacts with silk fibroin to reduce the content of β-sheets while CA does not reside in fibroin crystallites.

3.3.3 Short crystallites in CA silk fibroin

The heavy chain of *Bombyx mori* silk fibroin is a 5,263-residues polypeptide, consisting of 2,377 repeats of GX as the building blocks of β-sheets in crystalline domain (G: glycine; X being A: alanine, S: serine, Y: tyrosine, V: valine or T: threonine) [6]. Of the 2,377 repeats of GX, there are ~4,421 small amino acid residues (glycine, alanine and serine) and ~333 bulky amino acid residues (tyrosine, valine and threonine). The ratio of small amino acids to bulky residues is 1:13, i.e., a ratio of one bulky residue to 13 small amino acids in the crystalline domain. It tends to form stable β-sheet crystallites of 13 small residues in length when the bulky residues are at the periphery of the crystallites. This is equivalent to a small crystallite of ~4.55 nm in length, calculated based on the standard distance of 3.5 Å for a peptide bond in a β-sheet [7]. Spectacularly, β-sheet crystallites of 4.38 nm in CA silk, a very close size to the predicted one, were obtained through feeding CA at 0.05 wt% in modified feed to silkworm, which resulted in intrinsically toughest silkworm silk. Without feeding CA, much lengthier β-sheet crystallites of 8.99 nm in control silk were obtained with weaker mechanical properties, indicating CA plays a critical role in greatly reducing the length of β-sheet crystallites to 4.38 nm in CA silk to greatly enhance mechanical properties. Correspondingly, the short crystallites in the CA silk have shorter β-chains of 13 residues, as compared with lengthier β-chains of 26 residues in the control silk.

In addition to 0.05 wt%, different weight percentages of CA from 0 to 1 wt% in feeds were also fed to silkworms, and different crystallites between 4 - 11 nm in length were obtained (Figure 3.9), corresponding to approximately 13, 16, 26 (control) and 31 residues in length. The mechanical properties varied proportionately with the crystallite length. As shown in Figure 3.9a, a higher ultimate strength was obtained with shorter crystallites in the silk. Likewise, a higher toughness (Figure 3.9b) of CA silk was also obtained with shorter crystallites in the silk. At 0.05 wt% CA, the best mechanical properties were achieved with shortest crystallites of 4.38 nm in the silk. Besides, β-sheet crystallites are known to unravel during loading through the breakage of hydrogen bonds between β-chains [56]. In comparison to lengthier crystallites, the short crystallites in the CA silk have lesser number of hydrogen bonds between β-chains and can unravel to release the length of protein chain with less difficulty. This allows the CA silk to deform plastically to a greater extent before fracture, endowing it with greatly enhanced toughness, as observed in the larger region of plastic deformation in the stress-strain curve of CA silk as compared to the control silk.

3.3.4 Concentration effect of CA on silk fibroin structures and mechanical properties

The concentration of CA in silk fibroin dope (i.e., fibroin in gland) after feeding silkworms with 0 (i.e., control), 0.05, 0.5 and 1.0 wt% of CA in feeds was determined. The crystallite length in the silk was found to decrease proportionately (i.e., a linear relationship) in response to an increase in the concentration of CA in the dope (Figure 3.9c), that in turn gave increasingly enhanced mechanical properties. Accordingly, the highest concentration of CA in the dope was achieved at the feeding of 0.05 wt% of CA, which resulted in the shortest crystallite in the silk that in turn gave the best ultimate strength and toughness.

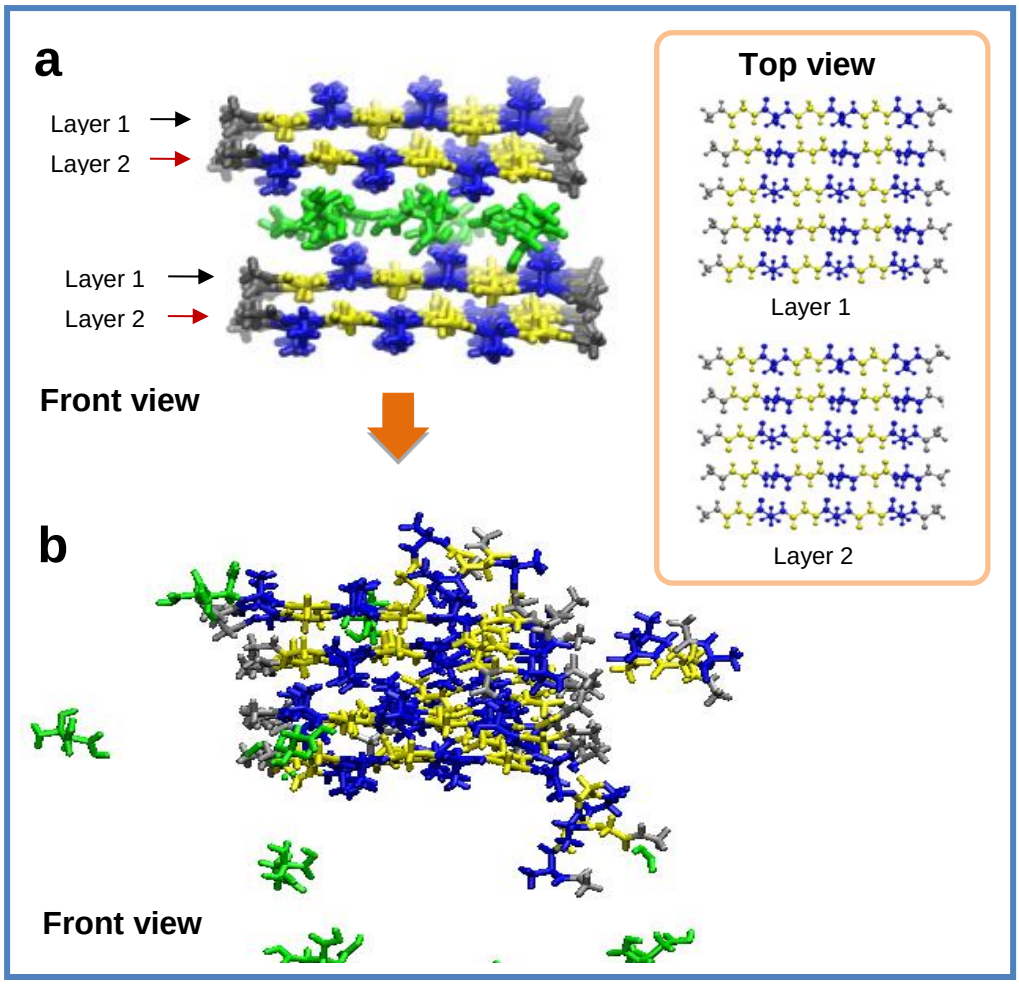

Figure 3.8 Molecular dynamics simulations – The fate of CA molecules in the crystalline domain of silk fibroin. (a) Initial configuration of poly(GA) crystallites and CA molecules. The glycine (G) residues are displayed in yellow and the alanine (A) residues are displayed in blue, and the chains are capped at both ends (cap residues displayed in grey). The CA molecules were located in between the two crystallites. (b) Snapshot of the configuration at 5 ns of molecular dynamics simulation: The CA molecules are expelled from the crystalline domain spontaneously.

Experimentally, after ingestion, CA was first transferred to the haemolymph of a silkworm through the gut epithelial (i.e., gut wall). As tabulated in (Figure 3.9c), a higher weight percentage of CA in feed led to a higher concentration of CA in the haemolymph. This can be attributed to the leaky gut wall, which allows hydrophilic molecules smaller than 400 Da to pass through via paracellular pathway into the haemolymph (molecular weight of CA = 192.12 Da) [218]. The CA was

subsequently transferred from the haemolymph into silk dope through amphiphilic lipid layers of gland epithelial (i.e. gland wall). Like the ionized forms (mono-, di- and tri-ionized citrates), neutral CA is also hydrophilic and readily dissolves in the haemolymph. Unlike the ionized forms, neutral CA can also dissolve in organic solvents (e.g. alcohol, ether, ethyl acetate) and is thus permeable through the gland wall into silk dope.

With feeding CA at 0.05 wt% in modified feed, the pH of the haemolymph is lowered from the typical value of 6.57 ± 0.02 (control) to 6.23 ± 0.04. In comparison, with feeding more CA at 1.0 wt%, the pH of the haemolymph was raised to 6.82 ± 0.07 (the higher pH is attributed to the alkalinizing effect of CA [219]). The haemolymph at the lower pH contains more CA in neutral form [220], and thus accounts for the higher uptake of CA into the dope. As further understood from energetic analysis, the neutral form of CA has also the strongest binding to fibroin, while the increasingly ionized forms have much weaker binding to fibroin (Table 3.2). Consequently, the neutral form of CA plays the most important role in the formation of short crystallites to strengthen the mechanical properties of the silkworm silk.

Table 3.2 Binding energy of a β-chain with a citric acid in its neutral (CA) or ionized forms (i.e., CA^- , CA^{2-}, CA^{3-}).

Interaction	**Binding energy (kJ/mol)**
Inter-chain	-96.74
One chain- one CA	-30.25
One chain- one CA^-	-22.71
One chain- one CA^{2-}	-20.29
One chain- one CA^{3-}	-16.21

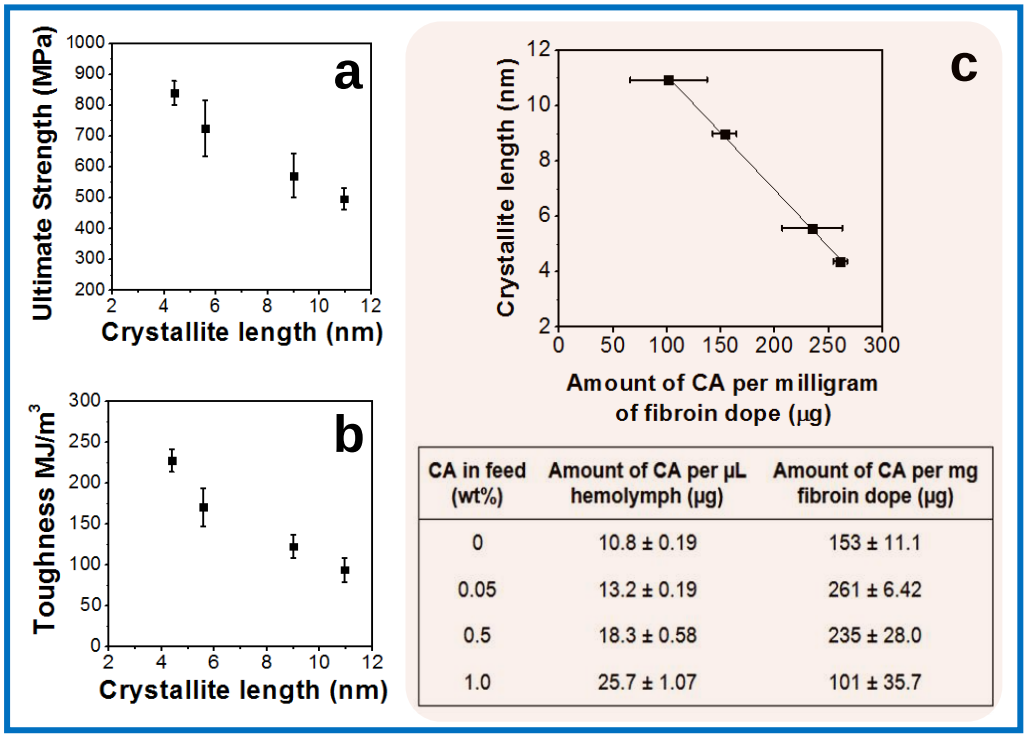

CA in feed (wt%)	Amount of CA per μL hemolymph (μg)	Amount of CA per mg fibroin dope (μg)
0	10.8 ± 0.19	153 ± 11.1
0.05	13.2 ± 0.19	261 ± 6.42
0.5	18.3 ± 0.58	235 ± 28.0
1.0	25.7 ± 1.07	101 ± 35.7

Figure 3.9 Enhanced mechanical properties of CA silk with shorter crystallites. (a,b) Ultimate tensile strength and toughness of silk fibroin fibers (n=5) as a function of crystallite length. (d) Crystallite length in silk fibroin fibers as a function of the concentration of CA in dried silk fibroin dopes obtained from silk glands (n=3). The concentration of CA in haemolymph and silk fibroin dope as a function of weight percentages (wt%) of CA in feed is tabulated.

3.4 Summary

In summary, we demonstrated a facile way to tune the structures at nanoscale to greatly toughen and strengthen the silkworm silk. By designing a feeding technique to drastically shorten the length of crystallites, we are able to simultaneously enhance both the strength and ductility of the silk through an enhanced architecture, providing a facile and versatile route to toughen the silk and widen its engineering applications [221]. The feeding technique presented here will contribute to the manufacture of intrinsically toughest silk fibers in a scalable, cost-effective, environmentally-friendly and sustainable manner, that will also reduce the environmental footprints of man-made fibers.

Chapter 4 Intrinsically Colored Silk

4.1 Introduction

Silk fibers are obtained from arthropods, most notably silkworms and spiders [222–224]. The *Bombyx mori* silkworm silk is the most widely used type of silk, which is highly prized for its superior aesthetic value and strength. The silkworm silk consists of a gummy outer layer (i.e., sericin) and core filaments (i.e., fibroin, here simply referred to as silk), which is made up of two domains: ordered β-sheet crystallites with strong hydrogen bonding, and disordered amorphous region with varying degrees of hydrogen bonding [4,52,54,69,83,194,225–228]. After removing sericin, the degummed silk (i.e., fibroin) has excellent biocompatibility and has been exploited to produce biomaterials in various forms such as sutures, drug delivery carriers and tissue engineering scaffolds [2,26]. In recent years, more efforts have been directed towards modifying properties or enhancing functionalities of silk by integrating with various materials, and the resulting functional silk has been used to make optical and electronic components in diagnostic and therapeutic devices, where biocompatibility, degradability and flexibility are required [229–231]. We foresee a great demand to produce various colored and functional silk materials containing stimuli-sensitive dyes and drugs (i.e., xenobiotics) that can be applied for wound dressing with monitoring/sensing features and tissue engineering scaffolds with anti-bacterial, anti-coagulant or anti-inflammatory features, and many others.

Xenobiotics are foreign substances in living organisms that are not produced *in vivo* and are not from normal diets, which have been extensively studied in the fields of genetics, proteomics, drug delivery, biooptics and biomaterials [2,54,232–235]. With normal feed containing no xenobiotics, silkworms usually produce white silk. In this study, through introducing xenobiotics into silkworm's diet and monitoring the

resulting color and fluorescence in the silkworm's body, we established an understanding on the *in vivo* uptake of xenobiotics in silkworms that leads to direct production of intrinsically colored and/or luminescent silk by the silkworms. The molecular properties-directed absorption, distribution and excretion of xenobiotics were investigated using a series of fluorescent molecules as model compounds in a silkworm model. Rhodamine dyes were included due to their wide applications in biology and biotechnology. The efficient uptake of xenobiotics into silk is further studied through quantitative analysis of the intrinsically colored and highly luminescent silk secreted by silkworm. Conventional dyeing of silk and silk fabrics/products into different colors involves harsh processing conditions such as high temperature and pH, and necessitates additional steps to remove excess dye molecules and to restore the original properties of silk. The biological incorporation of dyes into silk, in particular its fibroin is a greener method of producing the functional silk because it eliminates the need of an external dyeing process, along with the resources (water, energy and additional chemicals) associated with it. Beyond the absorption of dyes to produce color and luminescence in the silk, this feeding concept can also be expanded to incorporate other functional molecules (e.g., drugs, antibiotics, perfumes and nutrients) into silk with therapeutic or nutritional value. The findings will provide first-hand insights to better understand the molecular properties that allow specific materials to be incorporated into silk while it is being produced in the silk gland. Furthermore, this new development also paves a way to produce various functional silk embedded with stimuli-sensitive dyes or drugs as novel biomaterials for *in vivo* applications.

4.2 Materials and Methods

4.2.1 Materials

Rhodamine 101 (98%), Rhodamine 110 (99%), Rhodamine 116 (98%),

Rhodamine 123 (98%), Rhodamine B (98%), sulforhodamine 101 (95%), acridine orange (99%) and fluorescein sodium (95%) were obtained from Sigma Aldrich. All reagents were used without further purification.

4.2.2 Experimental methods

4.2.2.1 Preparation of silkworm feed

Normal feed was prepared by mixing 100 g mulberry powder (Recorp Inc, Canada) with 300 mL water followed by microwaving to make a thick green paste. Modified feed was prepared by thoroughly mixing 0.05 wt% of individual dyes into 50 g normal feed.

4.2.2.2 Culture and dissection of silkworms

Silkworms were cultured on normal feed until the second day of their fifth instar. Starting on the third day of their fifth instar, the silkworms were transitioned to modified feed containing various fluorescent molecules until they started spinning their cocoons. Dissection of the silkworms were carried out in Insect Ringer solution containing 128 mM NaCl, 1.8 mM $CaCl_2$. $2H_2O$, 1.3 mM KCl and 50 mM Tris. The extracted silk glands were placed in pH 6.6 phosphate buffer for imaging.

4.2.2.3 Measurement of partition coefficient

Each fluorescent dye was first dissolved in 1 mL MES buffer at a concentration of 1 µM and then partitioned with 1 mL octanol. MES buffer was used as the aqueous phase. The concentrations of the dye in each phase were determined using a Shimadzu RF-5301 fluorescence spectrophotometer.

4.2.2.4 Quantification of dye in silk

A piece of silk cocoon was weighed and degummed as described previously [235]. The resulting solution was measured using

fluorescence spectrophotometer to determine the amount of dye in silk sericin. The degummed silk was thoroughly rinsed and further dissolved by heating in 9 M LiBr solution at 70 °C for 3 h. The obtained solution was measured using fluorescence spectrophotometer to determine the amount of dye in silk fibroin. Total amount of dye in silk can be obtained by summing up these two components together.

4.3 Results and Discussion

4.3.1 Absorption of fluorescent xenobiotics in silkworms

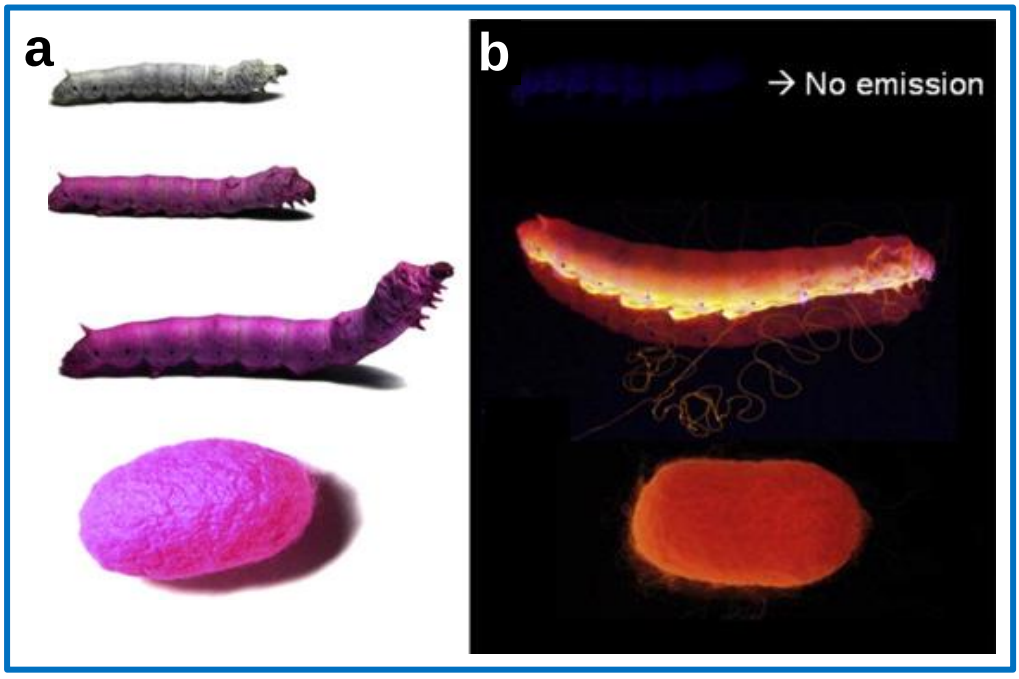

Figure 4.1 *In vivo* uptake of Rhodamine B into a silkworm to produce intrinsically colored and luminescent silk. Photographs documenting the development of silkworm fed with dye-modified feed from the third day of fifth instar until the complete formation of its cocoon, taken under room light (a) and UV irradiation (b).

A model xenobiotic compound, i.e., Rhodamine B (excitation wavelength: 540 nm; emission wavelength: 625 nm) was mixed into mulberry powder to make modified feed that was fed to silkworms starting from the third day of their fifth instar. Figure 4.1 illustrates the development of a typical silkworm from the start of consumption of

Rhodamine B until the formation of its cocoon. The *in vivo* absorption of Rhodamine B shows up as color change of the body of the silkworm, observable within two hours on the modified feed and became saturated within a day (Figure 4.1a). The silkworm appears highly fluorescent upon ultraviolet (UV) irradiation (Figure 4.1b). At the end of fifth instar, the silkworms on modified feed started producing intrinsically colored and highly luminescent silk, and the cocoons constructed from the silk appear pink under room light (appears orange under UV irradiation), as compared to those produced by silkworms on normal feed which appear white. Inside the cocoons, the silkworms developed normally into moths that produced eggs and second generation silkworms normally (Figure 4.2). This is an early indication that Rhodamine B was not toxic to the silkworms, as will be discussed later.

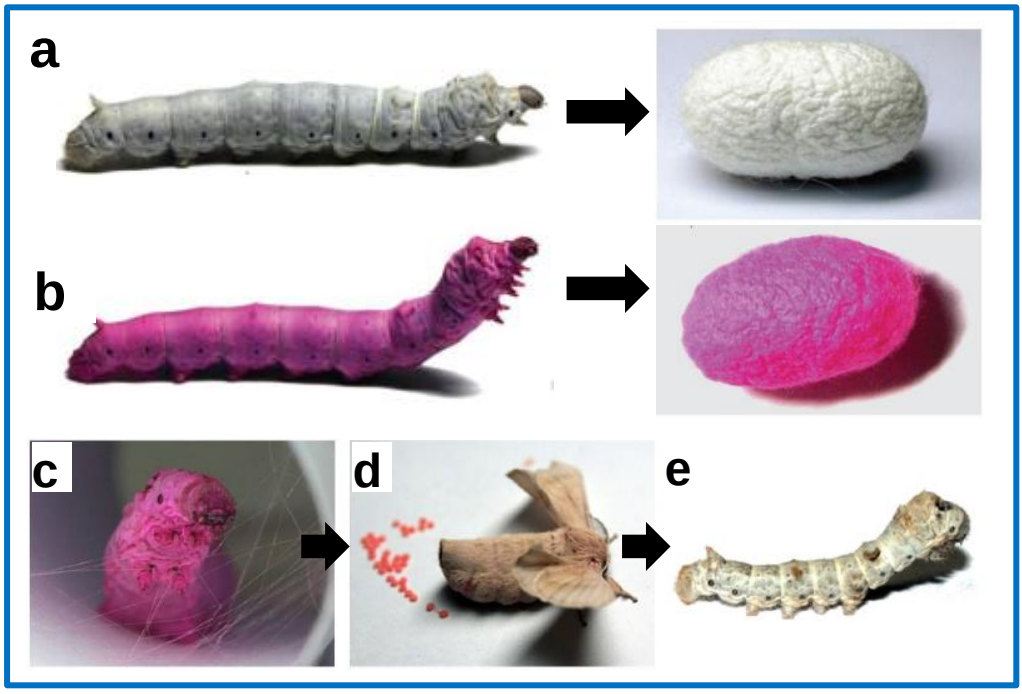

Figure 4.2 Intrinsically colored silk cocoon produced through effective uptake of Rhodamine B into a silkworm. (a) Photographs of a silkworm with normal feed and its resulting white cocoon. (b) Room-light photographs of a silkworm with modified feed containing Rhodamine B and its resulting colored cocoon. (c) A colored silkworm that has consumed Rhodamine B spinning its cocoon. (d) A moth from a silkworm that consumed Rhodamine B, producing colored eggs and (e)

the second generation silkworm that was hatched and grown from a colored egg.

4.3.2 Distribution of fluorescent xenobiotics into silk gland

To understand the production of colored and luminescent silk, silkworms were dissected at various points after feeding with modified feed. After two days of feeding, Rhodamine B was observed dominantly in the silk gland than the rest of the body, as shown in the photograph under room light (Figure 4.3a). Rhodamine B was found primarily in the wall of silk gland within the first 2 h of feeding, with negligible absorption into the gland lumen, as observed under UV irradiation (Figure 4.3c) (Gland content normally appears transparent or semi-transparent under room light, and since silk is a protein that absorbs strong the UV region, UV irradiation was used to enable clear visualization of the gland content). In the next two days, the concentration of Rhodamine B gradually increased in both the gland wall and lumen, indicating that the xenobiotic molecules were first absorbed throughout the gland wall and subsequently diffused into the gland lumen. At the end of the second day, the final concentration of the dye in the gland lumen (i.e., the silk) is visibly higher than that in the gland wall (i.e., the epithelial cells) as shown in Figure 4.3d. The distribution of acridine orange (excitation wavelength: 502 nm; emission wavelength: 526 nm) was investigated next. After two days of feeding, acridine orange was observed dominantly in the silkworm's fat body rather than the silk gland (Figure 4.3b). The acridine orange was only clearly observed in the silk gland wall after 12 h of feeding (Figure 4.3e). In the next two days, the concentration of acridine orange greatly increased in the gland wall, yet the concentration in the lumen was still very low (Figure 4.3f). In contrast to the finding for Rhodamine B which visibly dominates the gland content (i.e., the silk) (Figure 4.3d), after two days of feeding the concentration of acridine orange in the gland wall was visibly higher than the silk content in the gland lumen (Figure 4.3f).

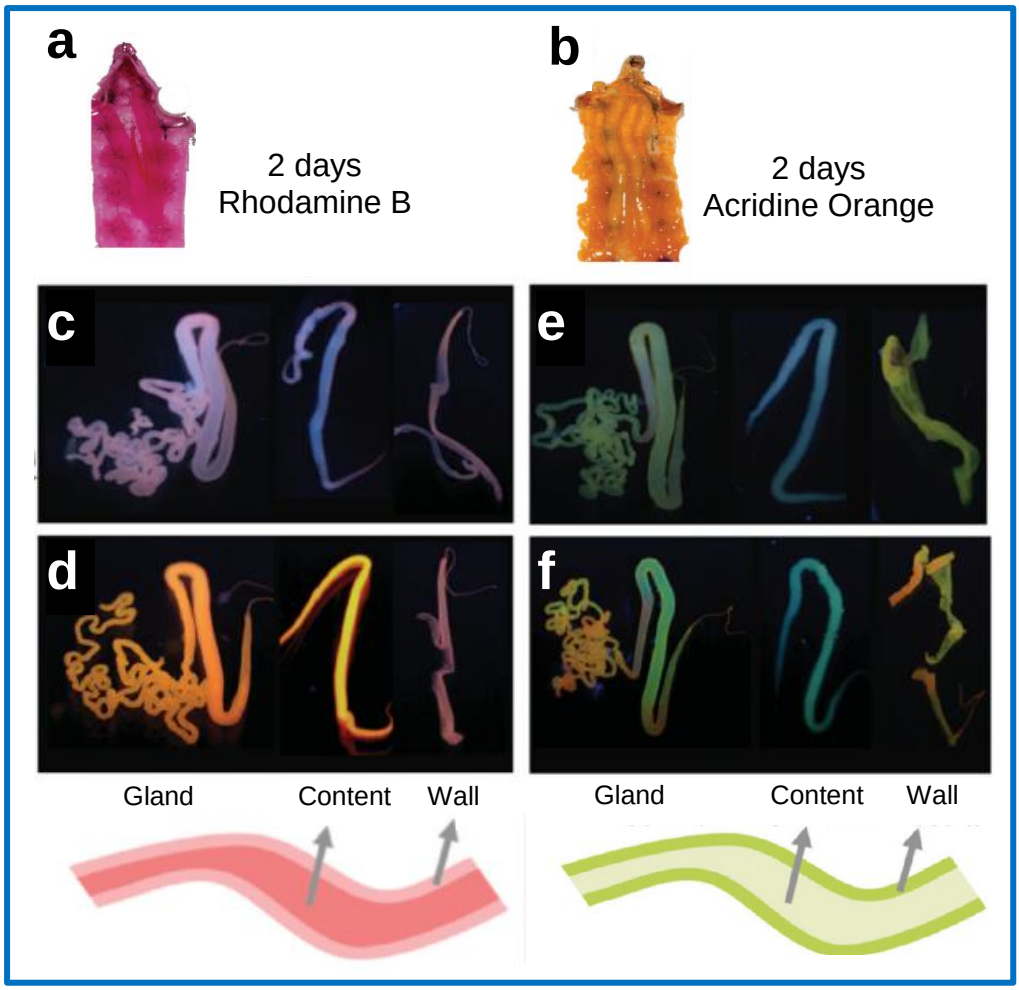

Figure 4.3 Molecular structure-dependent uptake led to spatial and temporal distribution of fluorescent molecules in silkworms, with dominant uptake of Rhodamine B into the lumen (i.e., silk content) and acridine orange in the epithelium (i.e., wall) of silk gland. Room-light photographs of dissected silkworms after two-day feeding with modified feed containing (a) Rhodamine B and (b) acridine orange. Photoluminescence photographs under UV irradiation of silk glands extracted from silkworms at various points of time after the start of feeding with modified feed: 2 h (c) and two days (d) with Rhodamine B, 12 h (e) and two days (f) with acridine orange, showing the whole silk gland (left), the peeled gland lumen (middle) and the gland epithelium (right).

Collectively, these experiments indicate that Rhodamine B dominantly distributes into the silk content inside gland lumen, whereas acridine orange retains more in silk gland wall with less penetration into the gland lumen. To verify the observed difference in the distribution of both dyes, it was further investigated the distribution of Rhodamine B

and acridine orange in a silkworm that had consumed an equimolar mixture of both dyes for two days (Figure 4.4a). Photographs of silk gland were taken under room light rather than UV irradiation to clearly differentiate the pink Rhodamine B in gland lumen from the yellow acridine orange in gland epithelium. In agreement with previous observation, acridine orange was found mainly on the epithelium of silk gland, while Rhodamine B was concentrated in the lumen of silk gland (Figure 4.4b).

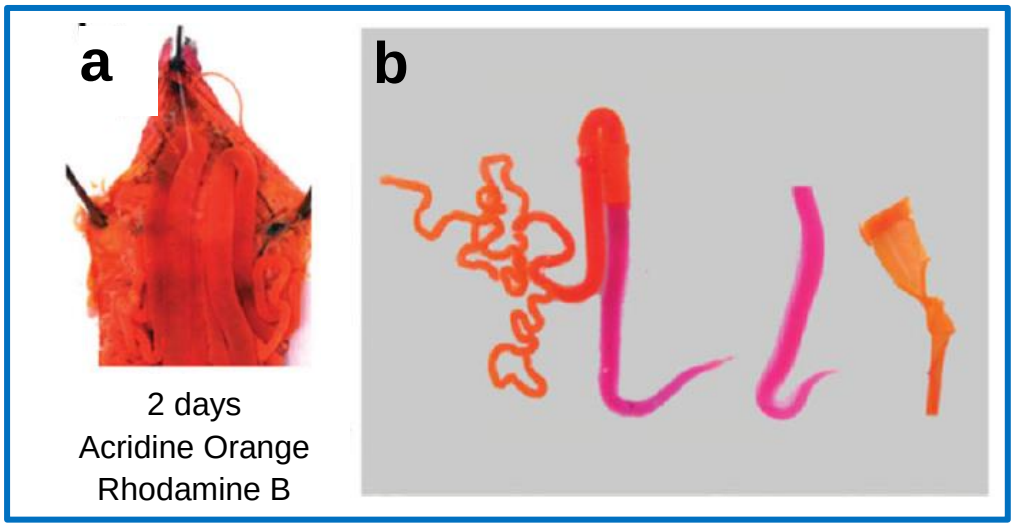

Figure 4.4 (a) Room-light photographs of dissected silkworms after two-day feeding with modified feed containing a mixture of Rhodamine B and acridine orange. (b) Room-light photographs of the silk gland of a silkworm after two-day feeding with a mixture of Rhodamine B and acridine orange in modified feed, showing the whole silk gland with partially peeled gland epithelium (left), the peeled gland lumen (middle) and the gland epithelium (right).

4.3.3 Clearance of fluorescent xenobiotics in silkworms

Upon absorption, the fate of xenobiotics could be conveniently monitored by visualizing the changes of color in the silkworm's body as displayed in Figure 4.5. In the first experiment, we started with two silkworms that were first fed Rhodamine B for 2 days, resulting in intensely pink silkworms (Figure 4.5a1). One of these two silkworms

was switched to normal food without the presence of any dye additives. Within one day, this silkworm lost most of its original pink shade (Figure 4.5a2). The other pink silkworm was switched to a modified feed containing acridine orange for the next 2 days. Again, the silkworm lost its original color and instead took up the orange shade from acridine orange (Figure 4.5a3).

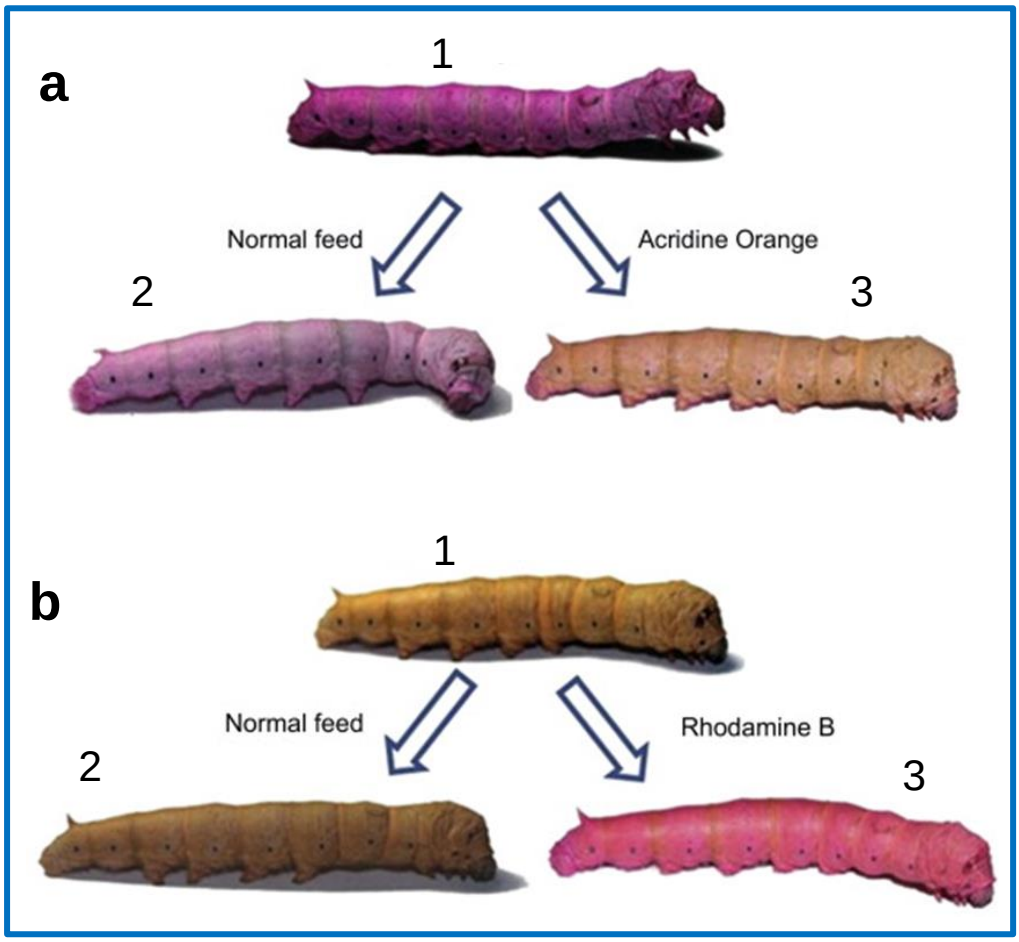

Figure 4.5 Comparison of uptake and clearance of Rhodamine B and acridine orange. The experiment started with silkworms on normal diet at the 3rd day of 5th instar. Two silkworms were then fed with Rhodamine B while the other two fed with acridine orange for 2 days, resulting in a pink silkworms for Rhodamine B (1,a) and orange silkworms for acridine orange (1,b). Next, one pink silkworm and one orange silkworm were switched to normal feed for two days (2,a), resulting in a less intensely colored pink silkworm for Rhodamine B and almost no change in color for acridine orange (2,b). In a parallel experiment, one pink silkworm and one orange silkworm were switched to diet containing the other dye: pink silkworm fed with acridine orange

(3,a), and orange silkworm fed with Rhodamine B (3,b) resulting in silkworms with mixed colors.

Figure 4.6 A comparison between silkworms after two days on modified feed (a), and two days on modified feed followed by two days on normal feed (b). For Rhodamine B, there was obvious loss of color from the silkworm's body due to the gradual clearance of dye. In contrast for acridine orange there was no observable difference when supply of dye was stopped because the existing dye molecules were strongly retained by in the silkworm body.

In the second experiment, we started with two silkworms that were fed with acridine orange for 2 days resulting in intensely orange silkworms (Figure 4.5b1). One of these silkworms was then switched to normal food without any dye additives. After one day or even up to seven days, the silkworm retained most of the original orange shade with no

appreciable change compared to the starting point (Figure 4.5b2). The other orange silkworm was switched to modified feed containing Rhodamine B for the next 2 days. Again, the silkworm maintained its orange color while at the same time absorbing the pink shade from Rhodamine B (Figure 4.5b3).

This shows the ability of Rhodamine B to quickly be absorbed into most parts of the organism, and at the same time also efficiently cleared once the consumption was stopped. On the other hand, acridine orange was also quickly absorbed and distributed, but was retained very strongly with no appreciable clearance. A similar observation was also observed upon dissection of the silkworm (Figure 4.6).

4.3.4 Effect of molecular lipophilicity

In addition to the qualitative observation as documented above, the uptake of xenobiotics was quantitatively investigated by characterizing the silk secreted from silkworms. Here we make use of the silkworms to produce intrinsically colored and luminescent cocoons, in which the high content of a dye in silk fibers reflects an efficient uptake of this dye from the silkworm's body into their silk glands. The convenient quantitative analysis can provide a better understanding of *in vivo* absorption and distribution of xenobiotics by correlating with their lipophilicity.

Various fluorescent xenobiotics with different visible and emission colors have been tested and successfully incorporated into the silkworm's body and silk. Aside from Rhodamine B, Rhodamine 110, Rhodamine 116 and Rhodamine 101 were also absorbed into silkworm's body and cocoons, resulting in both visible colors and luminescence under UV irradiation (Figure 4.7A–E). As shown in Figure 4.7E, the uptaken amounts of various fluorescent molecules into silk are nonlinearly dependent on their partition coefficients (log *P*), a measure of lipophicity.

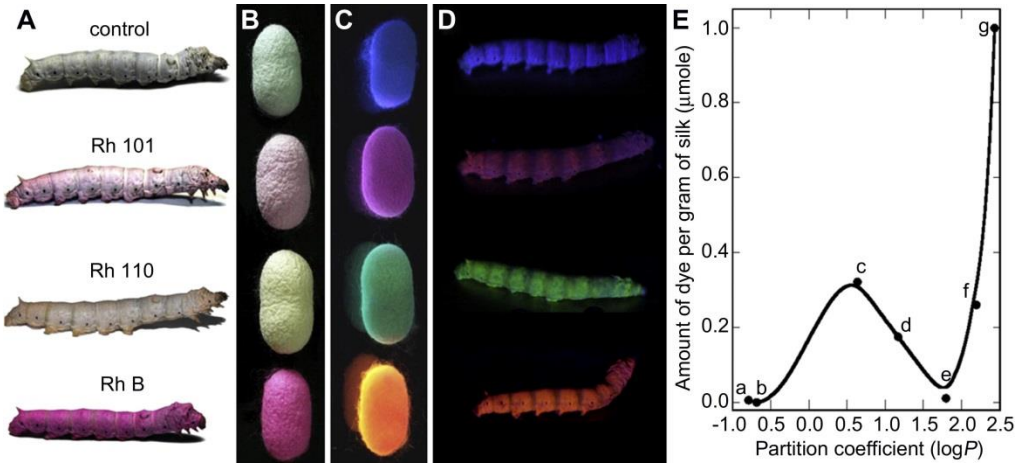

Figure 4.7 Absorption of various fluorescent xenobiotic compounds into silkworms and their silk. Room-light photographs of (A) silkworms and (B) cocoons taken under room light. Photoluminescence photographs of (D) silkworms and (C) cocoons taken under UV radiation. (E) The measured quantity of various fluorescent molecules in silk as a function of their partition coefficient (log *P*). a: fluorescein sodium (-0.79), b: sulforhodamine 101 (-0.69), c: Rhodamine 116 (0.64), d: Rhodamine 110 (1.17), e: acridine orange (1.80), f: Rhodamine 101 (2.19), g: Rhodamine B (2.43).

With negative log *P* at -0.79 and -0.69, highly hydrophilic fluorescein sodium and sulforhodamine 101 had negligible presence in silk (0.006 and 0.001 μmole/g) because of their rapid clearance out of the silkworm's body. With increased log *P*, lipophilicity, to a value similar to Thai golden silk (0.55), Rhodamine 116 was uptaken more in an amount two magnitudes higher in silk at 0.322 μmole/g. With a further increase of log *P* (>1), the absorption of fluorescent molecules into silk started to decrease due to reduced solubility. The amount of Rhodamine 110 (0.175 μmole/g) was around half that of Rhodamine 116, while acridine orange only has an even lower concentration in silk at 0.012 μmole/g. However, there was a sharp reversal of this trend observed for Rhodamine 101 and Rhodamine B. The amount of Rhodamine B was approximately 8 times, 16 times, and two magnitudes higher than Rhodamine 116, Rhodamine 110 and acridine orange, respectively, at ~ 1 μmole/g. This reversal signifies the

presence of another factor that determines *in vivo* distribution, as will be discussed next.

4.3.5 Effect of molecular self-assembly

Based on the quantification of Rhodamine B in silk (Figure 4.7E), the concentration of this dye in gland lumen at the start of silk spinning was estimated at 1 mM, and dimers would be formed at such high concentration [236]. Molecular self-assembly of Rhodamine B exposes either its hydrophilic carboxylic acid or hydrophobic ethyl groups outward to adjust the overall lipophilicity of the dimers, resulting in a more efficient transfer of Rhodamine B molecules from silk gland epithelium to silk in gland lumen eventually leading to production of intensely colored and luminescent silk. On the other hand, the concentration of acridine orange inside the silk gland lumen was very low. This is because the non-amphiphilic structure of acridine orange does not allow tuning of lipophilicity even upon the formation of dimers [237]. Although the concentration of acridine orange in silk gland epithelium cells was high, these molecules were unable to transfer to the more hydrophilic silk. Acridine orange was thus retained mainly in gland cells with very low uptake into gland lumen and negligible expression in silk. Molecular self-assembly therefore plays a significant part in determining the *in vivo* distribution of xenobiotics. Since different parts of the body have different levels of lipophilicity, amphiphilic molecules that can tune their lipophilicity through self-assembly would be able to achieve a better distribution *in vivo*.

4.3.6 Silkworms as animal model in xenobiotic screening

The attained understanding of molecular structure-dependent distribution and uptake of substances in a silkworm model is useful not only for producing intrinsically colored and functional silk but also for *in vivo* screening of xenobiotic chemicals relevant to humans such as drugs or food additives. Silkworms have been used as animal model

due to their ease of handling, low breeding cost and short lifecycle. The silkworms are also well suited for screening of various xenobiotics, specifically to understand their *in vivo* absorption, distribution and excretion, due to several additional reasons. First, the silkworms are much smaller than mice, allowing an observable color change with a small amount of xenobiotics. At the same time, the silkworms are much bigger than fruit flies, thus allowing easy monitoring with naked eyes. Second, the silkworms have simple anatomy, mainly occupied by their fat body and silk gland [81]. The silk gland is primarily made up of epithelial tissue, allowing convenient study of the transfer process across the epithelium into the lumen of the gland—a transfer that occurs before xenobiotic absorption into tissues or organs in various organisms. Third, the silkworms produce silk fiber, providing a practical way to quantify xenobiotic uptake into silk gland. A high expression of xenobiotic in silk implies a high absorption into silkworm's body and a selective distribution into the silk gland.

In the silkworm model presented here, the series of Rhodamine compounds investigated, including Rhodamine 110, Rhodamine 116, Rhodamine 101 and Rhodamine B were all effectively absorbed in silkworms, and their *in vivo* absorption can be conveniently quantified from their uptake in the silk fiber. They contain the carboxyl and amine groups which offer solubility/bioavailability in silkworms. The acidic carboxyl groups, –COOH transform into negatively charged $–COO^-$ in the alkaline environment of the silkworms's gut (pH 9.4–9.8 in midgut and pH 8.4 in hindgut) [238], leading to an increased solubility of these xenobiotics. Meanwhile, the basic amine groups become positively charged upon entering the silkworms's acidic haemolymph [81], also leading to an increased solubility. It is clear that the conversion between negative and positive charge in basic and acidic conditions can facilitate the highly effective absorption and excretion of these xenobiotics, and also allow their transfer between various tissues in the silkworms's body. For many applications, for example, to cross a biological membrane or barrier, a particle has to be hydrophobic, but

before and after it has to be hydrophilic [239]. Many drugs in human disease diagnostics/treatments are weak acids or weak bases which contain the carboxyl and/or amine groups. The biological diffusion of drugs through the stomach or intestinal epithelial lining for effective uptake into the blood plasma depends on solubility/bioavailability of the drugs based on these acidic or basic groups [240,241]. It was shown in this study that silkworms have a unique advantage as invertebrate animal model for chemical screening because the substances in silk glands can be systematically studied through analysis of the resulting silk, in addition to dissection of silkworms. Thus, the use of silkworm as an animal model for *in vivo* chemical screening presents an alternative animal model [242–244] for low-cost and high throughput screening of drug candidates.

4.4 Summary

In summary, it was demonstrated that with modified feed containing xenobiotics such as dyes, one is able to obtain direct production of intrinsically colored and/or luminescent silk by the silkworms. We established an understanding of *in vivo* absorption, distribution and excretion of various xenobiotics using silkworms as a model and a series of fluorescent molecules as model compounds. *In vivo* uptake of xenobiotics is dependent on both molecular structure and self-assembly properties. In comparison, molecules with lower partition coefficients were not retained due to their fast clearance out of the silkworm's body; molecules with higher partition coefficient are retained effectively. Moreover, the direct uptake of various fluorescent xenobiotics across the epithelia into silk glands into its silk lumen was studied and quantified by measuring the fluorescence of intrinsically luminescent silk secreted by the glands. We foresee a simple low-cost silkworm model that allows convenient *in vivo* screening of a large number of xenobiotics, as well as production of various silk-based biomaterials with added functionalities.

Chapter 5 Conclusion and Future Work

5.1 Conclusion

In this research, a green and facile feeding technique was designed to greatly enhance the toughness of the silkworm silk. Citric acid (CA) was added in mulberry leaf paste and fed to silkworms to effectuate structural changes in silk for great enhancement in mechanical properties. The CA silk features crystallites as short as 4.38 nm as compared to the control (8.99 nm). Correspondingly, the short crystallites in the CA silk have shorter β-chains of approximately 13 amino acid residues as compared with lengthier β-chains of approximately 26 amino acid residues in the control silk, which gave greatly enhanced toughness because the lesser number of hydrogen bonds associated with the shorter β-chains allows for unfolding upon stretching. The short crystallites of 4.38 nm are close to the predicted one at ~4.55 nm to form stable β-sheet crystallites of small residues in length (based on the ratio of small amino acids to bulky residues in the crystalline domain of 1:13, i.e., a ratio of one bulky residue to 13 small amino acids). Accordingly, the CA silk obtained in this study emerges to be the intrinsically toughest silkworm silk, with mechanical properties that surpass those of the previously reported silkworm silk, and compare well with or even exceed those of naturally produced spider silk, including those from spider species such as *Araneus diadematus*, *Nephila clavipes*, etc. The optimal enhancement in the mechanical properties was understood by both advanced characterizations and computational simulations, through revealing the underlying interactions of CA with fibroin structures as well as the resulting structural changes. This convenient way to tune the structures of silk fibroin at the nanoscale provides a green, facile and versatile route to toughen the silk and widen its engineering applications. This feeding technique presented here will contribute to manufacture mechanically toughest silk fibers in a scalable, cost-effective, environmentally-

friendly and sustainable manner, that will also reduce the environmental footprints of man-made fibers. The intrinsically toughest silk is expected to possess a range of unprecedented new functionalities which enable it as a natural substitute for many synthetic materials and open up possibilities for numerous novel applications.

Through introducing various xenobiotics into silkworm's diet and monitoring the resulting color and fluorescence in the silkworm's body, we established an understanding on the *in vivo* uptake of xenobiotics in silkworms that results in direct production of intrinsically colored and/or luminescent silk by the silkworms. The molecular properties-directed absorption, distribution and excretion of xenobiotics were investigated through dissection of the silkworms. The efficient uptake of xenobiotics into silk is further studied through quantitative analysis of the intrinsically colored and highly luminescent silk secreted by silkworm. *In vivo* uptake of xenobiotics is dependent on both molecular structure and self-assembly properties. Hydrophilic molecules were not retained due to their fast clearance out of the silkworm's body, whereas hydrophobic molecules were retained effectively by the silkworm. The findings provide a better understanding to select, design and synthesize appropriate molecules for improving uptake efficiency of substances into the silk. The biological incorporation of dyes into silk, in particular its fibroin is a greener method of producing the functional silk because it eliminates the need of an external dyeing process, along with the resources (water, energy and additional chemicals) associated with it.

5.2 Future Work

Beyond the absorption of dyes to produce color and luminescence in the silk, this concept can also be expanded to incorporate other functional molecules (e.g., drugs, antibiotics, perfumes and nutrients) into silk with therapeutic or nutritional value. The resulting functional

silks would offer novel applications with performance and utility unattainable with current materials. The feeding method can also be combined with other strategies to produce silk with further enhanced properties and functionalities, for example, the artificial reeling techniques that have been shown to produce stronger, stiffer and more extensible silk. Besides, the understanding gained on the mechanical behaviour of silk crystallites will be helpful in efforts to modify the silk, for example, by the incorporation of functional moieties to reduce the weakening effect of moisture, to further enhance the properties of silk fibroin.

References

1. Nagaraju, J. Silkworm Biology. 2004. [http://www.cdfd.org.in/SILKSAT/index.php?f=silkbio]

2. Altman GH, Diaz F, Jakuba C, Calabro T, Horan RL, Chen J, Lu H, Richmond J, Kaplan DL. Silk-based biomaterials, Biomaterials, *24,* pp.401-416. 2003.

3. Zhou P, Xie X, Knight DP, Zong XH, Deng F, Yao WH. Effects of pH and calcium ions on the conformational transitions in silk fibroin using 2D Raman correlation spectroscopy and 13C solid-state NMR, Biochemistry, *43,* pp.11302-11311. 2004.

4. Jin HJ, Kaplan DL. Mechanism of silk processing in insects and spiders, Nature, *424,* pp.1057-1061. 2003.

5. Vollrath F, Porter D. Silks as ancient models for modern polymers, Polymer *50,* pp.5623-5632. 2009.

6. Zhou CZ, Confalonieri F, Jacquet M, Perasso R, Li ZG, Janin J. Silk fibroin: structural implications of a remarkable amino acid sequence, Protein Struct. Funct. Genet., *44,* pp.119-122. 2001.

7. Foo CWP, Bini E, Hensman J, Knight DP, Lewis RV, Kaplan DL. Role of pH and charge on silk protein assembly in insects and spiders, Appl. Phys. A: Mater. Sci. Process, *82,* pp.223-233. 2006.

8. Willcox PJ, Gido SP, Muller W, Kaplan DL. Evidence of a Cholesteric Liquid Crystalline Phase in Natural Silk Spinning Processes, Macromolecules, *29,* pp.5106-5110. 1996.

9. Tao H, Amsden JJ, Strikwerda AC, Fan K, Kaplan DL, Zhang X, Averitt RD, Omenetto FG. Metamaterial silk composites at terahertz frequencies, Adv. Mater., *22,* pp. 3527-3531. 2010.

10. Anonymous. Fibre2Fashion.com. National Gem of China–the Silk Industry. 2009. [http://www.fibre2fashion.com/industry-article/17/1631/national-gem-of-china-the-silk-industry1.asp].

11. Vepari C, Kaplan DL. Silk as a biomaterial, Prog. Polym. Sci., *32,* pp.991-1007. 2007.

12. Rockwood DN, Preda RC, Yücel T, Wang X, Lovett ML, Kaplan DL. Materials fabrication from *Bombyx mori* silk fibroin, Nat. Protoc., *6,* pp.1612-1631. 2011.

13. Lu Q, Wang X, Zhu H, Kaplan DL. Surface immobilization of antibody on silk fibroin through conformational transition, Acta. Biomater., *7,* pp. 2782-2786. 2011.

14. Altman GH, Horan RL, Lu HH, Moreau J, Martin I, Richmond JC, Kaplan DL. Silk matrix for tissue engineered anterior cruciate ligaments, Biomaterials, *23,* pp.4131-4141. 2002.

15. Liu H, Fan H, Wang Y, Toh SL, Goh JC. The interaction between a combined knitted silk scaffold and microporous silk sponge with human mesenchymal stem cells for ligament tissue engineering, Biomaterials, *29,* pp.662-674. 2008.

16. Unger RE, Wolf M, Peters K, Motta A, Migliaresi C, James Kirkpatrick C. Growth of human cells on a non-woven silk fibroin net: a potential for use in tissue engineering, Biomaterials, *25,* pp.1069-1075. 2004.

17. Wang Y, Kim HJ, Vunjak-Novakovic G, Kaplan DL. Stem cell-based tissue engineering with silk biomaterials, Biomaterials, *27,* pp.6064-6082. 2006.

18. Tsioris K, Raja WK, Pritchard EM, Panilaitis B, Kaplan DL, Omenetto FG. Fabrication of Silk Microneedles for Controlled-Release Drug Delivery, Adv. Funct. Mater., *22,* pp.330-335. 2012.

19. Lawrence BD, Marchant JK, Pindrus MA, Omenetto FG, Kaplan DL. Silk film biomaterials for cornea tissue engineering, Biomaterials, *30,* pp.1299-1308. 2009.

20. Gil ES, Park SH, Marchant J, Omenetto F, Kaplan DL. Response of human corneal fibroblasts on silk film surface patterns, Macromol. Biosci., *10,* pp.664-673. 2010.

21. Gil ES, Mandal BB, Park SH, Marchant JK, Omenetto FG, Kaplan DL. Helicoidal multi-lamellar features of RGD-functionalized silk biomaterials for corneal tissue engineering, Biomaterials, *31,* pp.8953-8963. 2010.

22. Yang Y, Chen X, Ding F, Zhang P, Liu J, Gu X. Biocompatibility evaluation of silk fibroin with peripheral nerve tissues and cells in vitro, Biomaterials, *28,* pp.1643-1652. 2007.

23. Liu H, Ge Z, Wang Y, Toh SL, Sutthikhum V, Goh JC. Modification of sericin-free silk fibers for ligament tissue engineering application, J. Biomed. Mater. Res. B Appl. Biomater., *82,* pp.129-138. 2007.

24. Tao H, Brenckle MA, Yang M, Zhang J, Liu M, Siebert SM, Averitt RD, Mannoor MS, McAlpine MC, Rogers JA, Kaplan DL, Omenetto FG. Silk-based conformal, adhesive, edible food sensors, Adv. Mater., 24, pp.1067-1072. 2012.

25. Capelli R, Amsden JJ, Generali G, Toffanin S, Benfenati V, Muccini M, Kaplan DL, Omenetto FG, Zamboni R. Integration of silk protein in organic and light-emitting transistors, Org. Electron. *12,* pp.1146-1151. 2011.

26. Hakimi O, Knight DP, Vollrath F, Vadgama P. Spider and mulberry silkworm silks as compatible biomaterials, Compos. Part B-Eng., *38,* pp.324-337. 2007.

27. Numata K, Kaplan DL. Silk-based delivery systems of bioactive molecules, Adv. Drug Delivery Rev., *62,* pp.1497-1508. 2010.

28. Wenk E, Merkle HP, Meinel L. Silk fibroin as a vehicle for drug delivery applications, J. Controlled Release, *150,* pp.128-141. 2011.

29. Kaplan DL, Meinel L. Silk constructs for delivery of musculoskeletal therapeutics, Adv. Drug Delivery Rev., *64,* pp.1111-1122. 2012.

30. Kasoju N, Bora U. Silk Fibroin in Tissue Engineering, Adv. Healthcare Mater., *1,* pp.393-412. 2012.

31. Kundu B, Rajkhowa R, Kundu SC, Wang X. Silk fibroin biomaterials for tissue regenerations, Adv. Drug Delivery Rev., *65,* pp.457-470. 2013.

32. Kundu B, Kurland NE, Bano S, Patra C, Engel FB, Yadavalli VK, Kundu SC. Silk proteins for biomedical applications: Bioengineering perspectives, Prog. Polym. Sci., *39,* pp.251-267. 2014.

33. Zhang Q, Yan S, Li M. Silk Fibroin Based Porous Materials, Materials, *2,* pp.2276-2295. 2009.

34. Lawrence BD, Cronin-Golomb M, Georgakoudi I, Kaplan DL, Omenetto FG. Bioactive silk protein biomaterial systems for optical devices, Biomacromolecules, *9,* pp.1214-1220. 2008.

35. Tao H, Kaplan DL, Omenetto FG. Silk Materials – A Road to Sustainable High Technology, Adv. Mater., *24,* pp.2824-2837. 2012.

36. Hardy JG, Scheibel TR. Composite materials based on silk proteins, Prog. Polym. Sci., *35,* pp.1093-1115. 2010.

37. Hu X, Cebe P, Weiss AS, Omenetto F, Kaplan DL. Protein-based composite materials, Materials Today, *15,* pp.208-215. 2012.

38. Yamaguchi K, Kikuchi Y, Takagi T, Kikuchi A, Oyama F, Shimura K, Mizuno S. Primary structure of the silk fibroin light chain

determined by cDNA sequencing and peptide analysis, J. Mol. Biol., *210,* pp.127-139. 1989.

39. Zhou CZ, Confalonieri F, Medina N, Zivanovic Y, Esnault C, Yang T, Jacquet M, Janin J, Duguet M, Perasso R, Li ZG. Fine organization of *Bombyx mori* fibroin heavy chain gene, Nucleic Acids Res., *28,* pp.2413-2419. 2000.

40. Inoue S, Tanaka K, Arisaka F, Kimura S, Ohtomo K, Mizuno S. Silk fibroin of *Bombyx mori* is secreted, assembling a high molecular mass elementary unit consisting of H-chain, L-chain, and P25, with a 6:6:1 molar ratio, J. Biol. Chem., *275,* pp.40517-40528. 2000.

41. Takahashi Y, Gehoh M, Yuzuriha K. Structure refinement and diffuse streak scattering of silk (*Bombyx mori*), Int. J. Biol. Macromol., *24,* pp.127-138. 1999.

42. Marsh R, Corey RB, Pauling L. An investigation of the structure of silk fibroin. Biochim. Biophys. Acta., *16,* pp.1-34. 1955.

43. Bourne PE, Weissig H. Structural Bioinformatics, first ed. p. 649, Chichester: John Wiley & Sons. 2003.

44. Garrett RH, Grisham CM. Biochemistry, third ed. p. 1086, Belmont: Brooks Cole. 2007.

45. Kaplan DL. Fibrous proteins—silk as a model system, Polym. Degrad. Stabil., *59,* pp.25-32. 1998.

46. Fossey S, Némethy G, Gibson K, Scheraga H. Conformational energy studies of beta-sheets of model silk fibroin peptides. I. Sheets of poly(Ala-Gly) chains, Biopolymers, *31,* pp.1529-1541. 1991.

47. Chang S. (ed). X-ray Multiple-Wave Diffraction: Theory and Application. pp. 143-222, Berlin: Springer. 2010.

48. Ando I and Asakura T (eds). Studies in Physical and Theoretical Chemistry. pp. 853-890, Amsterdam: Elsevier. 1998.

49. Kameda T, Ohkawa Y, Yoshizawa K, Naito J, Ulrich AS, Asakura T. Hydrogen-bonding structure of serine side chains in *Bombyx mori* and *Samia cynthia ricini* silk fibroin determined by solid-state 2H NMR, Macromolecules, *32,* pp.7166-7171. 1999.

50. Asakura T, Sugino R, Okumura T, Nakazawa Y. The role of irregular unit, GAAS, on the secondary structure of *Bombyx mori* silk fibroin studied with 13C CP/MAS NMR and wide-angle X-ray scattering, Protein Sci., 11, pp.1873-1877. 2002.

51. Lim VI, Sternberg SV. A novel structural model for silk fibroin: $\alpha_L\alpha_R\beta$-structure, FEBS Lett., *131,* pp.203-207. 1981.

52. Sirichaisit J, Brookes VL, Young RJ, Vollrath F. Analysis of structure/property relationships in silkworm (*Bombyx mori*) and spider dragline (*Nephila edulis*) silks using raman spectroscopy, Biomacromolecules, *4,* pp.387-394. 2003.

53. Cunniff PM, Fossey SA, Auerbach MA, Song JW, Kaplan DL, Adams WW, Eby RK, Mahoney D, Vezie DL. Mechanical and thermal properties of dragline silk from the spider Nephila clavipes, Polym. Adv. Technol., *5,* pp.401-410. 1994.

54. Shao Z, Vollrath F. Surprising strength of silkworm silk, Nature, *418,* p.741. 2002.

55. Gosline JM, Guerette PA, Ortlepp CS, Savage KN. The mechanical design of spider silks: from fibroin sequence to mechanical function, J. Exp. Biol., *202,* pp.3295-3303. 1999.

56. Du N, Yang Z, Liu XY, Li Y, Xu HY. Structural Origin of the Strain-Hardening of Spider Silk, Adv. Funct. Mater., *21,* pp.772-778. 2011.

57. Krasnov I, Diddens I, Hauptmann N, Helms G, Ogurreck M, Seydel T, Funari SS, Müller M. Mechanical properties of silk: interplay of deformation on macroscopic and molecular length scales, Phys. Rev. Lett., *100,* pp.048104/1-4. 2008.

58. Keten S, Xu Z, Ihle B, Buehler MJ. Nanoconfinement controls stiffness, strength and mechanical toughness of beta-sheet crystals in silk, Nature Mater. *9,* pp.359-367. 2010.

59. Vollrath F, Madsen B, Shao Z. The effect of spinning conditions on the mechanics of a spider's dragline silk, Proc. R. Soc. B-Biol. Sci., *268,* pp.2339-2346. 2001.

60. Pins GD, Christiansen DL, Patel R, Silver FH. Self-assembly of collagen fibers. Influence of fibrillar alignment and decorin on mechanical properties, Biophys. J., *73,* pp.2164-2172. 1997.

61. Yang L, van der Werf KO, Fitié CF, Bennink ML, Dijkstra PJ, Feijen J. Mechanical properties of native and cross-linked type I collagen fibrils, Biophys. J., *94,* pp.2204-2211. 2008.

62. Li H, Donovan JA. Salt embrittlement of Nylon 6, Eng. Fract. Mech., *1,* pp.91-95. 2013.

63. Kumar S, Doshi H, Srinivasarao M, Park JO, Schiraldi DA. Fibers from polypropylene/nano carbon fiber composites, Polymer, *43,* pp.1701-1703. 2002.

64. Nova A, Keten S, Pugno NM, Redaelli A, Buehler MJ. Molecular and nanostructural mechanisms of deformation, strength and toughness of spider silk fibrils, Nano Lett., *10,* pp.2626-2634. 2010.

65. Wu X, Liu XY, Du N, Xu G, Li B. Unraveled mechanism in silk engineering: fast reeling induced silk toughening, Appl. Phys. Lett., 95, pp.093703/1-3. 2009.

66. Xia XX, Qian ZG, Ki CS, Park YH, Kaplan DL, Lee SY. Native-sized recombinant spider silk protein produced in metabolically engineered Escherichia coli results in a strong fiber, Proc. Natl. Acad. Sci. USA, 107, pp.14059-14063. 2010.

67. Du N, Liu XY, Narayanan J, Li L, Lim MLM, Li D. Design of superior spider silk: from nanostructure to mechanical properties, Biophys. J., *91,* pp.4528-4535. 2006.

68. Xiao S, Stacklies W, Cetinkaya M, Markert B, Gräter F. Mechanical response of silk crystalline units from force-distribution analysis, Biophys. J., 96, pp.3997-4005. 2009.

69. Pérez-Rigueiro J, Viney C, Llorca J, Elices M. Silkworm silk as an engineering material, J. Appl. Polym. Sci., *70,* pp.2439-2447. 1998.

70. Lawrence BD, Omenetto F, Chui K, Kaplan DL. Processing methods to control silk fibroin film biomaterial features, J. Mater. Sci., *43,* pp.6967-6985. 2008.

71. John MJ, Thomas S (eds). Natural Polymers. pp. 275-304, Cambridge Royal Society of Chemistry. 2012.

72. Drummy LF, Farmer BL, Naik RR. Correlation of the b-sheet crystal size in silk fibers with the protein amino acid sequence, Soft Matter, *3,* pp.877-882. 2007.

73. Liu XY, Du N. Enhanced silk protein material having improved mechanical performance and method of forming the same. US Patent 0,068,517 A1 filed on 12 Sep. 2007.

74. Pan H, Zhang Y, Shao H, Hu X, Li X, Tian F. Nanoconfined crystallites toughen artificial silk, J. Mater. Chem. B, *2,* pp.1408-1414. 2014.

75. Riekel C, Bränden C, Craig C, Ferrero C, Heidelbach F, Müller M. Aspects of X-ray diffraction on single spider fibers, Int. J. Biol. Macromol., *24,* pp.179-186. 1999.

76. Lefèvre T, Rousseau ME, Pézolet M. Protein Secondary Structure and Orientation in Silk as Revealed by Raman Spectromicroscopy, Biophys. J., *92,* pp.2885-2895. 2007.

77. Xu G, Gong L, Yang Z, Liu XY. What makes spider silk fibers so strong? From molecular-crystallite network to hierarchical network structures, Soft Matter, *10,* pp.2116-2123. 2014.

78. Armato U, Dal PI, Kesenci K, Migliaresi C, Motta A. Method for the preparation of non-woven silk fibroin fabrics. PTC WO Patent 02/29141 A1 filed on 28 Sep. 2001.

79. Unger RE, Peters K, Wolf M, Motta A, Migliaresi C, Kirkpatrick CJ. Endothelialization of a non-woven silk fibroin net for use in tissue engineering: growth and gene regulation of human endothelial cells, Biomaterials, *25,* pp.5137-5146. 2004.

80. Zhao HP, Feng XQ, Shi HJ. Variability in mechanical properties of *Bombyx mori* silk, Mater. Sci. Eng. C, *27,* pp.675-683. 2007.

81. Aruga, H. Principles of sericulture. pp. 133-264, New Delhi: Oxford and IBH Publishing Co, Pvt. Ltd. 1994.

82. Rahmathulla VK. Management of Climatic Factors for Successful Silkworm (*Bombyx mori L*.) Crop and Higher Silk Production: A Review, Psyche, pp.121234/1-12. 2012.

83. Vollrath F, Knight DP. Liquid crystalline spinning of spider silk, Nature, *410,* pp.541-548. 2001.

84. Servoli E, Maniglio D, Motta A, Migliaresi C. Folding and assembly of fibroin driven by an AC electric field: effects on film properties, Macromol. Biosci., *8,* pp.827-835. 2008.

85. Wen H, Lan X, Zhang Y, Zhao T, Wang Y, Kajiura Z, Nakagaki M. Transgenic silkworms (*Bombyx mori*) produce recombinant spider dragline silk in cocoons. Mol. Biol. Rep., *37,* pp.1815-1821. 2010.

86. Teulé F, Miao YG, Sohn BH, Kim YS, Hull JJ, Fraser MJ, Lewis RV, JarvisDL. Silkworms transformed with chimeric silkworm/spider silk genes spin composite silk fibers with improved mechanical properties, Proc. Natl. Acad. Sci. USA, *109,* pp.923-928. 2012.

87. Hu K, Cui F, Lv Q, Ma J, Feng Q, Xu L, Fan D. Preparation of fibroin/recombinant human-like collagen scaffold to promote fibroblasts compatibility. J. Biomed. Mater. Res. A, *84,* pp.483-490. 2008.

88. Wang Y, Kim UJ, Blasioli DJ, Kim HJ, Kaplan DL. In vitro cartilage tissue engineering with 3D porous aqueous-derived silk scaffolds and mesenchymal stem cells, Biomaterials, *26,* pp.7082-7094. 2005.

89. Wang Y, Blasioli DJ, Kim HJ, Kim HS, Kaplan DL. Cartilage tissue engineering with silk scaffolds and human articular chondrocytes, Biomaterials, *27,* pp.4434-4442. 2006.

90. Nazarov R, Jin HJ, Kaplan DL. Porous 3-D Scaffolds from Regenerated Silk Fibroin, Biomacromolecules, 5, pp.718-726. 2004.

91. Kim UJ, Park J, Kim HJ, Wada M, Kaplan DL. Three-dimensional aqueous-derived biomaterial scaffolds from silk fibroin, Biomaterials, *26,* pp.2775-2785. 2005.

92. Kluge JA, Rosiello NC, Leisk GG, Kaplan DL, Dorfmann AL. The consolidation behavior of silk hydrogels, J. Mech. Behav. Biomed. Mater., *3,* pp.278-289. 2010.

93. Jin HJ, Park J, Karageorgiou V, Kim UJ, Valluzzi R, Cebe P, Kaplan DL. Water-stable silk films with reduced β-sheet content, Adv. Funct. Mater., *15,* pp.1241-1247. 2005.

94. Jiang C, Wang X, Gunawidjaja R, Lin YH, Gupta MK, Kaplan DL, Naik RR, Tsukruk VV. Mechanical Properties of Robust Ultrathin Silk Fibroin Films, Adv. Funct. Mater., *17,* pp.2229-2237. 2007.

95. Ohgo K, Zhao C, Kobayashi M, Asakura T. Preparation of non-woven nanofibers of *Bombyx mori* silk, Samia cynthia ricini silk and recombinant hybrid silk with electrospinning method, Polymer, *44,* pp.841-846. 2003.

96. Ayutsede J, Gandhi M, Sukigara S, Micklus M, Chen HE, Ko F. Regeneration of *Bombyx mori* silk by electrospinning. Part 3: characterization of electrospun nonwoven mat, Polymer, *46,* pp.1625-1634. 2005.

97. Tsukada M, Freddi G, Minoura N, Allara G. Preparation and Application of Porous Silk Fibroin Materials, J. Appl. Polym. Sci., *54,* pp.507-514. 1994.

98. Uebersax L, Merkle HP, Meinel L. Insulin-like growth factor I releasing silk fibroin scaffolds induce chondrogenic differentiation of human mesenchymal stem cells, J. Controlled Release, *127,* pp.12-21. 2008.

99. Kim UJ, Park J, Li C, Jin HJ, Valluzzi R, Kaplan DL. Structure and properties of silk hydrogels, Biomacromolecules, *5,* pp.786-92. 2004.

100. Schacht EH. Polymer chemistry and hydrogel systems, J. Phys. Conf. Ser., *3,* pp.22-28. 2004.

101. Hardy JG, Scheibel TR. Composite materials based on silk proteins, Prog. Polym. Sci., *35,* pp.1093-1115. 2010.

102. Rujiravanit R, Kruaykitanon S, Jamieson AM, Tokura S. Preparation of crosslinked chitosan/silk fibroin blend films for drug delivery system, Macromol. Biosci., *3,* pp.604-611. 2003.

103. Kim DH, Viventi J, Amsden JJ, Xiao J, Vigeland L, Kim YS, Blanco JA, Panilaitis B, Frechette ES, Contreras D, Kaplan DL, Omenetto FG, Huang Y, Hwang KC, Zakin MR, Litt B, Rogers JA. Dissolvable films of silk fibroin for ultrathin conformal bio-integrated electronics, Nature Mater., *9,* 511-517. 2010.

104. Freddi G, Tsukada M, Beretta S. Structure and physical properties of silk fibroin/polyacrylamide blend films, J. Appl. Polym. Sci., *71,* 1563-1571. 1999.

105. Freddi G, Romanò M, Massafra MR, Tsukada M. Silk fibroin/cellulose blend films: preparation, structure, and physical properties. J. Appl. Polym. Sci., *56,* pp.1537-1545. 1995.

106. Lawrence BD, Wharram S, Kluge JA, Leisk GG, Omenetto FG, Rosenblatt MI, Kaplan DL. Effect of hydration on silk film material properties, Macromol. Biosci., *10,* pp.393-403. 2010.

107. Hu X, Shmelev K, Sun L, Gil ES, Park SH, Cebe P, Kaplan DL. Regulation of silk material structure by temperature-controlled water vapor annealing, Biomacromolecules, *12,* pp.1686-1696. 2011.

108. Ghosh S, Laha M, Mondal S, Sengupta S, Kaplan DL. *In vitro* model of mesenchymal condensation during chondrogenic development, Biomaterials, *30,* pp.6530-6540. 2009.

109. Sun Y, Shao Z, Ma M, Hu P, Liu Y, Yu T. Acrylic polymer–silk fibroin blend fibers, J. Appl. Polym. Sci., *65,* pp.959-966. 1997.

110. He J, Wang Y, Cui S, Gao Y, Wang S. Structure and properties of silk fibroin/carboxymethyl chitosan blend films, Polym. Bull., *65,* pp.395-409. 2010.

111. Mandal BB, Kapoor S, Kundu SC. Silk fibroin/polyacrylamide semi-interpenetrating network hydrogels for controlled drug release, Biomaterials, *30,* pp.2826-2836. 2009.

112. Pritchard EM, Kaplan DL. Silk fibroin biomaterials for controlled release drug delivery, Expert Opin. Drug. Deliv., *8,* pp.797-811. 2011.

113. Lv Q, Hu K, Feng Q, Cui F. Fibroin/collagen hybrid hydrogels with crosslinking method: preparation, properties, and cytocompatibility, J. Biomed. Mater. Res. A, *84,* pp.198-207. 2008.

114. Tao H, Kainerstorfer JM, Siebert SM, Pritchard EM, Sassaroli A, Panilaitis BJ, Brenckle MA, Amsden JJ, Levitt J, Fantini S, Kaplan DL, Omenetto FG. Implantable, multifunctional, bioresorbable optics, Proc. Natl. Acad. Sci. USA., *109,* pp.19584-19589. 2012.

115. Müller C, Hamedi M, Karlsson R, Jansson R, Marcilla R, Hedhammar M, Inganäs O. Woven electrochemical transistors on silk fibers, Adv. Mater., *23,* pp.898-901. 2011.

116. Dubas ST, Kumlangdudsana P, Potiyaraj P. Layer-by-layer deposition of antimicrobial silver nanoparticles on textile fibers, Colloid Surface A, *289,* pp.105-109. 2006.

117. Li G, Liu H, Zhao H, Gao Y, Wang J, Jiang H, Boughton RI. Chemical assembly of TiO2 and TiO2@Ag nanoparticles on silk fiber to produce multifunctional fabrics, J. Colloid Interface Sci., *358,* pp.307-315. 2011.

118. Gupta MK, Khokhar SK, Phillips DM, Sowards LA, Drummy LF, Kadakia MP, Naik RR. Patterned silk films cast from ionic liquid solubilized fibroin as scaffolds for cell growth, Langmuir, *23,* pp.1315-1319. 2007.

119. Perry H, Gopinath A, Kaplan DL, Dal Negro L, Omenetto FG. Nano- and micropatterning of optically transparent, mechanically robust, biocompatible silk fibroin films, Adv. Mater. *20,* pp.3070-3072. 2008.

120. Iizuka T, Sezutsu H, Tatematsu K, Kobayashi I, Yonemura N, Uchino K, Nakajima K, Kojima K, Takabayashi C, Machii H, Yamada K, Kurihara H, Asakura T, Nakazawa Y, Miyawaki A, Karasawa S, Kobayashi H, Yamaguchi J, Kuwabara N, Nakamura T, Yoshii K, Tamura T. Colored Fluorescent Silk Made by Transgenic Silkworms, Adv. Funct. Mater., 23, pp.5232-5239. 2013.

121. Lu YH, Lin H, Chen YY, Wang C, Hua YR. Structure and Performance of *Bombyx mori* Silk Modified with Nano-TiO_2 and Chitosan, Fiber Polym., *8,* 1-6. 2007.

122. Lin N, Toh GW, Feng Y, Liu XY, Xu H. Two-photon fluorescent *Bombyx mori* silk by molecular recognition functionalization, J. Mater. Chem. B, *2,* pp.2136-2143. 2014.

123. Aznar-Cervantes S, Roca MI, Martinez JG, Meseguer-Olmo L, Cenis JL, Moraleda JM, Otero TF. Fabrication of conductive electrospun silk fibroin scaffolds by coating with polypyrrole for biomedical applications, Bioelectrochemistry, *85,* pp.36-43. 2012.

124. Leksophee T, Supansomboon S, Sombatsompop N. Effects of Crosslinking Agents, Dyeing Temperature, and pH on Mechanical Performance and Whiteness of Silk Fabric, J. Appl. Polym. Sci., *91,* pp.1000-1007. 2004.

125. Raja WK, MacCorkle S, Diwan IM, Abdurrob A, Lu J, Omenetto FG, Kaplan DL. Transdermal Delivery Devices: Fabrication, Mechanics and Drug Release from Silk, Small, *9,* pp.3704-3713. 2013.

126. Ray LG. The Role of Synthetic Fibers in the Textile Industry of the Future, Text. Res. J., 22, pp.144-151. 1952.

127. Sofia S, McCarthy MB, Gronowicz G, Kaplan DL. Functionalized silk-based biomaterials for bone formation, J. Biomed. Mater. Res., *54,* pp.139-148. 2001.

128. Bhardwaj N, Kundu SC. Electrospinning: A fascinating fiber fabrication technique, Biotechnol. Adv., *28,* pp.325-347. 2010.

129. Masini BD, Stinner DJ, Waterman SM, Wenke JC. Bacterial adherence to high–tensile strength sutures, Arthroscopy, 27, pp.834-838. 2011.

130. Tomita N, Tamai S, Morihara T, Ikeuchi K, Ikada Y. Handling Characteristics of Braided Suture Materials for Tight Tying, J. Appl. Biomater., *4,* pp.61-65. 1993.

131. Viju S, Thilagavathi G. Characterization of tetracycline hydrochloride drug incorporated silk sutures, J. Text. I., *104,* pp.289-294. 2013.

132. Postlethwait RW, Willigan DA, Ulin AW. Human tissue reaction to sutures. Ann. Surg., *181,* pp.144-150. 1975.

133. Nideffer J. Suture in the Operating Room. 2010. [http://www.surgical-instrument-pictures.com/suture.html]

134. Drury JL, Mooney DJ. Hydrogels for tissue engineering: scaffold design variables and applications, Biomaterials, *24,* pp.4337-4351. 2003.

135. Lavik E, Langer R. Tissue engineering: current state and perspectives, Appl. Microbiol. Biot., *65,* pp.1-8. 2004.

136. Kjaer M. Role of Extracellular Matrix in Adaptation of Tendon and Skeletal Muscle to Mechanical Loading, Physiol. Rev., *84,* pp.649-698. 2004.

137. Wang JHC. Mechanobiology of tendon, J. Biomech., *39,* pp.1563-1582. 2006.

138. Oatis CA (ed). Kinesiology: the mechanics and pathomechanics of human movement. p.66-79, Philadelphia: Lippincott Williams and Wilkins. 2003.

139. Zioupos P, Currey JD. Changes in the Stiffness, Strength, and Toughness of Human Cortical Bone With Age, Bone, *22,* pp.57-66. 1998.

140. Clark JA, Cheng JCY, Leung KS. Mechanical properties of normal skin and hypertrophic scars, Burns, *22,* pp.443-446. 1996.

141. Laurencin CT, Ambrosio AM, Borden MD, Cooper JA Jr. Tissue engineering: orthopedic applications, Annu. Rev. Biomed. Eng., *1,* pp.19-46. 1999.

142. Vunjak-Novakovic G, Altman G, Horan R, Kaplan DL. Tissue engineering of ligaments, Annu. Rev. Biomed. Eng., *6,* pp.131-156. 2004.

143. Engler AJ, Griffin MA, Sen S, Bönnemann CG, Sweeney HL, Discher DE. Myotubes differentiate optimally on substrates with tissue-like stiffness: pathological implications for soft or stiff microenvironments, J. Cell Biol., *166,* pp.877-887. 2004.

144. Engler AJ, Sen S, Sweeney HL, Discher DE. Matrix elasticity directs stem cell lineage specification, Cell, *126,* pp.677-689. 2006.

145. Holst J, Watson S, Lord MS, Eamegdool SS, Bax DV, Nivison-Smith LB, Kondyurin A, Ma L, Oberhauser AF, Weiss AS,Rasko JE. Substrate elasticity provides mechanical signals for the expansion of hemopoieticstem and progenitor cells, Nat. Biotechnol., *28,* pp.1123-1128. 2010.

146. Hu X, Park SH, Gil ES, Xia XX, Weiss AS, Kaplan DL. The influence of elasticity and surface roughness on myogenic and osteogenic-differentiation of cells on silk-elastin biomaterials, Biomaterials, *32,* pp.8979-8989. 2011.

147. Dal Pra I., Freddi G., Minic J., Chiarini A., Armato U. De novo engineering of reticular connective tissue in vivo by silk fibroin nonwoven materials, Biomaterials, *26,* pp.1987-1999. 2005.

148. Laurencin CT, Freeman JW. Ligament tissue engineering: An evolutionary materials science approach, Biomaterials, *26,* pp.7530-7536. 2005.

149. Yates EW, Rupani A, Foley GT, Khan WS, Cartmell S, Anand SJ. Ligament tissue engineering and its potential role in anterior cruciate ligament reconstruction, Stem Cells Int., pp.438125/1-6. 2012.

150. Meinel L, Hofmann S, Karageorgiou V, Zichner L, Langer R, Kaplan D, Vunjak-Novakovic G. Engineering cartilage-like tissue using human mesenchymal stem cells and silk protein scaffolds, Biotechnol. Bioeng., *88,* pp.379-391. 2004.

151. Meinel L, Karageorgiou V, Fajardo R, Snyder B, Shinde-Patil V, Zichner L, Kaplan D, Langer R, Vunjak-Novakovic G. Bone tissue engineering using human mesenchymal stem cells: effects of scaffold material and medium flow, Ann. Biomed. Eng., *32,* pp.112-122. 2004.

152. Yucel T, Cebe P, Kaplan DL. Vortex-induced injectable silk fibroin hydrogels, Biophys. J., *97,* pp.2044-2050. 2009.

153. Motta A, Migliaresi C, Faccioni F, Torricelli P, Fini M, Giardino R. Fibroin hydrogels for biomedical applications: preparation, characterization and in vitro cell culture studies, J. Biomater. Sci., Polym. Ed., *15,* pp.851-864. 2004.

154. Fini M, Motta A, Torricelli P, Giavaresi G, Nicoli Aldini N, Tschon M, Giardino R, Migliaresi C. The healing of confined critical size cancellous defects in the presence of silk fibroin hydrogel, Biomaterials, *26,* pp.3527-3536. 2005.

155. Arai T, Freddi G, Innocenti R, Tsukada M. Biodegradation of *bombyx mori* silk fibroin fibers and films, J. Appl. Polym. Sci., *91,* pp.2383-2390. 2004.

156. Meinel L, Hofmann S, Karageorgiou V, Kirker-Head C, McCool J, Gronowicz G, Zichner L, Langer R, Vunjak-Novakovic G, Kaplan DL. The inflammatory responses to silk films in vitro and in vivo, Biomaterials, 26, pp.147-155. 2005.

157. Ayutsede J, Gandhi M, Sukigara S, Micklus M, Chen HE, Ko F. Regeneration of *Bombyx mori* silk by electrospinning. Part 3: characterization of electrospun nonwoven mat, Polymer, *46,* pp.1625-1634. 2005.

158. Ghosh S, Parker ST, Wang X, Kaplan DL, and Lewis JA. Direct-Write Assembly of Microperiodic Silk Fibroin Scaffolds for Tissue Engineering Applications, Adv. Funct. Mater. *18,* pp.1883-1889. 2008.

159. Li C, Vepari C, Jin HJ, Kim HJ, Kaplan DL. Electrospun silk-BMP-2 scaffolds for bone tissue engineering, Biomaterials, *27,* pp.3115-3124. 2006.

160. Numata K, Kaplan DL. Silk-Based Gene Carriers with Cell Membrane Destabilizing Peptides, Biomacromolecules, *11,* pp.3189-3195. 2010.

161. Numata K, Hamasaki J, Subramanian B, Kaplan DL. Gene delivery mediated by recombinant silk proteins containing cationic and cell binding motifs, J. Controlled Release, *146,* pp.136-143. 2010.

162. Uebersax L, Mattotti M, Papaloïzos M, Merkle HP, Gander B, Meinel L. Silk fibroin matrices for the controlled release of nerve growth factor (NGF), Biomaterials, *28,* pp.4449-4460. 2007.

163. Lu S, Wang X, Lu Q, Hu X, Uppal N, Omenetto G, Kaplan DL. Stabilization of enzymes in silk films, Biomacromolecules, *10,* pp.1032-1042. 2009.

164. Lu Q, Wang X, Hu X, Cebe P, Omenetto F, Kaplan DL. Stabilization and release of enzymes from silk films, Macromol. Biosci.,*10,* pp.359-368. 2010.

165. Numata K, Kaplan DL. Silk-based delivery systems of bioactive molecules, Adv. Drug Deliv. Rev., *62,* pp.1497-1508. 2010.

166. Guziewicz N, Best A, Perez-Ramirez B, Kaplan DL. Lyophilized silk fibroin hydrogels for the sustained local delivery of therapeutic monoclonal antibodies, Biomaterials, *32,* pp.2642-2650. 2011.

167. Kundu J, Poole-Warren LA, Martens P, Kundu SC. Silk fibroin/poly(vinyl alcohol) photocrosslinked hydrogels for delivery of macromolecular drugs, Acta Biomater., *8,* pp.1720-1729. 2012.

168. Dinerman AA, Cappello J, Ghandehari H, Hoag SW. Swelling behavior of a genetically engineered silk-elastinlike protein polymer hydrogel, Biomaterials, *23,* pp.4203-4210. 2002.

169. Elia R, Newhide DR, Pedevillano PD, Reiss GR, Firpo MA, Hsu EW, Kaplan DL, Prestwich GD, Peattie RA. Silk-hyaluronan-based composite hydrogels: a novel, securable vehicle for drug delivery, J. Biomater. Appl., *27,* pp.749-762. 2013.

170. Kundu J, Patra C, Kundu SC. Design, fabrication and characterization of silk fibroin-HPMC-PEG blended films as vehicle for transmucosal delivery, Mat. Sci. Eng. C, *28,* pp.1376-1380. 2008.

171. Raja WK, Maccorkle S, Diwan IM, Abdurrob A, Lu J, Omenetto FG, Kaplan DL. Transdermal delivery devices: fabrication, mechanics and drug release from silk, Small, *9,* pp.3704-3713. 2013.

172. Serwer L, Hashizume R, Ozawa T, James CD. Systemic and Local Drug Delivery for Treating Diseases of the Central Nervous System in Rodent Models, J. Vis. Exp., pp.42/1-5. 2010.

173. Coelho J (ed). Drug delivery systems: advanced technologies potentially applicable in personalised treatment. p.318-321, New York: Springer Dordrecht. 2013.

174. Wang X, Kluge JA, Leisk GG, Kaplan DL. Sonication-induced gelation of silk fibroin for cell encapsulation, Biomaterials, *29,* pp.1054-1064. 2008.

175. Kim K, Cheng J, Liu Q, Wu XY, Sun Y. Investigation of mechanical properties of soft hydrogel microcapsules in relation to protein delivery using a MEMS force sensor, J. Biomed. Mater. Res. A, *92,* pp.103-113. 2010.

176. Nicodemus GD, Bryant SJ. Cell Encapsulation in Biodegradable Hydrogels for Tissue Engineering Applications, Tissue Eng, Part B Rev., *14,* pp.149-165. 2008.

177. Yu B, West L, Moussy Y, Moussy F. Transcutaneous Implantation Methods for Improving the Long-Term Performance of Glucose Sensors in Rats, IEEE Sens. J., *8,* pp.97-103. 2008.

178. Parker ST, Domachuk P, Amsden J, Bressner J, Lewis JA, Kaplan DL, Omenetto FG. Biocompatible Silk Printed Optical Waveguides, Adv. Mater., *21,* pp.2411-2415. 2009.

179. Domachuk P, Perry H, Amsden JJ, Kaplan DL, Omenetto FG. Bioactive “self-sensing” optical systems, Appl. Phys. Lett., 95, pp.253702/1-3. 2009.

180. Amsden JJ, Domachuk P, Gopinath A, White RD, Negro LD, Kaplan DL, Omenetto FG. Rapid nanoimprinting of silk fibroin films for biophotonic applications, Adv. Mater., *22,* pp.1746-1749. 2010.

181. Mannoor MS, Tao H, Clayton JD, Sengupta A, Kaplan DL, Naik RR, Verma N, Omenetto FG, McAlpine MC. Graphene-based wireless bacteria detection on tooth enamel, Nat. Commun. 3, pp.763/1-8. 2012.

182. Zhong J, Ma M, Zhou J, Wei D, Yan Z, He D. Tip-induced micropatterning of silk fibroin protein using in situ solution atomic force microscopy, ACS Appl. Mater. Inter., 5, pp.737-746. 2013.

183. Ma H, Jen AKY, Dalton LR. Polymer-Based Optical Waveguides: Materials, Processing, and Devices, Adv. Mater., *14,* pp.1339-1365. 2002.

184. Stegeman GI, Stolen RH. Waveguides and fibers for nonlinear optics, J. Opt. Soc. Am. B, *6,* pp.652-662. 1989.

185. Kaplan DL, Omenetto F, Lawrence B, Cronin-Golomb M, Georgakoudi I. Biopolymer optical waveguide and method of manufacturing the same. US Patent 20100063404 A1 filed on 5 Nov. 2007.

186. Jacobs JM. Suggested guidelines for the handling of optical fiber. 2001. [http://www.corning.com/docs/opticalfiber/wp3627_12-01.pdf]

187. Hsu TR. Miniaturization – A paradigm shift in advanced manufacturing and education. In IEEE/ASME International Conference on Advanced Manufacturing Technologies and Education, August 2002, Chia-Yi, Taiwan, pp. 1-19.

188. Huby N, Vié V, Renault A, Beaufils S, Lefèvre T, Paquet-Mercier F, Pézolet M, Bêche B. Native spider silk as a biological optical fiber, Appl. Phys. Lett., *102,* pp.123702/1-8. 2013.

189. Gatesy J, Hayashi C, Motriuk D, Woods J, Lewis R. Extreme diversity, conservation, and convergence of spider silk fibroin sequences. Science, *291,* pp.2603-2605. 2001.

190. Brookes VL, Young RJ, Vollrath F. Deformation micromechanics of spider silk, J. Mater. Sci., *43,* pp.3728-3732. 2008.

191. Cetinkaya M, Xiao S, Markert B, Stacklies W, Gräter F. Silk fiber mechanics from multiscale force distribution analysis, Biophys. J., *100,* pp.1298-1305. 2011.

192. Plaza GR, Guinea GV, Perez-Rigueiro J, Elices M. Thermo-hydro-mechanical behavior of spider dragline silk: gassy and rubbery states, J. Polym. Sci. Part B: Polym. Phys., *44,* pp.994–999. 2006.

193. Poza P, Perez-Rigueiro J, Elices M, Llorca J. Fractographic analysis of silkworm and spider silk, Eng. Fract. Mech., *69,* pp.1035-1048. 2002.

194. Pérez-Rigueiro J, Viney C, Llorca J, Elicesa M. Mechanical properties of silkworm silk in liquid media, Polymer, *41,* pp.8433-8439. 2000.

195. Fu C, Porter D, Shao Z. Moisture effects on *Antheraea pernyi* silk's mechanical property, Macromolecules, *42,* pp.7877-7880. 2009.

196. Cornell WD, et al. A second generation force field for the simulation of proteins, nucleic acids, and organic molecules, J. Am. Chem. Soc., *117,* pp.5179-5197. 1995.

197. Jorgensen WL, Chandrasekhar J, Madura JD, Impey RW, Klein ML. Comparison of simple potential functions for simulating liquid water, J. Chem. Phys., *79,* pp.926-935. 1983.

198. Darden T, York D, Pedersen L. Particle mesh Ewald—an N.Log (N) method for Ewald sums in large systems, J. Chem. Phys., *98,* pp.10089-10092. 1993.

199. Hess B, Kutzner C, van der Spoel D, Lindahl E. GROMACS 4: algorithms for highly efficient, load-balanced, and scalable molecular simulation, J. Chem. Theory Comput., *4,* pp.435-447. 2008.

200. Sotomayor M, Schulten K. Single-molecule experiments *in vitro* and *in silico*, Science, *316,* pp.1144-1148. 2007.

201. Li D, Ji B, Hwang K, Huang Y. Crucial roles of the subnanosecond local dynamics of the flap tips in the global conformational changes of HIV-1 protease, J. Phys. Chem. B, *114,* pp.3060-3069. 2010.

202. Li D, Ji B, Hwang K, Huang Y. Strength of hydrogen bond network takes crucial roles in the dissociation process of inhibitors from the HIV-1 protease binding pocket, PLoS ONE, *6,* e19268. 2011.

203. Luzar A, Chandler D. Hydrogen-bond kinetics in liquid water, Nature, *379,* pp.55-57. 1996.

204. Sheu SY, Yang DY, Selzle HL, Schlag EW. Energetics of hydrogen bonds in peptides, Proc. Natl Acad. Sci. USA, *100,* pp.12683-12687. 2003.

205. She Z, Zhang B, Jin C, Feng Q, Xu Y. Preparation and *in vitro* degradation of porous three-dimensional silk fibroin/chitosan scaffold, Polym. Degrad. Stabil., *93,* pp.1316-1322. 2008.

206. Fibroin reinforcement process of fragile silk. CN Patent 101424042B filed on 3 Nov. 2008. [http://www.google.com/patents/CN101424042B]

207. Timár-Balázsy Á, Eastop D. Chemical principles of textile conservation. Butterworth-Heinemann: Oxford. 2002.

208. Zhou P, Li G, Shao Z, Pan X, Yu T. Structure of Bombyx mori Silk Fibroin Based on the DFT Chemical Shift Calculation, J. Phys. Chem., *105,* pp.12469-12476. 2001.

209. Vollrath F, Porter D, Holland C. There are many more lessons still to be learned from spider silks, Soft Matter, *7,* pp.9595-9600. 2011.

210. Case DA, *et al.* AMBER 9. University of California, San Francisco, pp. 225-230. 2006.

211. Hess B, Kutzner C, van der Spoel D, Lindahl E. GROMACS 4: Algorithms for Highly Efficient, Load-Balanced, and Scalable Molecular Simulation, J. Chem. Theory Comput., *4,* pp.435-447. 2008.

212. Humphrey W, Dalke A, Schulten K. VMD: visual molecular dynamics, J. Mol. Graph., *14,* pp.33-38. 1996.

213. Jorgensen WL, Chandrasekhar J, Madura JD, Impey RW, Klein ML. Comparison of simple potential functions for simulating liquid water, J. Chem. Phys., *79,* pp.926-935. 1983.

214. McGrath K, Kaplan DL. Silk Protein-Based Materials. Boston: Birkhäuser. 1997.

215. Tretinnikov ON, Tamada Y. Influence of Casting Temperature on the Near-Surface Structure and Wettability of Cast Silk Fibroin Films, Langmuir, *17,* pp.7406-7413. 2001.

216. Beniash E, Simmer JP, Margolis HC. Structural Changes in Amelogenin upon Self-assembly and Mineral Interactions, J. Dent. Res, *91,* pp.967-972. 2012.

217. Venkataramani S, Truntzer J, Coleman DR. Thermal stability of high concentration lysozyme across varying pH: A Fourier Transform Infrared study, J. Pharm. Bioallied Sci., *5,* pp.148-153. 2013.

218. Hamamoto H, *et al.* Effects of molecular mass and hydrophobicity on transport rates through nonspecific pathways of the silkworm larva midgut, Int. J. Antimicrob. Agents., *26,* pp.38-42. 2005.

219. John B, Joseph B, Michael BW. Physiology. Baltimore: Lippincott Williams & Wilkins. 2001.

220. Hacker M, Messer WS, Bachmann KA. Pharmacology: Principles and Practice. Burlington: Elsevier. 2009.

221. Scheibel T. Spider silks: recombinant synthesis, assembly, spinning, and engineering of synthetic proteins, Microb. Cell Fact., *3,* pp.14/1-10. 2004.

222. Kaplan DL, Adams WW, Farmer B, Viney C (eds). Silk polymers: materials science and biotechnology. pp. 2-16, Washington DC: American Chemical Society. 1994.

223. Craig CL. Evolution of arthropod silks, Annual Review of Entomology, *42,* pp.231-267. 1997.

224. Vollrath F, Knight DP, Hu XW. Silk production in a spider involves acid base treatment, Proc. R. Soc. London B-Bio. Sci., *265,* pp.817-820. 1998.

225. van Beek JD, Hess S, Vollrath F, Meier BH. The molecular structure of spider dragline silk: Folding and orientation of the protein backbone, Proc. Nat. Acad. Sci. USA, *99,* pp.10266-10271. 2002.

226. Perez-Rigueiro J, Viney C, Llorca J, Elices M. Mechanical properties of single-brin silkworm silk, J. Appl. Polym. Sci., *75,* pp.1270-1277. 2000.

227. Perez-Rigueiro J, Elices M, Llorca J, Viney C. Tensile properties of silkworm silk obtained by forced silking, J. Appl. Polym. Sci., *82,* pp.1928-1935. 2001.

228. Perez-Rigueiro J, Elices M, Llorca J, Viney C. Effect of degumming on the tensile properties of silkworm (*Bombyx mori*) silk fiber, J. Appl. Polym. Sci., *84,* pp.1431-1437. 2002.

229. Domachuk P, Tsioris K, Omenetto FG, Kaplan DL. Bio-microfluidics: Biomaterials and biomimetic designs, Adv.Mater., *22,* pp.249-260. 2010.

230. Kim DH, Kim YS, Amsden J, Panilaitis B, Kaplan DL, Omenetto FG, Zakin MR, Rogers JA. Silicon electronics on silk as a path to bioresorbable, implantable devices, Appl. Phys. Lett., *95,* pp.133701-133703. 2009.

231. Omenetto FG, Kaplan DL. A new route for silk, Nature Photon., *2,* pp.641-643. 2008.

232. Hino R, Tomita M, Yoshizato K. The generation of germline transgenic silkworms for the production of biologically active recombinant fusion proteins of fibroin and human basic fibroblast growth factor, Biomaterials, *27,* pp. 5715-5724. 2006.

233. Benfenati V, Toffanin S, Capelli R, Camassa LM, Ferroni S, Kaplan DL, Omenetto FG, Muccini M, Zamboni R. A silk platform that enables electrophysiology and targeted drug delivery in brain astroglial cells, Biomaterials, *31,* pp. 7883-7891. 2010.

234. Bray LJ, George KA, Ainscough SL, Hutmacher DW, Chirila TV, Harkin DG. Human corneal epithelial equivalents constructed on *Bombyx mori* silk fibroin membranes, Biomaterials, *32,* pp. 5086-5091. 2011.

235. Tan PH, Aung KZ, Toh SL, Goh JC, Nathan SS. Three-dimensional porous silk tumor constructs in the approximation of *in vivo* osteosarcoma physiology, Biomaterials, *32,* pp. 6131-6137. 2011.

236. Selwyn JE, Steinfeld JI. Aggregation equilibria of xanthenes dyes, J. Phys. Chem, *76,* pp. 762-774. 1972.

237. Antonov L, Gergov G, Petrov V, Kubista M, Nygren J. UV-Vis spectroscopic and chemometric study on the aggregation of ionic dyes in water, Talanta, *49,* pp. 99-106. 1999.

238. Kuriyama K, Eguchi M. Conversion of the molecular-form by alkaline treatment of gut protease from the silkworm, *Bombyx mori*, Comp. Biochem. Physiol. B, *82,* pp. 575-579.1985.

239. Edwards EW, Chanana M, Wang D, Möhwald H. Stimuli-responsive reversible transport of nanoparticles across water/oil interfaces, Angew. Chem. Int. Ed, *47,* pp. 320-323. 2008.

240. Shore PA, Brodie BB, Hogben CAM. The Gastric Secretion of Drugs: A pH Partition Hypothesis, J. Pharmacol. Exp. Ther., *119,* pp.361-9. 1957.

241. Mannhold R (ed). Molecular drug properties. Weinheim: Wiley-VCH. 2008.

242. Segalat L. Invertebrate animal models of diseases as screening tools in drug discovery, ACS Chem. Biol., *2,* pp.231-236. 2007.

243. Tampakakis E, Okoli I, Mylonakis E. A *C. elegans*-based, whole animal, in vivo screen for the identification of antifungal compounds, Nat. Protocol, *3,* pp.1925-1931. 2008.

244. Lieschke GJ, Currie PD. Animal models of human disease: zebrafish swim into view, Nat Rev Genet, *8,* pp.353-367. 2007.